Technische Universität München

Physik-Department

Lehrstuhl für Biophysik E22

SILICON-ON-INSULATOR BASED THIN-FILM-RESISTOR FOR THE DETECTION OF BIOMOLECULAR INTERACTIONS

Michael G. Nikolaides

Für Eva und Sophia

Table of Contents

Zusammenfassung

Das Verständnis molekularer Wechselwirkungen in komplexen Systemen, wie zum Beispiel lebenden Zellen, stellt eine der grossen Herausforderungen an zukünftige biophysikalische Forschungsarbeiten dar. In Anbetracht der riesigen Anzahl verschiedener Moleküle in lebenden Systemen benötigt man spezielle Detektionsmechanismen zur Analyse. In diesem Zusammenhang bleibt die Detektion an der flüssig/fest Grenzfläche einer der vielversprechendsten Ansätze. Die Detektion von Molekülen an der flüssig/fest Grenzfläche ist auch für viele Anwendungen wichtig, von der Analyse industrieller Abfälle bis hin zu medizinischen Fragestellungen. Die Hauptanforderung an ein neuartiges Sensorsystem ist die Fähigkeit, Moleküle spezifisch mit hoher Emfindlichkeit zu detektieren. Darüberhinaus ist es unerlässlich, dass viele Reaktionen parallel detektiert werden können, um die Vielzahl der Wechselwirkungen zu bewerkstelligen. Oberflächennahe, zweidimensionale Elektronensysteme in Halbleitern erfüllen beide dieser Anforderungen.

Die vorliegende Arbeit beschäftigt sich mit der Entwicklung eines Sensors basierend auf halbleitenden Silicon-On-Insulator (SOI) substraten zur Detektion von biologischen und chemischen Molekülen. Mit diesem Sensor wurde die spezifische Bindung eines Proteins an membranständige Rezeptoren mit hoher Empfindlichkeit gemessen.

Die SOI Substrate bestanden aus einer 30 nm dicken, leicht p-dotierten ($c_{Bor} = 10^{16} cm^{-3}$), einkristallinen Siliziumsensorschicht mit (100) Orientierung, welche auf einem vergrabenen Oxid mit einer Dicke von $100\,nm$ oder $200\,nm$ saß. Der Substratwafer bestand aus leicht p-dotiertem Silizium ($c_{Bor} = 10^{16} cm^{-3}$) mit einer Dicke von ca. $650\,\mu$m. Ein Kontakt auf der Rückseite des Wafers diente zum Anlegen einer Gate Spannung, um die Ladungsträgerkonzentration in dem dünnen Sensorfilm zu kontrollieren, sowie den Arbeitspunkt festzulegen. Eine in den Elektrolyten getauchte Ag/AgCl Elektrode diente zur Potentialkontrolle und zum Anlegen einer Front Gate Spannung an der vorderen Oberfläche des Sensors. Der Zusammenhang zwischen gemessenem Widerstand und Oberflächenpotential wurde in einer Kalibrationsmessung bestimmt.

Die Antwort des Sensors mit natürlicher Oxidoberfläche gegenüber Veränderungen des pH-Werts und der Salzkonzentration wurde gemessen und die Messungen stimmten mit der Site-binding Theorie und der Grahame Gleichung sehr gut überein. Die Sensitivität gegenüber Veränderungen des pH Werts betrug $-50 mV/pH$. Adsorptionsexperimente von Poly-L-Lysin auf der blanken Oxidoberfläche liessen eine Abschätzung der Sensitivität zu $1e^-/100nm^2$ zu.

Um die Stabilität der Sensoren über lange Zeiten zu verbessern wurde die Oberfläche mittels aufgeschleuderter Poly-Methyl-MethAcrylate (PMMA), sowie kovalent gebundener OctadecylTriMethoxySilane (ODTMS) Schichten hydrophobisiert. Beide Methoden resultierten in einer hydrophoben Oberfläche, was durch Kontaktwinkelmessungen bestätigt wurde. Auf den PMMA bedeckten Sensoren war die pH Antwort stark reduziert, jedoch waren die Schichten nicht stabil genug für eine weitere Verwendung als Passivierungsschicht. Dagegen war die pH Antwort auf den ODMTS passivierten Sensoren nahezu unverändert, da die ODTMS Schichten permeabel für H^+ Ionen waren. Die ellipsometrisch bestimmte Dicke der ODTMS Schichten betrug $\approx 1.5 - 2\,nm$, was auf eine Monolage hindeutet.

Auf die ODTMS hydrophobisierten Oberflächen wurde mittels der Solvent Exchange Technik eine Lipidschicht bestehend aus DMPC, Cholesterol und DOGS-NTA gebracht. Die Kopfgruppen der funktionellen DOGS-NTA Lipide wurden durch Zugabe von Nickel bzw. EDTA enthaltenden Puffern umgeladen und diese molekulare Umladung konnte mit dem Halbleitersensor gemessen werden. Die maximal erreichbare Sensitivität betrug $1e^-/650nm^2$. Das gemessene Signal für die Umladung hing linear mit der Konzentration an funktionellen Lipiden an der Oberfläche zusammen und konnte in einem theoretischen Modell innerhalb der linearisierten Poisson-Boltzman Theorie erklärt werden.

Das Potential der Sensoren, biomolekulare Vorgänge quantitativ zu messen, konnte durch die Detektion der spezifischen Bindung von synthetisch hergestellten Peptiden und natürlichen Proteinen mit Histidine-Linker an die komplexierten NTA Kopfgruppen der Lipide demonstriert werden. Die Ergebnisse für die puren Histidin linker, für 6 Asparaginsäuren mit Histidin linker, sowie für die natürlichen Proteine GFP und LuSy wurden gemessen und ließen sich innerhalb des entwickelten einfachen Modells erklären. Die Sensitivität gegenüber der Bindung von GFP betrug 1 Molekül / $65nm^2$.

Diese Messungen sind der bisher erste erfolgreiche Nachweis einer Proteinbindung an einen Rezeptor in einer biokompatiblen Membran mit Hilfe eines Halbleitersensors.

Summary

Understanding the interactions between molecules in complex systems, such as the cells of living organisms, remains one of the main challenges for future biophysical research. Facing the huge number of molecules in living systems, sophisticated detection techniques have to be applied. In this context, the specific and sensitive detection of molecular interactions at solid/liquid interfaces remains one of the most promising approaches. This detection is also becoming increasingly important for a wide variety of applications and technologies, ranging from the analysis of industrial waste to biomedical applications. The main requirement for new sensor technologies is the highly sensitive and specific detection of molecules. However, at the same time, for the applicability of the technique towards screening of biomolecular interactions, the potential of simultaneous parallel detection is mandatory. Surface near, two dimensional electron systems in semiconducting materials are thought to fulfill both of these requirements, a high sensitivity against surface events and the possibility for highly parallelized devices through standard semiconductor technology.

In this thesis, a sensor device based on semiconducting <u>S</u>ilicon-<u>O</u>n-<u>I</u>nsulator (SOI) for the detection of biological and chemical molecules has been developed and specific protein binding events to receptors incorporated into lipid membranes have been detected with high sensitivty by these sensors.

The SOI wafers used to produce the sensor devices consisted of a 30 nm thick, slightly boron-doped ($c = 10^{16} cm^{-3}$), single crystalline Si (100) sensor layer on top of a buried oxide layer of $100\,nm$ or $200\,nm$ thickness. The substrate wafer underneath the buried oxide was also slightly p-doped silicon and had a thickness of $650\,\mu m$. The whole structure was covered by a thin ($1 - 2\,nm$) layer of native oxide. A voltage applied at the back side of the wafer (U_{bg}) was used to control the charge carrier concentration in the conducting sensor layer and to set the working point for the sensor measurements. A Ag/AgCl reference electrode immersed into an electrolyte on top of the sensor surface was used to control the potential of the electrolyte and to apply front gate voltages. Calibration measurements were carried out to relate the measured changes in sheet resistance to changes in the surface potential.

To verify the sensor mechanism, the response of the sensors with native oxide surface against variations of the pH and the salt concentration of an electrolyte was measured and compared to the theoretical predictions of the site-binding theory and

the Grahame equation, yielding excellent agreement. The sensitivity of the pH measurement was $-50mV/pH$ and from the noise level, the sensitivity of the developed sensor device was extrapolated to be $0.02-0.04$ pH steps. By detecting the adsorption of charged poly-l-lysine, the sensitivity of the sensors towards changes of the surface charge density was estimated to be $1e^-/100\,nm^2$.

To reduce the drift of the signal over long times and to further functionalize the sensors, the surface was hydrophobized by the adsorption of Poly-Methyl-MethAcrylate (PMMA) or the covalent binding of OctadecylTriMethoxySilane (ODTMS). Both methods yielded a hydrophobic surface as indicated by an increase in the contact angle. For the PMMA covered devices, the pH response was drastically reduced, but the layer was not stable enough for the further use as passivation layer in the lipid membrane experiments. Contrary, the pH response of the ODTMS covered devices did not disappear due to the permeability of the layer for H^+ ions, but the layer was very stable due to the covalent bond to the surface. The thickness of the ODTMS layers was determined by ellipsometry to be approx. $1.5\,nm$, indicating a monolayer of silane on the surface.

As biomimetic test system, a functional lipid monolayer with incorporated DOGS-NTA lipids was deposited on the ODTMS covered sensors. The headgroups of the DOGS-NTA lipids were charged and decharged by nickel or EDTA containing buffer and this charging was detected by the sensor with a sensitivity of $1e^-/650nm^2$. A theoretical model within the standard linearized Poisson-Boltzman theory was developed to explain the measured linear increase of the signal with the concentration of incorporated functional lipids.

The potential of the sensor for the quantitative detection of biomolecular interactions was demonstrated by measuring the specific and reversible binding of histidine tagged artificial peptides and natural proteins to the functional lipid mono layer. As example petides, the binding of His6Asp6, Green Fluorescent Protein (GFP) and Histidine$_{360}$ LumazinSynthase (His$_{360}$LuSy) was detected and the obtained signals were quantitatively explained with the previously developed model. The binding of GFP was observed with a sensitivity of 1 molecule/$65nm^2$ and was shown to be reversible and specific.

So far, these binding measurements represent the first quantitative detection of specific protein binding events to a functional and biocompatible lipid layer with a semiconductor sensor device.

Introduction

The detection of molecular interactions at interfaces is of great interest for a wide variety of applications, ranging from basic biological research and the screening of new drugs to the analysis of industrial waste [Fodor, 1997]. One possible approach to detect molecules at interfaces is the use of modern semiconducting materials as substrate and sensor at the same time. The binding of a molecule at the interface or a change of the surface charge density influences the band structure of the underlying material and consequently the electrical properties of the semiconductor. When the semiconductor is designed in a smart way, these changes can be detected and directly read out by a computer device.

Apart from using smart semiconductor devices, other techniques have been developed for the detection of molecules at solid/liquid interfaces.

DNA chips are used to detect the hybridization of DNA and hence to read out the genetic information of a DNA probe [Fodor et al., 1991]. On these chips, a huge variety of different fragments of DNA is synthesized in a spot pattern on a glass slide and the DNA to be analyzed is amplified in a polymerase chain reaction and labelled with a fluorescent dye. The hybridization to the complementary strand on the glass surface can be observed in a fluorescent microscope [Fodor, 1997, Chee et al., 1996]. Hence, the resulting spot pattern contains information about the DNA content and by analyzing this pattern, the DNA sequence can be obtained.

To avoid the fluorescent label molecules, *Infineon* developed a fully electronic DNA Sensor, where the receptor DNA strands are immobilized on interdigitated gold electrodes. An inactive redox couple is attached to the DNA strand of interest. Upon hybridzation, the redox couple is activated and hence the conductivity between the interdigitated electrodes is changed significantly.

Even though these techniques work fine for the detection of DNA, for the analysis of the interaction between proteins, labelling approaches are much more difficult to apply. Attaching a label to a complex biomolecule, such as a protein, can result in a change of the three dimensional structure or even in a loss of its functionality. Therefore, for the detection of more complex interactions, label free detection schemes have to be used.

Among these, the most prominent example to detect protein interactions at surfaces is surface plasmon resonance (SPR). Surface plasmons are collective vibrations of electrons at the surface of a conductor. In order to excite a plasmon by light, energy and momentum of plasmon and photon must match. This is only possible, if the conductor is coupled to a medium with a refractive index $n > 1$. At a defined angle Θ_{min}, momentum and energy of the plasmon and the photon are equal and plasmons are excited. Changes in the refractive index at the surface of the conductor are directly reflected by a shift in the angle Θ_{min}. Therefore, changes at the surface, such as the adsorption of molecules or changes of the bulk buffer can be detected. SPR is very sensitive to mass changes at the interface and has been successfully used to detect proteins down to surface concentrations of $0.01 ng/mm^2$ [Dorn et al., 1998], but its applicability to screen many interactions in parallel is limited.

Apart from SPR, impedance spectroscopy can be used to analyze molecular interactions at interfaces. The complex impedance of an interface is measured during a reaction at the interface and is interpreted with the help of equivalent circuits. Changes in different frequency regimes can be attributed to different interfaces. For example, supported lipid membranes on functionalized Indium Tin Oxide (ITO) electrodes were used to detect the charging and decharging of NitriloTriaceticAcid (NTA) functionalized lipids with nickel ions and EthyleneDiamineTetraaceticAcid (EDTA) [Hillebrandt et al., 2002]. As these NTA-complexes can be used for the further binding of histidine tagged proteins [Schmitt et al., 1994], this system can serve as a model system for the detection of proteins in native environment [Dietrich et al., 1995]. However, the sensitivity of this technique is not high enough to detect the binding of proteins to the lipid layer [Hillebrandt et al., 2002].

In contrast to this, surface near quasi two dimensional electron systems in semiconductor materials are known to have a very high sensitivity towards changes at the surface and can be parallelized. Many different material systems are being used to study the effect of molecules on the conductivity of semiconductor systems.

An extensively studied system are Ion Selective Field Effect Transistors (*ISFETs*), where the surface of a field effect transistor structure is sensitive to changes in the electrolyte. *ISFETs* based on standard silicon technology have been shown to be a versatile tool to detect chemical and enzymatic reactions [Kharitonov et al., 2001, Cooper et al., 2001]. The direct electrical detection of cell signalling was realized with recently developed semiconductor chips [Zeck, G. and Fromherz, P., 2001]. The

capacitive detection of inversion layers in silicon structures was successfully used to monitor the hybridization of DNA molecules [Fritz et al., 2002]. Silicon nanowires have been demonstrated to detect the binding of streptavidin to immobilized biotin with very high sensitivity [Ciu et al., 2001].

GaN based $ISFETs$ have been shown to have a high response towards pH changes of - $56mV/pH$ and have the additional advantage of being transparent, so that a parallel optical detection is possible [Steinhoff et al., 2003]. Two dimensional electron systems in $GaAs/AlGaAs$ hetero structures have a very high mobility and are therefore a promising candidate for the detection of molecules [Wu et al., 2001, Gartsman et al., 1998]. However, the instability of $GaAs$ in aqueous solutions has vitiated every attempt to use this material as functional sensor in biological systems [Adlkofer et al., 2000] and the development of the respective surface chemistry for GaN devices has hindered the application of this system to real biological samples so far.

In this thesis, a sensor device for the detection of biological molecules, based on quasi $2d$ electron systems in Silicon-On-Insulator (SOI) substrates is developed. The sensor device is characterized in electrolyte solution and good agreement was obtained with the theoretical predictions for the pH-response and the response to the ion concentrations (Chapter 3.2). To obtain a stable signal and a hydrophobic surface, the silicon oxide was passivated with ODTMS and a lipid monolayer was deposited on top of this passivated surface (Chapter 4.2). The monolayer consisted of a DMPC/cholesterol matrix with functional DOGS-NTA chelator lipids incorporated into this lipid monolayer. The charging and decharging of the NTA headgroups by adding EDTA and nickel containing buffer was detected (Chapter 5). Additionally, the specific binding of histidine-tagged artificial peptides and natural proteins to this monolayer was detected with high sensitivity. These measurements present the first detection of a protein binding event to a receptor in native environment with a semiconductor device so far (Chapter 6).

1 Basic Principles

The sensors developed in this thesis detect biomolecules at the solid-liquid interface, where the solid is a semiconductor and the liquid is an electrolyte. To develop a functional sensor for the detection of biological molecules, not only the bulk properties of both materials have to be known and understood, but also the interactions at the interface are important. Moreover, biological considerations as well as the understanding of of the surface chemistry are crucial for the successful detection of biological molecules in their native state. In this chapter, the basic physical, chemical and biological facts necessary to understand the further discussions are provided.

1.1   The SiO_2/Electrolyte Interface

A silicon oxide surface in contact with an electrolyte solution builds up surface hydroxyl groups. These hydroxyl groups are charged depending on the electrolyte pH. At the point of zero charge [1] the surface is neutral, for lower pH the net surface charge is positive, for higher pH it is negative. Consequently, for physiological pH values ($pH \approx 7$), the net surface charge of silicon oxide is negative and controls the potential drop into the solution. In this chapter, the relation between the surface potential ψ_s, the pH of the solution, the surface charge density σ and the concentration of ions in the electrolyte $[n_0, d_0]$ will be presented with the help of the *Poisson-Boltzman* theory and the site-binding theory.

1.1.1.   Poisson-Boltzman Theory and Grahame Equation

The potential distribution in an electrolyte solution above a silicon oxide surface is described by the Poisson-Boltzman theory. Figure 1.1 shows a SiO_x surface in an electrolyte solution. The charge density on the surface is σ and the electrolyte contains different ions i with valency z_i. The first layer of ions at the surface will be oppositely charged to the surfaces, yielding a double layer (DL), over whom the

---

[1]for silicon oxide, the point of zero charge is $pH_{pzc} = 2.2$
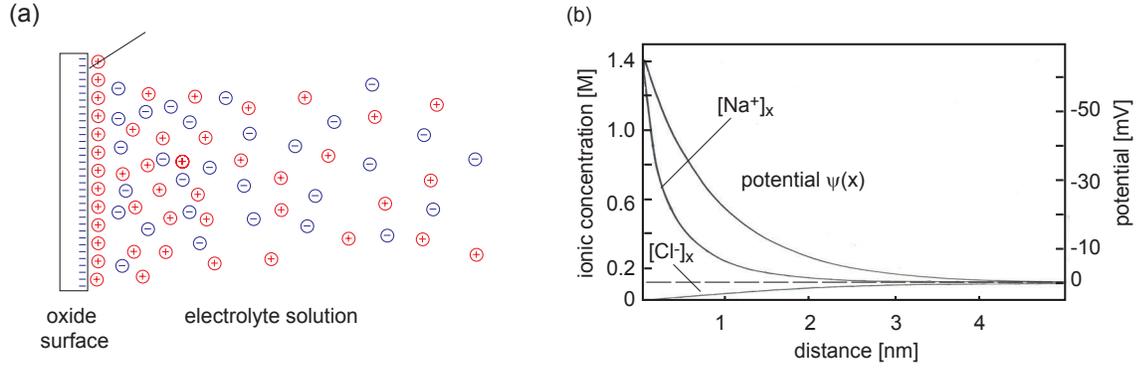
Figure 1.1: Sketch of a charged surface immersed in an electrolyte solution (a). The concentration of anions and cations reaches the bulk level of $0.1M$ after approx. $5\,nm$ (b). The potential drops according to the solution of equation 1.4.

potential drops linearly. Beyond this double layer, if the electrolyte solution is in thermal equilibrium, the concentration n_i of the ion species i at a distance x from the surface is given by

$$n_i(x) = n_{i,\infty} \cdot exp\left(\frac{z_i e\psi(x)}{k_B T}\right) \qquad . \tag{1.1}$$

where e is the elementary charge, k_B is the *Boltzman* constant, T is the temperature and $n_{i,\infty}$ is the concentration far away from the surface. The total charge density at a distance x is given by the sum of the different ion species:

$$\rho(x) = \sum_i \rho_i(x) = \sum_i n_i z_i e = \sum_i z_i\, e\, n_{i,\infty} \cdot exp\left(\frac{z_i e\psi(x)}{k_B T}\right) \tag{1.2}$$

In addition, the *Poisson equation*

$$\frac{\partial^2 \psi}{\partial x^2} = -\frac{\rho}{\epsilon} \tag{1.3}$$

has to be fulfilled. By inserting equation 1.2 into equation 1.3, the *Poisson-Boltzman* equation

$$\frac{\partial^2 \psi}{\partial x^2} = -\frac{1}{\epsilon} \sum_i z_i e n_{i,\infty} \cdot exp\left(\frac{z_i e\psi(x)}{k_B T}\right) \tag{1.4}$$

is obtained.

With the boundary conditions $\psi|_\infty = 0$ and $\frac{\partial \psi}{\partial x}|_\infty = 0$, for only mono- and divalent ions in the solution, the relation between the surface charge density σ, the surface potential ψ_s and the concentration of monovalent $[n_o]$ and divalent $[d_o]$ ions in the electrolyte can be obtained to

$$\sigma = \sqrt{8\epsilon\epsilon_0 kT} \sinh\left(\frac{e\psi_s}{2kT}\right) \sqrt{[n_0] + [d_0]\left(2 + e^{-\frac{e\psi_s}{kT}}\right)} \quad . \tag{1.5}$$

Equation 1.5 is known as *Grahame* equation [Israelachvili, J.N., 1985] and will be used to discuss the measurements for varying electrolyte concentrations (Chapter 3.2).

1.1.2. Relation between Surface Charge and *pH* (Site-Binding Theory)

To calculate the relation between the *pH* of the solution, the surface charge density and the surface potential, two possible surface reactions occurring at the SiO_2 / electrolyte interface have to be considered. Figure 1.2 shows a schematic representation of a silicon oxide surface in contact with an electrolyte. The chemical reactions between
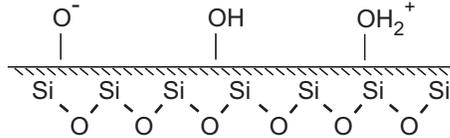
Figure 1.2: Schematic representation of the three different possible surface states of a silicon oxide surface in contact with aqueous solutions. Depending on the solutions *pH*, the neutral *OH* groups either lose an H^+ or bind an additional H^+ yielding positive and negative surface charge densities.

the different species follow the equations

$$SiOH \xleftrightarrow{K_a} SiO^- + H_s^+ \tag{1.6}$$

$$SiOH + H_s^+ \xleftrightarrow{K_b} SiOH_2^+ \quad , \tag{1.7}$$
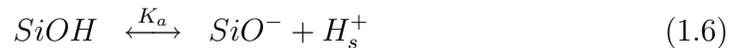
where K_a and K_b are the two chemical equilibrium constants and H_s^+ is the surface concentration of H^+ ions. These can be obtained from the concentration of surface

groups per unit area of the involved reactants as:

$$K_a = \frac{[SiO^-][H^+]_s}{[SiOH]} \tag{1.8}$$

$$K_b = \frac{[SiOH_2^+]}{[SiOH][H^+]_s} \qquad . \tag{1.9}$$

The net surface charge density σ is given by

$$\sigma = e([SiOH_2^+] - [SiO^-]) \tag{1.10}$$

and the total number of sites per unit area is

$$N_s = [Si - OH] + [SiOH_2^+] + [SiO^-] \tag{1.11}$$

The concentration of hydrogen ions at the surface ($[H^+]_s$) is related to the concentration of hydrogen ions in solution ($[H^+]_b$) over a Boltzman-factor

$$[H^+]_s = [H^+]_b \exp(-e\psi_0/k_B T) \tag{1.12}$$

The relationship between $[H^+]_b$, ψ_0 and σ can be derived from equations (1.8 - 1.12) in terms of K_a, K_b and N_s, which are the characterizing parameters of a specific oxide.

$$ln\,[H^+]_b - ln\left(\frac{K_a}{K_b}\right)^{1/2} = \frac{e\psi_s}{kT} + sinh^{-1}\frac{\sigma}{eN_s}\left(\frac{1}{4K_a K_b}\right)^{1/2} \tag{1.13}$$

For this calculation, it is assumed that $2(K_a K_b)^{1/2} \ll 1$ and $\sigma \ll eN_s$, both of which are valid for SiO_2.

In order to derive the relation between $pH = -log_{10}[H^+]_b$ and ψ_s, σ should be expressed in terms of ψ_s. It can be shown [Bergveld and Sibbald, 1988] that in practical cases the double layer capacitance can be approximated by a simple constant capacitance C_{DL}, which gives the relation between σ and ψ_s:

$$\sigma = \psi_s C_{DL} \tag{1.14}$$

Therefore, equation 1.13 directly describes the relation between pH and ψ_s, but needs further expansion for practical application. If we introduce the pH of the point of zero charge (pH_{pzc}) as a reference point on the pH-scale for which $\psi_s = 0$, it follows from equation 1.13 that

$$pH_{pzc} = -log_{10} \left(\frac{K_a}{K_b} \right)^{1/2} \qquad . \tag{1.15}$$

This value is called the point of zero charge, because $\psi_s = 0$ implies $\sigma = 0$. In other words, pH_{pzc} gives the hydrogen bulk concentration which results in an electrically neutral surface. Combining equations 1.13, 1.14 and 1.15 finally yields

$$\log{(pH_{pzc} - pH)} = \frac{q\psi_s}{k_B T} + \sinh^{-1} \left(\frac{q\psi_s}{k_B T} \frac{1}{\beta} \right) \qquad . \tag{1.16}$$

Here, for silicon oxide, $pH_{pzc} = 2.2$ and $\beta = \frac{2q^2 N_s \sqrt{K_a K_b}}{k_B T C_{DL}}$. The deduction presented here mainly follows [Bergveld and Sibbald, 1988], which also contains a further discussion of the topic.
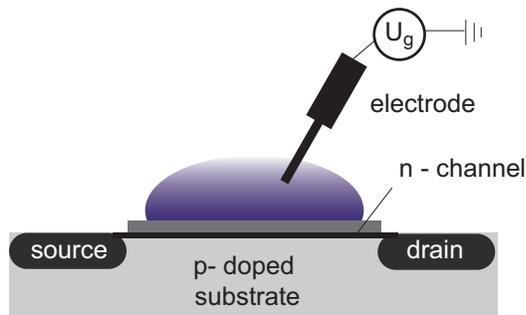
Figure 1.3: Sketch of a typical 'normally off' *ISFET*. Source and drain region are n-doped, the substrate is p-doped. With no gate voltage applied, no current is flowing through the channel.

1.2 *ISFET* Based Sensor Devices

The sensor system developed in this thesis has many similarities with a conventional I̲on S̲elective F̲ield E̲ffect T̲ransistors (*ISFETs*), which has been first introduced by Bergveld [Bergveld, 1970]. A lot of work has been dedicated to the properties of these devices, but until now, no real working protein sensor has been demonstrated. In this chapter, the basic properties of these devices will be presented qualitatively, as their understanding contributes to the understanding of the sensors used in this work.

ISFET devices are very similar to conventional M̲etal O̲xide F̲ield E̲ffect T̲ransistors (*MOSFET*) as used in modern semiconductor devices [Sze, S.M., 1981]. In contrast to *MOSFETs*, *ISFETs* have no metal gate and also react to the adsorption of charged molecules in addition to an applied gate voltage. Figure 1.3 shows a sketch of a typical *ISFET* based sensor based on a p-type silicon. The source and the drain regions are n-doped, separated by a short channel which is typically several nm in length. A thin layer of silicon dioxide is thermally grown over the substrate material in the channel, isolating it electrically from the electrolyte on top of it. Immersed in an electrolyte, an electrode is used to apply a gate voltage (V_{GS}) and hence to control the electrical conductivity in the channel.

Figure 1.4 shows the band structure of an *MOS* device in the three regimes that can be distinguished depending on the applied gate voltage. For negative gate voltages, holes are accumulated in the channel and no current can flow from source to

(a)   (b)   (c)
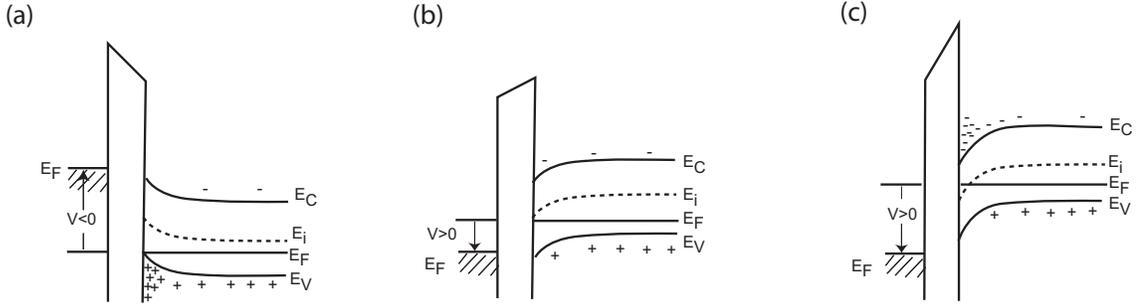
Figure 1.4: Band diagram of a p-type *MOS* structure in the three different possible regimes. (a) shows the accumulation case for negative gate voltages, whereas (b) shows the depletion for small positive gate voltages and (c) the inversion for higher positive gate voltages.

drain, because one of the pn-junctions between source and drain is blocking and the channel is cut-off (Figure 1.4 (a)).

For positive gate voltages, holes are depleted and the channel is not conducting (Figure 1.4 (b)). By further increasing the gate voltage, the channel will be inverted, i.e., electrons are accumulated and a thin conducting channel is built up between source and drain, yielding a significant current from source to drain (Figure 1.4 (c)). In this regime, the current from source to drain (I_D) increases for increasing source-drain voltage (V_{DS}) until the so-called 'pinch-off' is reached, where the source drain voltage drop is extending over only part of the channel and the current is not increased by a further increase of the source-drain voltage. The current voltage characteristics consequently exhibit a saturation plateau. The most widely used characteristics of such *ISFETs* are the $I_D - V_{GS}$ and the $I_D - V_{DS}$ relationships, which directly reflect the different types of operation. Figure 1.5 (a) shows the typical dependence of the channel conductivity from the gate voltage for an n-channel *ISFET* for a constant source-drain voltage. As mentioned earlier, for negative gate voltages, the *ISFET* is cut-off and no current can flow. For positive voltages, the channel is first depleted, but for gate voltages above the so called threshold voltage V_{th}, a significant current begins to flow.

Figure 1.5 (b) shows typical $I_D - V_{DS}$ relationships for an *ISFET* for different gate voltages. The dotted line separates the saturated region from the unsaturated region.

(a)   (b)
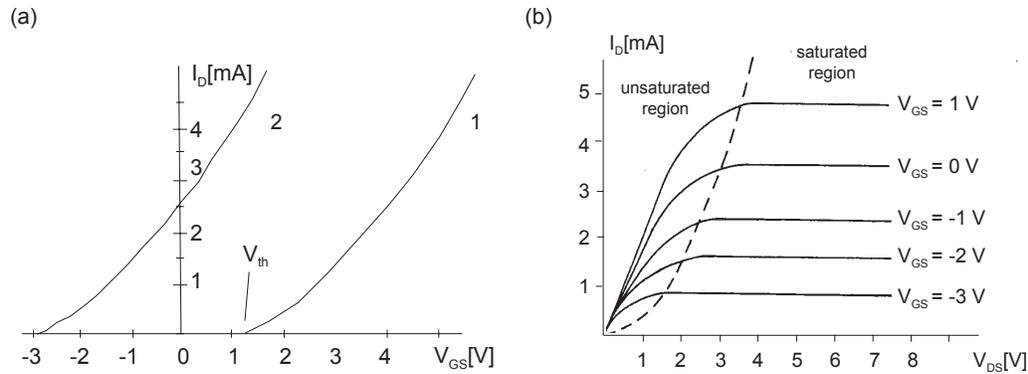
Figure 1.5: Typical $I_d - V_{gs}$ characteristics for an n-channel *FET* device (a)(1 = normally on; 2 = normally off type). In (b), typical $I_d - V_{ds}$ characteristics with various applied bias voltages are shown. One can clearly distinguish between the saturated region and the unsaturated region, separated by the dotted parabola.

The saturation of the current with the source-drain voltage can be clearly seen by the plateau region. The higher the applied gate voltage, the higher the saturation current.

The sensor devices developed in this thesis are similar to normally on, n-channel thin film *ISFET* devices. In order to be able to interpret the measurements in terms of a constant surface potential, the voltage drop between source and drain was kept as small as possible, and hence all measurements were performed in the linear regime of the unsaturated region.

native SiO$_2$	(1-2 nm)
silicon	(30 nm)
SiO$_2$	(100 nm / 200 nm)
silicon	(675 μm)
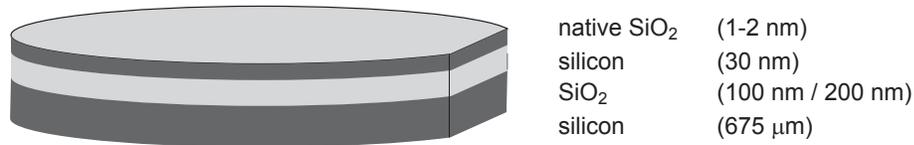
Figure 1.6: Silicon-on-Insulator substrate. The layer structure of the wafers used throughout this work was from bottom to top: Silicon wafer - buried SiO_2 - silicon sensor layer - native SiO_2

1.3 Properties of Silicon-On-Insulator (SOI)

SOI Layer Structure

In recent years, new material systems have been tested to be used as basis for modern semiconductor devices. As the devices get smaller and smaller, the interference between the devices gets more and important due to increased weight of leakage currents in the substrate wafer. In order to avoid these, the isolation of the conducting channel through an additional buried oxide was tested, leading to the development of Silicon-On-Insulator (SOI) material.

The typical layer structure of a SOI substrate is shown in figure 1.6. The conducting silicon layer is sandwiched between two oxide layers, the top oxide serving as gate oxide in the later devices and the buried oxide, insulating the channel from the substrate wafer.

The wafers used for this thesis were produced with the *ELTRAN* technique [Yonehara et al., 1994] as shown schematically in figure 1.7. The SOI and the insulating layers are originally formed on top of a seed wafer. To do that, double layered silicon having different porosities is formed on the seed wafer and a single-crystal silicon layer is epitaxially grown on top of this layer. After that, a thermal oxide is formed and the handle wafer is glued upside down to the layer structure on the seed wafer. A water-jet technique is used to split off the seed wafer within the porous silicon layer. Finally, a highly selective etching method is used to remove the remaining porous silicon and by H_2 annealing, the surface is planed on an atomic level. The resulting layer structure with the thicknesses used in this thesis is shown in figure 1.6.

seed wafer   handle wafer

anodizing, epitaxy
& oxidation

bonding

splitting

etching &
H$_2$ anneling
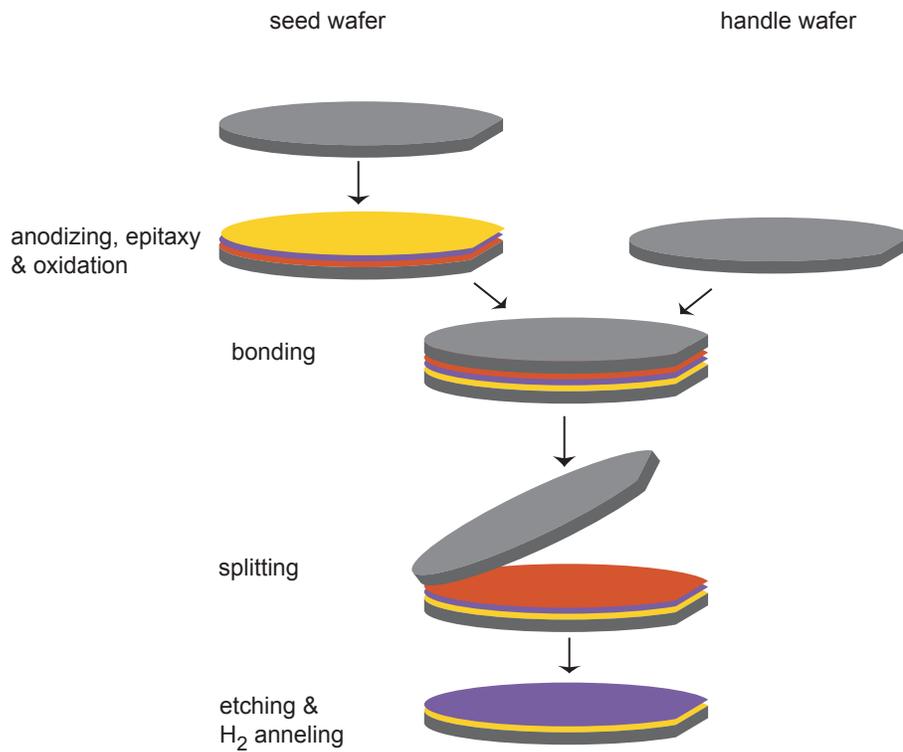
Figure 1.7: Process flow of the ELTRAN process to obtain high quality Silicon-on-Insulator sub-
strates.

Other methods used for the production of SOI are the implantation of a ox-
ide layer through the implantation with oxide ions (Separation by Implanted Oxy-
gen, SIMOX), which is described in detail in the literature. [Dong et al., 2004,
Tong and Gosele, 1993]

Band Diagram of SOI Layer Structures

In this thesis, a SOI layer structure with a top silicon thickness of 30 nm was used without further doping of the channel or the contact regions. Therefore, to understand the device characteristics of the sensors used in this work, a basic knowledge of the energetic band diagram of the pure layer structure is necessary.
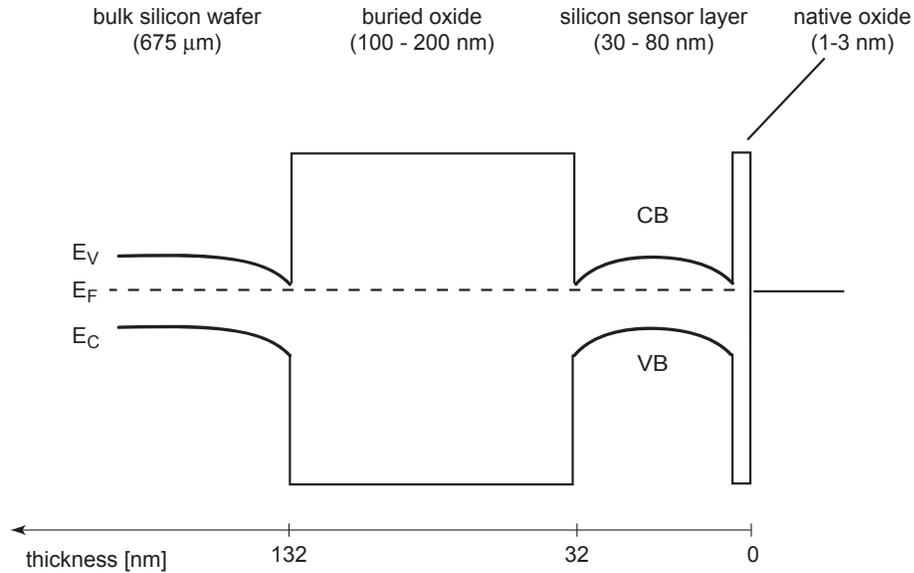
Figure 1.8: Schematic picture of the energetic band structure of the SOI substrates. The silicon sensor layer is sandwiched between two oxide layers, limiting the current to the surface near channel region. Changing the gate voltages influences the band structure and hence results in a change of the conductivity of the thin layer.

In Figure 1.8, a schematic picture of the band diagram as obtained from the simulation of the device with the software *nextnano*[3] [Vogl et al., 2004] is shown. The conducting channel is sandwiched between the barriers from the two oxide layers. The silicon layer presents a quasi two dimensional electron system, which is strongly influenced by the respective gate voltages applied to the gate electrodes on top of the oxide layers. For the sensor case, a gate voltage is applied at the back interface to drive the channel in a condition where surface events, occurring in the electrolyte are detected most sensitively. If a high enough positive back gate voltage is applied, the whole layer is inverted. This regime turned out to be best working for the detection of protein binding events at the surface (Chapter 3.1.3.). In chapter 3.1.1., the device characteristics resulting from this band diagram will be discussed in detail and in

chapter 3.1.4. and 3.1.3. the experimental results will be presented.

Electrical Transport in Silicon

The current in a semiconductor is carried by electrons and holes at the same time and the specific resistance ρ of a semiconductor can be described by

$$\rho = \frac{1}{\sigma} = \frac{1}{e(\mu_e n + \mu_h p)} \qquad , \qquad (1.17)$$

where n and p are the concentrations of electrons and holes in cm^{-3}, respectively. As good approximation, for non compensated semiconductors,

$$\sigma = e\mu_e n \quad \text{for n-type semiconductors, i.e.} \quad p \ll n \qquad (1.18)$$

$$\sigma = e\mu_h p \quad \text{for p-type semiconductors, i.e.} \quad n \ll p \qquad (1.19)$$

is fulfilled, where $\mu_{e/h}$ represents the mobility $[cm^2 V^{-1} s^{-1}]$.

For a quasi two dimensional system, the resistance is given in terms of a sheet resistance, being independent on the size of a squared area. Consequently, resistance values of such systems are given in a square resistance. For real cases, where the thickness of a conducting channel is very low but not zero as in the SOI sensors in this work, the specific resistance and the theoretical square resistance are related to each other by

$$R_{sheet} = \frac{\rho}{d} \qquad , \qquad (1.20)$$

where d is the thickness of the thin layer.

1.4 Solid Supported Lipid Membranes

One of the most important structural elements of living cells is their outer boundary, the plasma membrane. This membrane separates the cell inside from the outer environment. Already in 1972, a generally accepted model of the plasma membrane, the fluid-mosaic model was introduced [Singer and Nicolson, 1972]. In this model, the membrane consists from a fluid bilayer of amphiphilic phospholipids and cholesterol. This bilayer serves as a two-dimensional solvent for integral proteins and also contains anchoring sites for peripheral proteins (Figure 1.9(a)).

In an aqueous environment, the formation of the lipid bilayer structure and the incorporation of the proteins is driven by self-organization. This self assembly is driven by the hydrophobic effect, the gain of free energy through the exclusion of water during the aggregation of the alkyl chain parts of the lipid molecules and proteins [Hoppe et al., 1982].

The lipid-protein membrane composite provides a manifold of the functions of an individual cell. Together with the cytoskeleton bound to its inner side, it is responsible for the mechanical stability and the viscoelastic properties of the cell [Bausch et al., 1999]. Moreover, the plasma membrane regulates the transport of water and other molecules from the inside of the cell to the environment and vice versa. Hence it is also influencing the metabolism of the cell. The regulation of the ion transport via switchable ion channels enables the cell to build up chemical or electrical potential gradients across the membrane, which are the driving forces for many cellular processes and also regulate the communication of cells [B. Alberts, A. Johnson, J. Lewis, M. Raff, K. Roberts, P. Walter, 2002].

In order to study the properties of the plasma membrane, model membranes, so called supported membranes are deposited directly onto a solid support. The advantages of supported membranes, regarding the practical and scientific application are generally accepted in literature [Sackmann, 1996, Steinem et al., 1996]. As these membranes can be prepared from self assembly processes (see section 2.2.3.), the preparative effort is reduced drastically.

By depositing only the upper leaflet of the bilayer on a previously hydrophobized substrate, unwanted screening effects are omitted and charge effects are detected with a higher sensitivity. Hence, this system combines two main requirements for a working protein sensor. On the one hand, a specific receptor can be incorporated into a native environment (i.e. the lipid monolayer). On the other hand, the signal
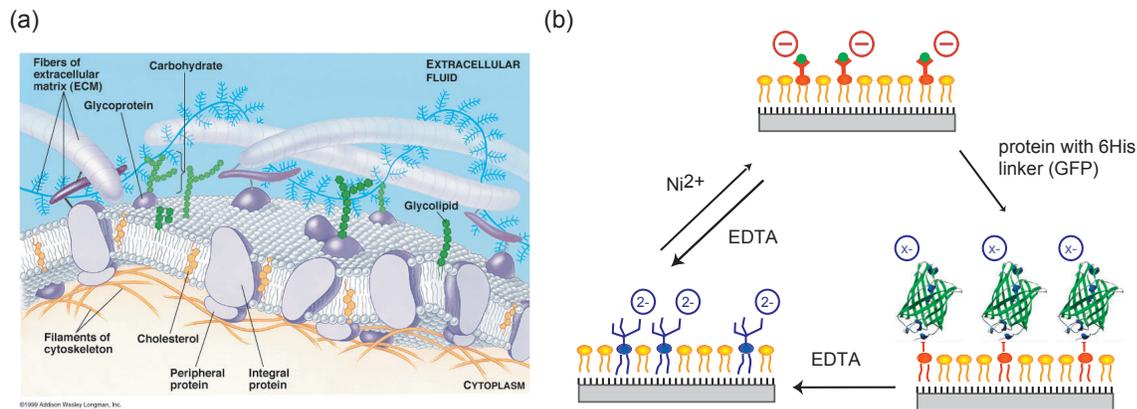
Figure 1.9: Sketch of a lipid cell membrane with the lipid molecules, peripheral proteins and the extracellular matrix (a). Model chelator lipid system as used in this thesis. The functional headgroups can be charged and decharged on a molecular level and can also serve a specific binding site for Histidine-tagged proteins (b) [Schmitt et al., 1994].

produced by the charge of any binding molecule is not reduced due to screening effects of a water layer between the substrate and the biological system. Both, lipid mono- and bilayers are well suited for coating applications of solid surfaces. Besides their intrinsic biocompatibility they can be functionlized easily and transferred to many different surfaces.

A common lipid system for the functionalization of surfaces is the chelator lipid system, which is based on the reversible binding of a protein via histidine-tag onto hydrophilic metal-chelator headgroups of lipids [Schmitt et al., 1994, Dietrich et al., 1995, Rädler et al., 2000]. One important feature of this immobilization technique is the oriented immobilization of the protein due to the engineered histidine-tag in the protein site. To preserve this orientation, unspecific interactions of the protein like penetration into the lipid layer or adsorption at interfaces have to be suppressed. Additionally, proteins may unfold upon contact with hydrophobic surfaces and therefore loose their functionality. A histidine-tagged Green Fluorescent Protein (GFP) was chosen as model protein to test the semiconductor sensor performance. Due to its intrinsic fluorescence, emitting light only if the protein is correctly folded and therefore functional [Ormo et al., 1996], the binding of functional GFP to lipid layers on glass susbtrates can easily be observed by fluorescence microscopy. Figure 1.9(b) shows a sketch of the lipid monolayer deposited on

a hydrophobic solid surface as used in this work and also illustrates the reversible charging and decharging of the NTA haedgroups with nickel and EDTA containing buffer. Moreover, it also shows that histidine tagged proteins can be specifically and reversibly bound to the complexed chelator lipids. The monolayer was composed of a DMPC/cholesterol matrix with different concentrations of functional DOGS-NTA (see section 2.2.3.) lipids incorporated in it. This lipid system has been shown to specifically bind functional GFP by fluorescence spectroscopy and SPR before [Dietrich et al., 1995, Schmitt et al., 1996].

2 Materials and Methods

In order to have a working semiconductor sensor, which is able to detect biologically relevant molecules in their native state, three major tasks had to be solved during this thesis. The first part was the development and optimization of the semiconductor technology to produce the bare surface devices. The second part was the design and optimization of the measurement setup and to programm a measurement software. Finally, the most challenging part was the development of the biofunctionalization of the surface in such a way that on the one hand the semiconductor devices were not destroyed and on the other hand, good enough surface properties were obtained for the specific binding of biological molecules. In section 2.1, the semiconductor technology is described, whereas section 2.2 describes the surface modifications. Finally, section 2.3 contains details about the measurement setup.

2.1 Sensor Production

In this section, the starting material - commercially available SOI wafers - as well as the technology used to process the devices will be described. The details of the process flow are described in the appendix.

Silicon-on-Insulator Substrate

SOI wafer consist of a thick silicon wafer, followed by a layer of silicon oxide (buried oxide, BOX) and a thin layer of crystalline silicon on top of it. The structure is covered by a thin layer of native oxide. The wafers used throughout this work were purchased from *Canon Inc., Japan* and were produced after the *ELTRAN* (Epitaxial Layer Transfer) process. Two different wafer types were used, differing only in the thickness of the buried oxide. The wafers had a diameter of *6"* and a total thickness of $650\,\mu m$. The substrate wafer was (100) silicon, slightly doped ($10^{16}cm^{-3}$) with boron and had a resistance of *8* Ωcm^{-3}. The buried oxide (BOX) has a thickness of either *100 nm* or *200 nm*. The single crystalline silicon layer has (*100*) orientation, is also boron doped ($10^{16}cm^{-3}$) and has a thickness of *30 nm*. Like any silicon surface
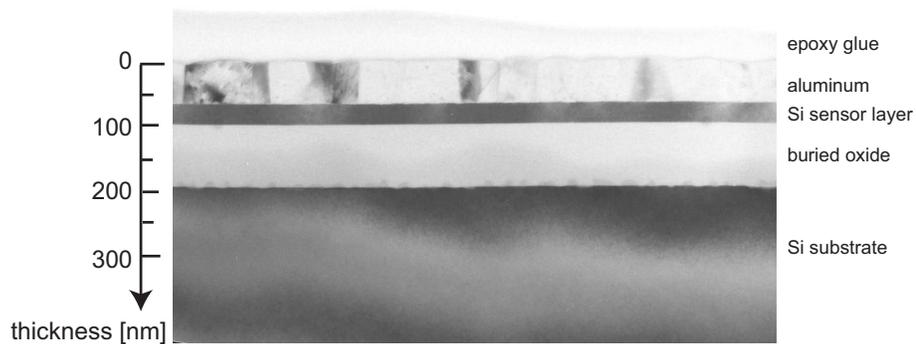
Figure 2.1: TEM image of the SOI layer structure after the metallization with aluminum [Lindner, 2003]. The layer structure reads (from top to bottom): Epoxy glue from the preparation, app. 70 nm Al, 30 nm Si sensor layer, 100 nm buried SiO_2, bulk silicon wafer.

under ambient conditions, the structure is covered with a native silicon oxide of *1-2 nm* thickness.

Figure 2.1 shows a TEM image of one of the SOI wafers with *100 nm* BOX [Lindner, 2003]. One can clearly distinguish the different layers. The native oxide is too thin to be resolved in this image.

Wafer Cutting and Cleaning

The sensor production is a single die process and consequently the wafers were cut into single dice of 9.3 mm x 9.3 mm on a Suess Microtec Ritztisch before the further processing. After the cutting, the wafers were blown with a stream of dry nitrogen. To remove the remaining silicon dust and to start with reproducible surface conditions, the wafers were sonicated and rinsed consecutively in acetone and isopropanol and dried again under nitrogen. The single wafer pieces were stored in clean sample boxes until the further processing.

MBE Overgrowth

To vary the doping concentration, some of the devices were overgrown with an additional layer of doped silicon with a Molecular Beam Epitaxy (*MBE*) process
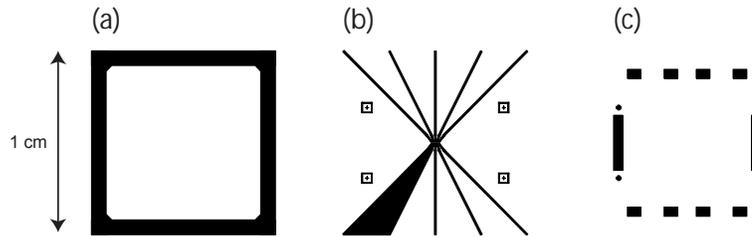
Figure 2.2: Photo mask used for the sensor processing. (a) shows the outer edge definition, (b) shows the hallbar structure with the positioning markers for the metallization (c) [Luber, 2002].

[Brunner, 2002]. In a MBE process, the wafers are exposed to silicon evaporated with an electron beam and boron from a *Knudsen*-effusion cell at the same time. The wafer is heated to $600^\circ C$ to enable the diffusion of the atoms at the surface resulting in high crystalline quality. The process takes places in ultra high vacuum (UHV). The thickness of the resulting single crystalline layer was chosen to be $50\,nm$ and the doping concentration was $10^{18}cm^{-3}$. Only boron was used as dopant [Riedl and Brunner, 2002]. Except for the measurement of the dependance of the sheet resistance from the electrolyte salt concentration in section 3.2.1. and the adsorption experiments with polyelectrolyte multi layers in section 3.2.2., all measurements in this thesis were done on wafers with original, i.e. $30\,nm$ thick slightly p-doped ($10^{16}cm^{-3}$) silicon sensor layer. Throughout this work, these sensors will be called *undoped* or slightly doped sensors to distinguish them from the additionally MBE overgrown sensors.

Photolithography

The standard technology to define structures on a semiconductor wafer is photolithography. A master structure is defined on the photo mask, which consists from a structured chromium layer deposited on a quartz glass. To define the master structure on the wafer, a thin film of photosensitive polymer is spin coated onto the wafer and hardened in an additional heating step. The photoresist is illuminated with UV-light over the mask, developed and hardened again. After that, either the metallization or the wet chemical etching takes place. The used photoresist was positive, meaning that the illuminated regions were removed by the developer. The structures on the mask to define the active regions of the sensor and to define the metal contacts are
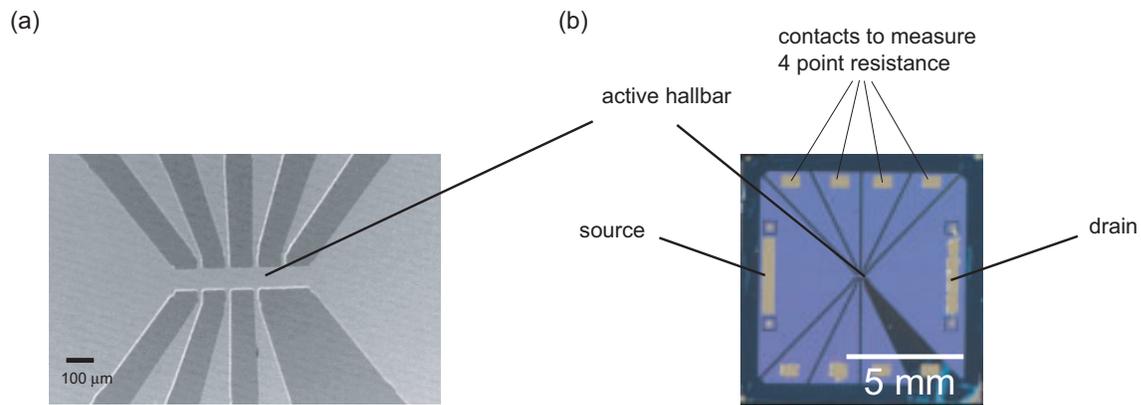
Figure 2.3: (a) Optical micrograph of the sensing device. Bright regions indicate conducting silicon, insulating silicon dioxide appears dark. The dimensions of the active hallbar in the middle are $240\,\mu m$ x $80\,\mu m$. Seven contacts along the hall bar can measure the voltage drop and are designed to yield the area normalized square resistance. The effective region measured is $80\,\mu m$ x $80\,\mu m$. The contact in the bottom right was left free to enable the additional metallization with a metal front gate. (b) Image of the sensor device after the lift-off process. The source and drain contact are on the left and right, the seven contacts to the hallbar are the small contacts on the top and on the bottom.

shown in figure 2.2.

The silicon layer is structured into an active hallbar in the middle, the metal contacts are sitting on the outside of the chip. The hallbar dimensions are $80\,\mu m$ x $240\,\mu m$, the overall size of the chip is 9.3 mm x 9.3 mm. The outer edge of the chip was also removed to avoid unwanted electrical contacting to the substrate.

Figure 2.3 (a) shows a microscopic image of the inner part of the sensor with the active hallbar after the etching step.

Etching

To define the active region, part of the silicon layer has to be removed. This was done by exposing the photo resist covered and developed wafer to a mixture of HF, HNO$_3$ and water. The chemical reaction for the etching of the Si layer is a two step process. In the first step, the silicon on the surface is oxidized to SiO_2, in a second step, this oxide is dissolved by HF. The chemical reaction equation is given by:

$$
\begin{array}{rcl}
3\,Si + 4\,HNO_3 & \longrightarrow & 3\,SiO_2 + 4\,NO \uparrow + 2\,H_2O \\
3\,SiO_2 + 18\,HF & \longrightarrow & 3\,H_2SiF_6 + 6\,H_2O \\
\hline
3\,Si + 4\,HNO_3 + 18\,HF & \longrightarrow & 3\,H_2SiF_6 + 4\,NO \uparrow + 8\,H_2O
\end{array}
\tag{2.1}
$$
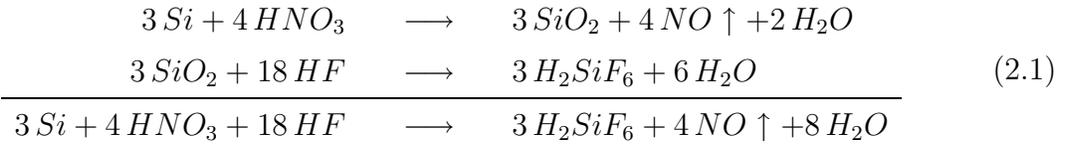
As this etching process is not strongly selective between Si and SiO_2 and the etching rate is dependant on the doping concentration, special attention has to be paid in order not to completely remove the buried oxide. However, when the silicon sensor layer is removed completely, the color of the substrate changes. This color change can hence be used as indicator for the etching time.

Metallization

The area of the ohmic contacts is defined in an additional photolithography step after the etching of the silicon layer. Before the metallization, the native oxide layer is removed with a HF dip. The metal is deposited in an evaporation chamber by e-beam. The thickness of the deposited layer is measured with a quartz crystal micro balance during the deposition. After the metal deposition, the photoresist and the metal on top of it is removed in a lift-off process in acetone.

The sensor with metal contacts after the lift-off process can be seen in figure 2.3 (b). The source and drain contacts are 3 mm x 0.5 mm, the contacts to the hallbar are 0.5 mm x 0.75 mm.
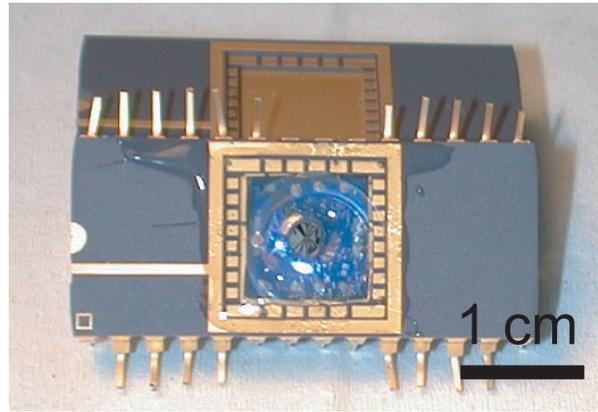
Figure 2.4: Image of an encapsulated sensor. In the middle of the chip carrier, the epoxy protects the metallization from the electrolytes. Only the inner part of the chip is exposed to the electrolytes. The metal contacts are bonded to the metal pads of the chip carrier which are connected to the leads of the carrier. In this case, the empty leads are bend up. The remaining leads can be plugged into a commercially available IC-socket.

Bonding and Encapsulation

After the metallization, the sensors were either functionalized in additional steps (see section 2.2.2.) or used directly with only the native oxide covering the sensor layer. In both cases, the active area of the sensor has to be exposed to electrolyte solutions, but the metal contacts must not get in touch with the solution. This was achieved by bonding the sensor into a chip carrier with an ultrasound bonder and encapsulating the bond wires, metallization and contact pads with silicon rubber.

The bond wires were bonded to the carrier, but had to be glued with a two component conducting glue to the chip. All attempts to bond the wire to the chip resulted in the destruction of the buried oxide and hence in a breakthrough to the substrate. Figure 2.4 shows a completely processed and encapsulated sensor with the open active region in the middle. The details of the bonding and encapsulation process are given in the appendix.

2.2   (Bio-)chemical Preparation Methods

Only if the right surface chemistry is used for the passivation and the functionalization of the sensor devices, a functional sensor with high enough sensitivity can be obtained. In this section, all chemicals and buffer solutions used throughout this work are described. If not stated otherwise, all chemicals were used without further purification as obtained from the manufacturer. Moreover, the preparation techniques used for the functionalization and passivation as well as for the deposition of lipid mono- and bilayers are described.

2.2.1.   Electrolyte Buffers

For the measurements of pH variations and changes in the salt concentration, buffer solutions prepared with deionized water[1] are used. *10 mM* phosphate buffer, composed from the two potassium salts K_2HPO_4 and KH_2PO_4 in the relation 4 : 1 was used as buffer system. Throughout this work, this mixture will be called standard *PBS* buffer. For the pH measurements, additional *90 mM* KCl was added and the pH was adjusted with KOH or HCl, respectively. For the measurements of the salt concentration, the pH was adjusted at 6.4 and the concentration of additional KCl was varied. Before the measurements, all buffers were degassed at room temperature.

For the adsorption of poly-l-lysine on the bare SiO_2 surface (section 3.2.2.), different concentrations dissolved in standard *PBS* buffer were used. In addition, *490 mM KCl* was added to the buffer and the pH was adjusted at $pH = 6.4$. Poly-l-lysine with a molecular mass of *80.000 g/mol*, corresponding to approx. *600* lysine monomers per molecule was purchased from Sigma-Aldrich (Sigma-Aldrich, Germany).

For the adsorption of polyelectrolyte multi layers, buffer solutions with a concentration of *5 mg/ml* of poly(allalamine hydrochloride) (*PAH*) or poly(sodium 4-styrenesulfonate) (*PSS*) were prepared. The buffer system in these experiments was *10 mM* tri-amoniumhydrochloride (*Tris*) with a $pH = 7.5$. Figure 2.5 shows the chemical structure of poly-l-lysine, *PAH* and *PSS*.

---

[1]For all aqueous solutions water from a Millipore purification system (Millipore, Molsheim, France) with a specific resistance of $> 18\,\mathrm{M\Omega cm}$ was used.
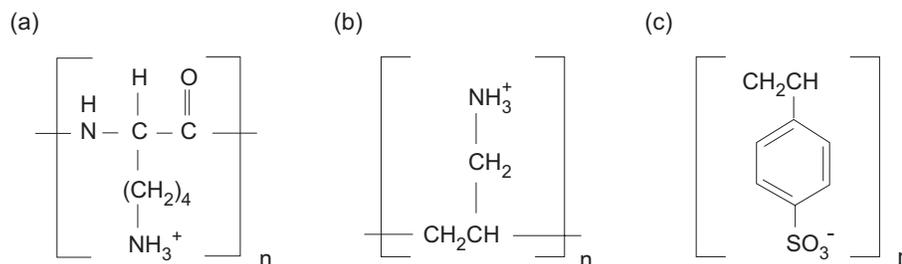
Figure 2.5: Chemical structure of the three molecules used for adsorption experiments of polyelectrolytes. (a) poly-l-lysine, (b) *PAH* and (c) *PSS*.

2.2.2.   Surface Passivation

In order to have a biocompatible and functional interface between a biological matrix and a solid support, organic self assembled monolayers (SAMs) are suited to provide a hydrophobic surface for the later modification. Moreover, these layers provide thin passivation layers that prevent the unspecific adsorption and surface decomposition on the one hand and minimize leakage currents on the other [Ulman, 1991]. For the experiments with a functionalized surface, the processed chips were cleaned and passivated before they were bonded and encapsulated in the chip carrier (see section 2.1). For the passivation of the SiO_2 surface, two different approaches were used, the spin coating of the surface with Poly-Methyl-MethAcrylate (*PMMA*) and the covalent binding of OctadecylTriMethoxySilane (*ODTMS*) to the surface. Before the passivation the surface was cleaned again.

Cleaning of the Surface

After the metallization, the SiO_2 surface was cleaned again. The cleaning consisted of the following steps:

- Ultrasonication (3 min) and subsequent rinsing with acetone and methanol.

- Ultrasonication in a solution of $1:1:5$ (v/v) ammoniumhydroxide (30 %) : hydrogenperoxide (30 %) : water for 3 min.

- Immersing the substrates in the same solution for another 30 min at $60\,^{\circ}C$ (adapted partially from RCA cleaning method [Kern and Puotinen, 1970]).

- Intensive rinsing with water (10 times).

After the cleaning, the surface was completely hydrophilic with contact angles below 10°. Unless the sensors were functionalized directly after the cleaning step, they were stored in glass boxes under vacuum ($p \approx 10^{-2}mbar$).

Covalent Immobilization of ODTMS

To get a covalently bound hydrophobic layer at the silicon oxide surface, <u>O</u>ctadecyl<u>T</u>ri<u>M</u>ethoxy<u>S</u>ilane (ODTMS) was used as a surface coating. Figure 2.6 shows the chemical structure of ODTMS and a schematic illustration of the chemical reaction to hydrophobize the silicon oxide surface. The silane molecules are dissolved in dry toluene. They form covalent siloxyl bonds with the surface offering hydroxyl groups. During this bond formation, they loose their methoxy headgroups to the solution. The quality of the silanization strongly depends on the preparation parameters. Substituting the methoxy sidegroups by active chloro- (Cl^-) groups increases not only the reactivity with the surface, but also increases the probability of covalent bond formation between different silane molecules in the bulk solution. Already small amounts of water in the solution lead to a polymerization of the silane molecules, while surface water blocks the hydroxyl groups at the surface. On the other hand, without any water at the surface, the surface groups can not be hydrolyzed. The temperature of the solution has to be kept in a certain range. Too high temperatures result in a gauche rotation of the alkyl chains and will hence hinder the formation of densely packed monolayers. At low temperatures, the alkyl chains will crystalize. For the formation of densely packed hydrophobic layers on the sensor surfaces the following procedure was used:

- Cleaning the substrates after the standard cleaning procedure as described above.

- Drying the substrates in vacuum over night to remove remaining surface water.

- Preparation of a mixture of dry toluene (solvent with molecular sieve, water content $< 0.005\%$) with $5vol\%$ ODTMS and $0.5vol\%$ Butylamine as catalyst.

- Immersing the sensors in this solution and sealing of the reaction container

- Ultrasonication for 60 min at a temperature of 14$^o C$.

(a)
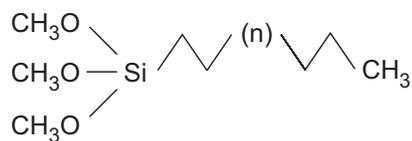
(b)
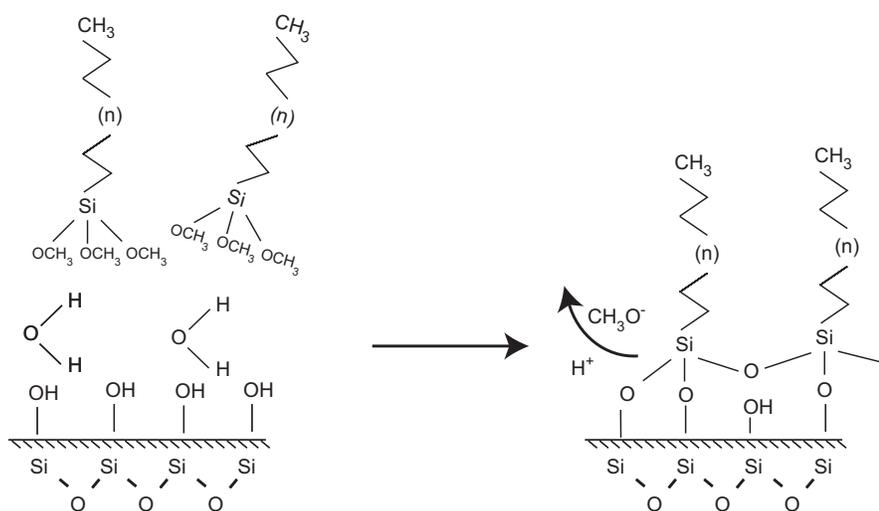
Figure 2.6: Chemical structure of ODTMS *(n=18)* used to hydrophobize the silicon oxide surface (a). Schematic illustration of the chemical reaction (b). Depending on the reaction parameters, the silanes at the surface bind to each other or to the silicon oxide surface.

- Incubating the sensors in the same solution for 30 min.

- Ultrasonication and intensive rinsing in pure toluene and methanol to remove remaining physisorbed and polymerized silane molecules.

Spincoating PMMA

Instead of using the covalent binding of ODTMS, a hydrophobic surface for the further functionalization can also be achieved by the deposition of polymer layers with the spin coating technique. However, the stability of the spincoated layers is not very

high and once water enters the region between the polymer layer and the hydrophilic substrate, the complete passivation layer will lift off. I tested the deposition of <u>P</u>oly-<u>M</u>ethyl-<u>M</u>eth<u>A</u>crylate (PMMA) to get a hydrophobic surface.

Before the spin coating, the sensor surfaces were cleaned after the standard cleaning method as described above. The sensors were deposited on the spin coater and covered with a drop of toluol. The toluol was removed by spinning the sensor at a speed of *1000 rpm* for *60 s* and subsequent blowing with nitrogen. For the spin coating of the passivation layer, PMMA (P.S.S., Germany, $M_w = 31.000$) was dissolved in toluene at a concentration of $1mg/ml$. Approx. *1 ml* of this solution was put on the device and spun at *1000 rpm* for *60 s*. After additional blowing with nitrogen, the hydrophobic samples were stored in glass boxes under vacuum until the encapsulation (see Section 2.1).

2.2.3. Preparation Methods for Lipid Membrane Experiments

The preparation of supported lipid membranes is very well established [Sackmann, 1996] and a lot of work has been dedicated to the optimization of the experimental methods. Supported lipid layers can come about in two forms, as bilayers on hydrophilic substrates and as monolayers on hydrophobic substrates. Both forms were used as functionalization layer and the preparation techniques used to form these layers will shortly be described in this section.

All lipids were purchased from *Avanti, Inc., USA* and stored in chloroform at $-18^{\circ} C$. Figure 2.7 shows the chemical structure of the different components of the lipid membranes used in this thesis. For both, lipid mono- and bilayers, a mixture of DMPC [2], cholesterol and DOGS-NTA [3] was used.

Preparation of Lipid Bilayers

Several preparation techniques are available to establish a lipid bilayer on a solid support.   Asymmetric bilayers can be prepared by the subsequent deposition of two monolayers with the Langmuir-Blodgett and the Langmuir-Schäfer transfer from the air/water interface [Kuhner et al., 1994, Sigl et al., 1997, Tamm and McConnell, 1985, Elender et al., 1996]. Although this technique is best suited for the preparation of asymmetric bilayers, it is experimentally very complicated and time consuming. A simpler approach to get bilayers is the implementation of self organized processes like solvent exchange [Lang et al., 1994] or direct spreading [Nissen et al., 1999, Rädler and Sackmann, 1997].

If proteins should be incorporated into the supported membrane, the fusion of small unilamellar vesicles containing these molecules is suitable [Cornell et al., 1997, Stelzle et al., 1993, Salafsky et al., 1996]. The formation of the bilayers is believed to occur in three steps: (i) adhesion of vesicles (ii) bursting and (iii) membrane spreading into patches towards the formation of homogenous layers. In this thesis, the vesicle fusion technique was used to form supported membranes on hydrophilic SiO_2 surfaces.

The desired amounts of lipids in chloroform solution were mixed in a glass flask to yield a total lipid concentration of *1 mg/ml* solution. Afterwards, the solvent was

---

[2]1,2-dimyristoyl-sn-glycero-3-phosphocholine
[3]1,2-dioleoyl-sn-glycero-3-{[N(5-amino-1-carboxypentyl) iminodiaceticacid]succinyl)}

(a)

(b)

(c)
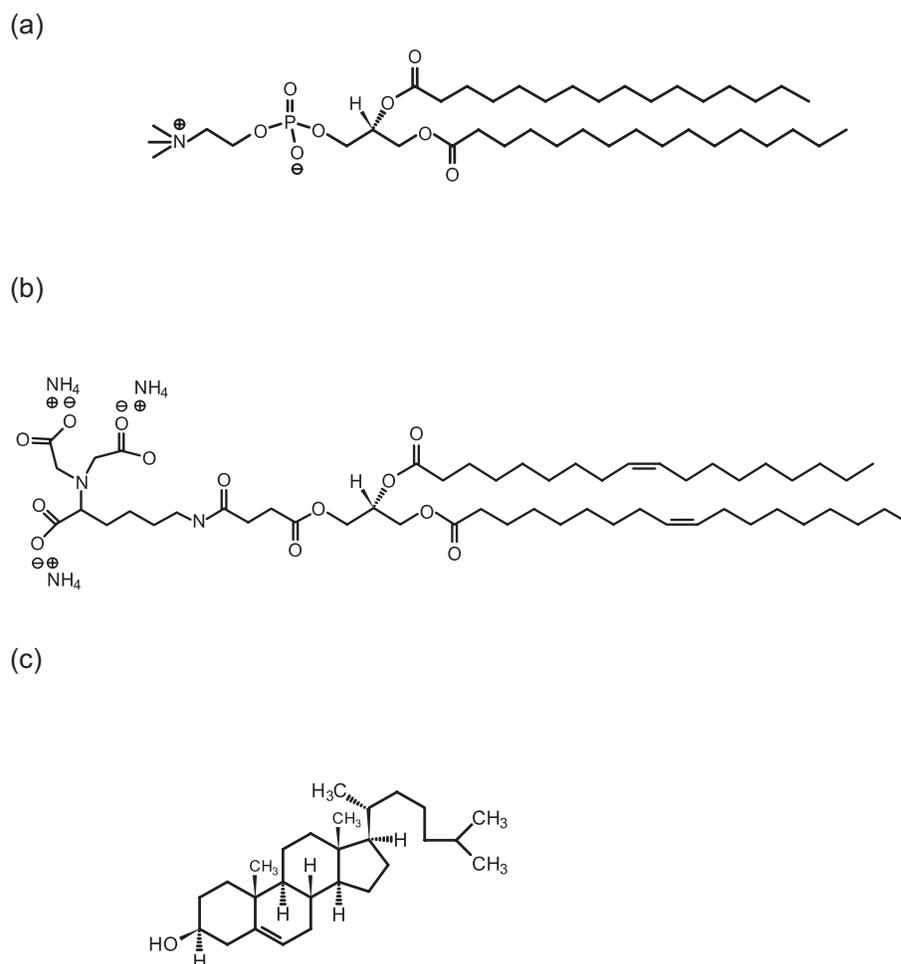
Figure 2.7: Chemical structure of DMPC (a), DOGS-NTA (b) and cholesterol (c).

evaporated under nitrogen and the glass was stored under vacuum over night. The dried lipids were dissolved in degassed standard *PBS* buffer to a final concentration of *1 mg/ml* and were stored at a 37° *C* for 2 hours. During this time, the lipids self-assemble into multilamellar vesicles. Finally, this mixture was sonicated for 10 minutes to get unilamellar vesicles. Directly after that, the vesicles were injected in the flow chamber on top of the sensor surface. After incubation for app. 2 hours, the formation of the bilayer was done and the chamber was rinsed extensively with buffer solution to remove remaining vesicles from the surface and from the bulk solution.

Preparation of Lipid Monolayers

On hydrophobic substrates, lipid monolayers with the headgroup facing to the electrolyte bulk can be deposited as biomimetic model system for the outer leaflet of a biological membrane. For an electronic sensor, this has the advantage that no residual water and hence no screening of the charges appears between the substrate and the lipid layer. Many techniques can be used to form a lipid monolayer on a hydrophobic support, such as vesicle fusion [Dorn et al., 1998, Plant, 1993, Plant, 1999], the Langmuir-Schäfer technique [Parikh et al., 1999] and the self organized assembly from ethanol or other solvents [Miller et al., 1990, Florin and Gaub, 1993, Steinem et al., 1996]. The monolayers on hydrophobic substrates used in this thesis were prepared after this 'solvent exchange' method.

The desired amounts of lipids in chloroform solution were mixed in a glass flask to yield a total lipid concentration of *1 mg/ml* solution. Afterwards, the solvent was evaporated under nitrogen and the glass was stored under vacuum over night. The dried lipids were dissolved in ethanol to a final concentration of *1 mg/ml* and injected into the chamber. The spontaneous formation of the lipid monolayer was initiated by rinsing the chamber with degassed standard buffer with a flow rate of $10\mu l/s$. A peristaltic pump (ISMATECH, Germany) applied this flow for *10 s*, followed by a rest time of *90 s*. After approx. 2 hours, the chamber was rinsed with buffer to remove all residual lipids and ethanol.

Membrane Based Charge Sensor and Protein Binding Experiments

The chelator lipid system used in this work consisted of DMPC, cholesterol and DOGS-NTA. The NTA headgroups of the DOGS lipids can be used to reversibly bind a protein via histidine-tag [Schmitt et al., 1994, Dietrich et al., 1995]. Moreover, the DOGS-NTA lipids themselves already provide an easy test system for the performance of the SOI sensors, as they can be charged and decharged upon exposure to different buffers.

The functional NTA headgroups of the lipid layers can be charged with divalent nickel ions and decharged by removing these nickel ions from the headgroups. The removal was done by adding a strong competitor for divalent ions. In this work, <u>E</u>thylene<u>D</u>iamine<u>T</u>etraacetic<u>A</u>cid (EDTA) was used. Nickel buffer consisted from $10\,mM\,PBS$ buffer with $1\,mM\,NiCl_2$ and $150\,mM$ KCl added for the equilibration of the two buffers on the DMPC monolayer. The EDTA buffer contained $50\,mM$
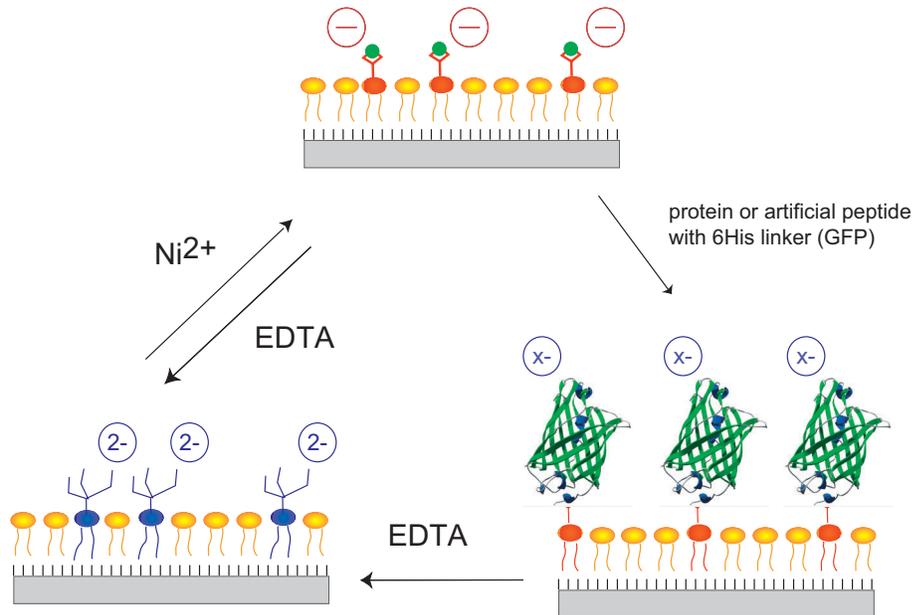
Figure 2.8: Model membrane system as deposited on the sensor devices. Upon buffer exchange, the net charge change of the functional lipids is $1\,e^-$ per NTA-headgroup. From the complexed state, His-tagged proteins are bound specifically to the metal complex [Schmitt et al., 1994].

EDTA in $10\,mM$ PBS. Both buffers were adjusted to $pH = 7.5$ and simply injected into the flow chamber. For the binding of the His-tagged proteins, a concentrated solution of protein containing buffer (Standard PBS, $c_{protein} = 0.2\,mg/ml$) at $pH = 7$ was used. Figure 2.8 shows a sketch of the model membrane system as used in this thesis. The functional headgroups can be charged and decharged on a molecular level. In the complexed state, the chelator lipids specifically bind Histidine-tagged proteins. By adding a strong competitor for the divalent Nickel ions, the chelator complex is opened again and the surface is reset.

2.3   Measurement Setup and Method

2.3.1.   Experimental Setup

Measurement Method

An encapsulated chip can be used in a commercial IC socket for the sensor measurements. The IC socket is soldered on a conductor board and every lead is connected to a *BNC* connector. Consequently, every single contact on the chip can be contacted separately. The measurement of the sheet resistance is carried out in 4 point geometry, to be independent of the contact resistance of the metallization. Figure 2.3.1. (a) shows a sketch of the sensor. A current is applied from source to drain (I_{sd}) and the voltage drop between two contacts (V) along the hallbar is measured. A back gate voltage (U_{bg}) at the back contact and a voltage applied at the reference electrode (U_{ref}) immersed in the electrolyte on top of the native oxide, is used to control the charge carrier density in the channel and the potential of the electrolyte. The geometric design of the active hallbar in the middle was planned to yield a sheet resistance normalized to a quadratic area, if the voltage drop was measured between two adjacent contacts. Consequently, all sheet resistance measurements were normalized to the number of squares, yielding the square resistance. All measurement instruments were connected and operated with a computer over an IEEE-GPIB interface. The measurement software is self written with *Labview* and is described in detail in the appendix.

In figure 2.3.1.(b), the principle wiring diagram is shown. For the sensor measurements, an additional flow chamber was put on top of the sensor. The back gate voltage (U_{bg}) is applied with an *Agilent E3647A* voltage source, the source-drain voltage (U_{sd}) is applied between the source and the drain contact with a *Keithley K2400* source-meter, which also measures the source-drain current I_{sd}. The potential of the reference electrode is controlled with a second *Keithley K2400* source-meter and the voltage drop V between two contacts along the hallbar is measured with a *Keithley K2000* voltmeter. In addition, the leakage current over the buried oxide to the substrate is measured with a second *Keithley K2000* multi meter.

The conductivity of the channel is influenced by the two gate voltages (U_{bg}, U_{ref}) and the condition of the surface (electrolyte, charged molecules, etc.). For a constant set of parameters (U_{bg}, U_{ref}, surface condition), the resistance is determined by measuring a complete current-voltage characteristic of the sensor layer. The source-drain
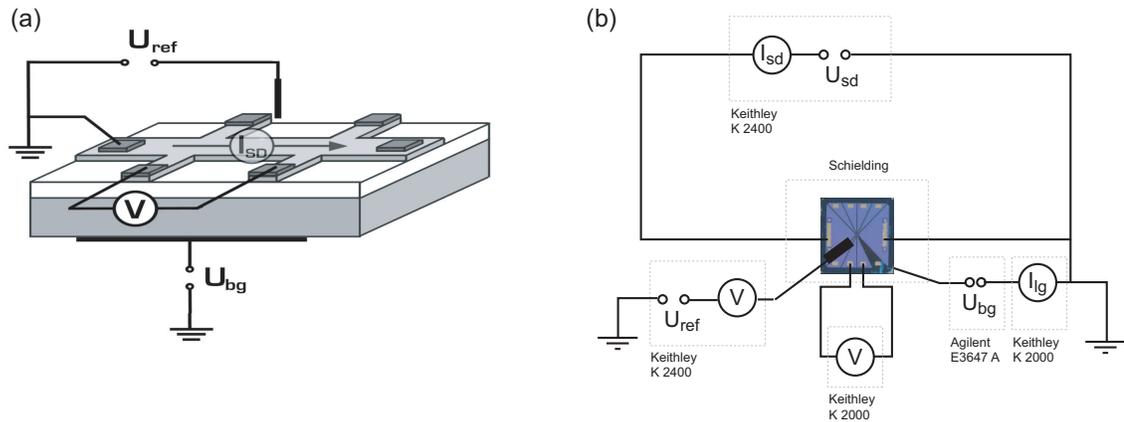
Figure 2.9: Scheme of the measurement setup (a). The sheet resistance was measured by applying a current from source to drain and measuring the voltage drop along the hallbar. A back-gate voltage applied to the substrate, and a front-gate voltage applied to the electrolyte solution on top of the native oxide were used to control the charge carrier concentration in the sensor channel. (b) shows the wiring diagram for the measurement of the sheet resistance. All measurement instruments were computer controlled. For sensor measurements, a flow chamber containing the $Ag/AgCl$ reference electrode was used.

voltage is varied between two limits and the number of intermediate points is chosen according to the measurements needs. Two characteristics were recorded, the two point characteristic (U_{sd} vs. I_{sd}) and the four point characteristic (V vs. I_{sd}). The two and four point resistance is given by the slope of these characteristics. The slope is calculated with the formula for linear regression for n measurement points $U_i(I_i)$

$$R = \frac{n \sum_{i=1}^{n} I_i U_i - \sum_{i=1}^{n} I_i \sum_{i=1}^{n} U_i}{n \sum_{i=1}^{n} I_i^2 - \left(\sum_{i=1}^{n} I_i\right)^2} \tag{2.2}$$

Thus, every complete current-voltage characteristic yields one two point resistance value $R_2(U_{sd}; I_{sd})$ and one four point resistance value $R_4(V; I_{sd})$.

To get good statistics, many characteristics are measured and the resulting resistance is time averaged. Depending on the desired accuracy, the number of characteristics for one constant set of parameters (U_{bg}, U_{ref}, surface condition) is chosen. After that, the set of parameters is changed and the resistance is recorded again for the new set.
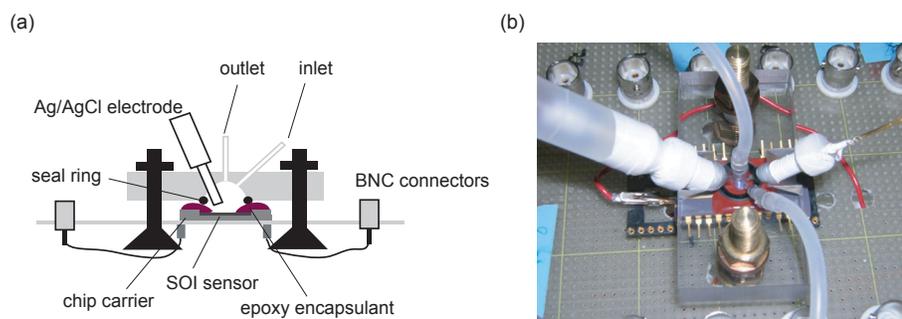
Figure 2.10: Sketch of the flow chamber for the application of the electrolyte solutions (a). The
sensor was plugged into an IC socket soldered on a conductor board. The metal contacts
were connected to the carriers leads and they were soldered to *BNC* plugs. Part (b)
shows a picture of the the flow chamber on top of the chip. The reference electrode
and a gold electrode for later electrochemical measurements are directly screwed into
the flow chamber.

Flow Chamber and Conductor Board

For the sensor measurements, an especially designed flow chamber is put on top of
the encapsulated sensor. Figure 2.10 (a) shows a sketch of the flow chamber on top
of the encapsulated sensor. To inject electrolytes into the chamber, it has an outlet
and an inlet connected with a tubing system. If necessary, the tubing was connected
to a syringe or a peristaltic pump to apply constant flow rates. The chamber also
contains the Ag/AgCl reference electrode and a gold electrode. The chamber can be
mounted on top of the sensor already plugged into the IC socket on the conductor
board. Figure 2.10 (b) shows an image of the chamber with the reference electrode,
the conductor board and the *BNC* plugs for the connection to the measurement
instruments.

2.3.2. Measurement Software

To control the different measuring instruments, a measurement program was written with *Labview*. Figure 2.11 shows a screenshot of the front panel. In this panel, all relevant parameters can be controlled and the obtained characteristics can be monitored online. The square resistance is calculated by the software, so that resistance changes can also be observed online. The software writes all relevant data into designated folders on the computer for later analysis with data processing software. In the appendix, a detailed manual for the software program is included.
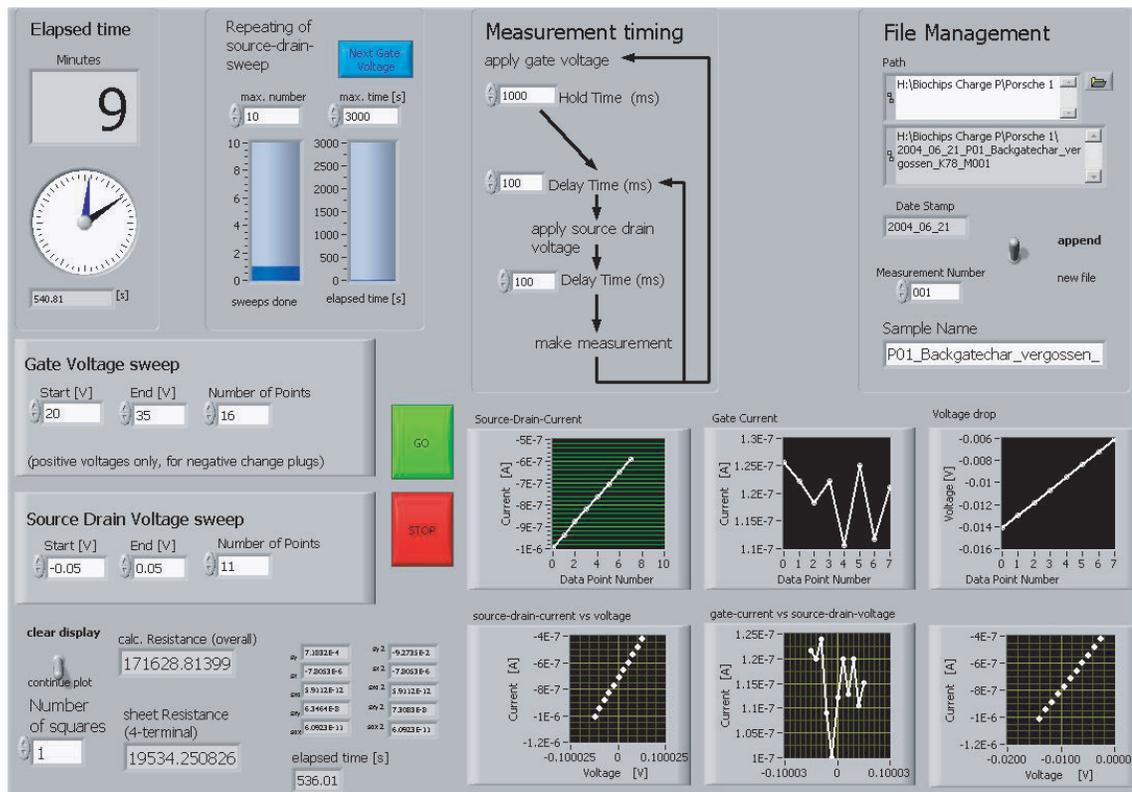
Figure 2.11: Screenshot of the front panel of the measurement software. In the upper left part, the relevant parameters can be set. In the top part, the file management can be done. In the lower part, the results are shown in numbers (left) and in graphical form (right).

2.3.3.   Backgate Characterization - Definition of the Working Point

The dependance of the sheet resistance from the applied back gate potential (U_{bg}) was obtained by measuring the sheet resistance as described and changing the applied back gate voltage. Typically, for each back gate potential, 25 characteristics were averaged. Figure 2.12 (a) shows a typical measurement of the resistance versus time for varying back gate voltage at constant front gate potential. To minimize the drift of alkali ions into the sensor material, only positive back gate voltages were used. For positive back gate voltages, the resistance decreased for increased U_{bg}. In the experimental setup,
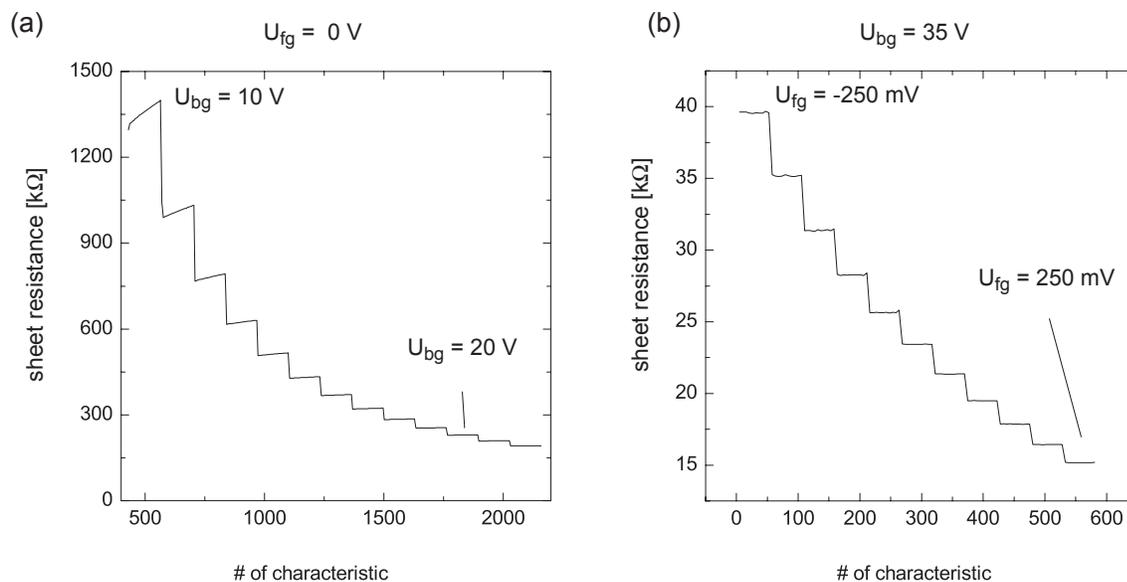
Figure 2.12: (a) shows a typical curve for the resistance versus time, when the back gate potential is varied at a constant front gate potential. (b) shows a typical calibration curve, i.e. the sheet resistance versus time at a constant back gate potential for varying front gate potential.

the back gate contact consists from conducting glue on the oxide of the wafer backside. Because of this experimental detail, it is not possible to estimate the potential which really governs at the interface between the substrate wafer and the buried oxide. This means that a direct comparison of the experimental data to the simulation is not possible. This fact will be discussed in more detail in section 3.1.1.

The back gate characterization was used to define the working point. As in the later sensor experiments the voltage drop between adjacent hallbar contacts should be

negligible compared to the change in surface potential caused by the surface reaction, the source drain voltage was kept in the mV range. For mV voltages, the DC current gets very small in the case of small U_{bg} and due to the imperfect shielding, the current voltage characteristics became non linear due to random noise. Therefore, at the working point, a compromise between this noise and a sensitivity still high enough to detect binding events at the front interface was made. The sensor measurements were taken at this constant back gate potential. Typically, for the undoped sensors the working point was between $U_{bg} = +15V$ and $U_{bg} = +25V$, for the doped sensors it was at $U_{bg} = 0V$.

2.3.4. Frontgate Characterization - Calibration Measurement

In order to relate the square resistance to the potential at the electrolyte/sensor surface interface, the potential of the electrode immersed in an electrolyte buffer was varied. For the back gate potential chosen as working point, the reference potential was varied between two limits. The resulting $R(U_{ref})$ curves can be used as calibration in the interpretation of the data. However, as the voltage drop over different electrolytes and the interfacial resistance of the several liquid/solid junctions are not exactly known, these calibration curves can be shifted with respect to the voltage axis. The size of this voltage offset can be obtained as fitting parameter. A sample curve of the resistance change for a constant back gate voltage if the front gate potential is varied, is shown in figure 2.12 (b). For the maesurements with the native oxide surface, the calibration was done with electrolyte on top of the native oxide, for the OTMS covered sensors, the calibration was done with the electrolyte on top of the ODTMS covered surface.

Even if the absolute value of the surface potential is not known from such a calibration measurement, changes of the sheet resistance ΔR are related uniquely to changes in the potential $\Delta \psi$, because the front gate characteristics are almost linear for the range of the sensor measurements.

3 Results I - Sensors with Native Oxide Surface

3.1 Electrical Sensor Characterization

To optimize the sensitivity and to interpret the measured changes of the sheet resistance, it is crucial to achieve a detailed understanding of the sensor performance and characteristic. In this section, theoretical as well as experimental data of the sensor performance will be presented and analyzed. It will be shown that the the back gate voltage can be used to vary the sensitivity of the device. Furthermore, a reference electrode immersed in an electrolyte solution on top of the native oxide can be used to calibrate the sensor.

3.1.1. Simulation of the Sensor with $nextnano^3$

The simulation software $nextnano^3$ [Vogl et al., 2004] calculates the band structure and the charge carrier density of semiconductor materials in one, two and three dimensions. Most of the sensor measurements were done with the undoped sensors and therefore the simulation of these structures will be discussed here. Basic understanding of the performance of the SOI-sensor can already be obtained with the simulation of a one dimensional structure as shown in figure 3.1 (b). The metal back gate contact is placed directly on the buried oxide of $200\,nm$ thickness. The sensor layer is $30\,nm$ thick and boron doped ($10^{16}cm^{-3}$). The structures are covered with a native oxide of $2\,nm$ thickness and a front gate metal electrode.

The simulated device differs from the original device structure due to the fact, that the simulation software in the status used here was not able to handle two isolated conducting materials in parallel as represented by the channel SOI and the substrate wafer. Therefore, the substrate wafer (thickness $\approx 650\,\mu m$) was left out. Moreover, the calculation setup and the real device differ in several points.

- The back gate contact in the experimental setup consists of a silver conductive

(a)

metal SiO$_2$ silicon   SiO$_2$ silicon SiO$_2$ electrolyte electrode

(b)

metal   SiO$_2$ silicon   SiO$_2$ metal
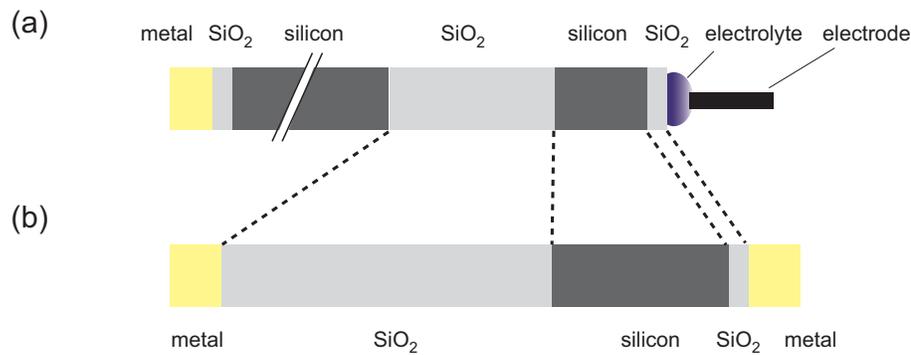
Figure 3.1: Comparison of the real device (a) and the layer structure used to simulate the sensor device in the calculations (b). The simulation layer structure reads from top to bottom: gold electrode (*5nm*), native oxide (*2 nm*), silicon sensing layer (*30 nm or 80 nm*), buried oxide (*200 nm*), back electrode (*5 nm*).

lacquer on the rough back surface of the wafer, which is also covered by native oxide.

- The front gate is not applied with a metal electrode but with an electrode immersed in an electrolyte solution on top of the surface.

- An applied back gate voltage also falls off over the substrate wafer, not included in the simulation setup.

Consequently, the simulation data can only give a qualitative understanding of the sensor and all simulation data can be shifted with respect to the voltage axis. The direct comparison between experiment and simulation is not possible with this simulation, but qualitative trends can be deduced from the simulations and will also be verified experimentally in the next sections.

The simulation of the device yields the charge carrier concentration in the channel and from that, the sheet resistance can be calculated. In the experiments, only positive back gate voltages were used to minimize the diffusion of alkali ions from the electrolyte into the sensor material. Consequently, the simulation was only done for positive back gate voltages and as an example two different positive back gate voltages (*+10 V* and *+20 V*) will be compared to yield a qualitative understanding of the sensor performance.
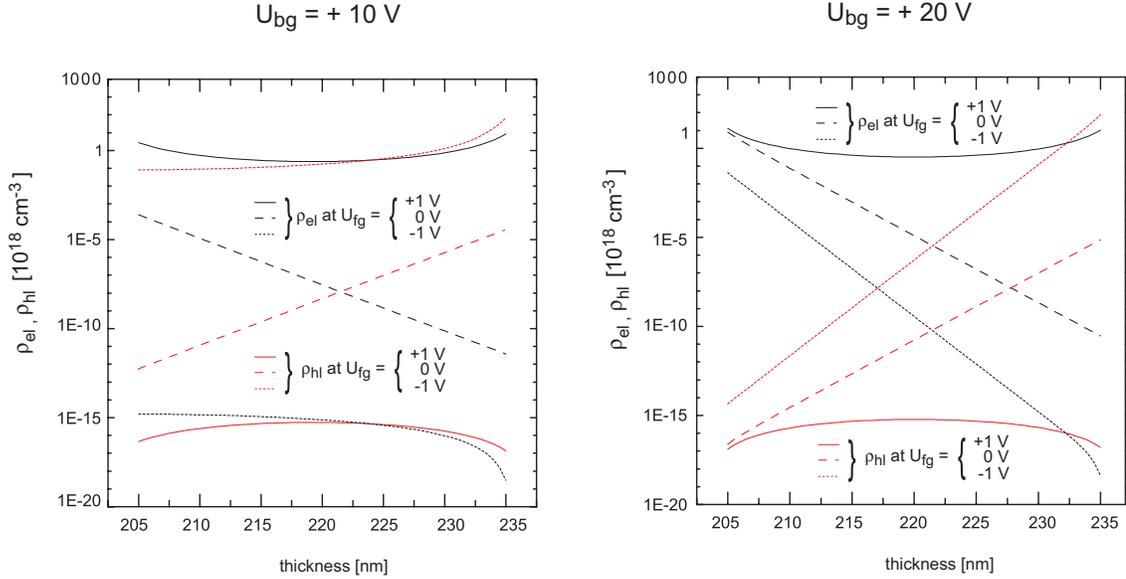
Figure 3.2: Charge density in the *30 nm* thick silicon sensing layer for a back gate voltage of $+10V$ (left) and $+20V$ (right). Three different front gate voltages are shown (*+1V, 0V, -1V*).

In figure 3.2, the simulated electron and hole densities in the $30\,nm$ thick conducting layer are shown for back gate voltages of $U_{bg} = +20V$ and $U_{bg} = +10V$. For both back gate voltages, three different applied front gate voltages (*+1V, 0V, -1V*) are distinguished.

For $U_{bg} = +20V$, the electron density (black) at the back interface is at least *13* orders of magnitude higher than the density of holes (red) and hence the back interface is in inversion for all applied front gate voltages. Contrary, at the front interface either electrons or holes are the dominant charge carriers, depending on the applied front gate potential. For *+1 V* front gate voltage, the electron density is higher than the hole density, but for front gate voltages of *0 V* and *-1 V*, holes are the dominant charge carriers. In other words, a back gate voltage of *+20 V* results in a high charge carrier density at the back interface and in a small screening length. This in turn means that a change of the front gate voltage mainly influences the charge carrier distribution at the front interface and hence the effect of such a change on the overall resistance of the conducing channel is relatively small.

In comparison, on the left side of figure 3.2, the simulated electron and hole densities in the $30\,nm$ thick conducting layer are shown at a back gate voltage of $U_{bg} = +10V$. In this case, the whole layer is now influenced by variations of the front
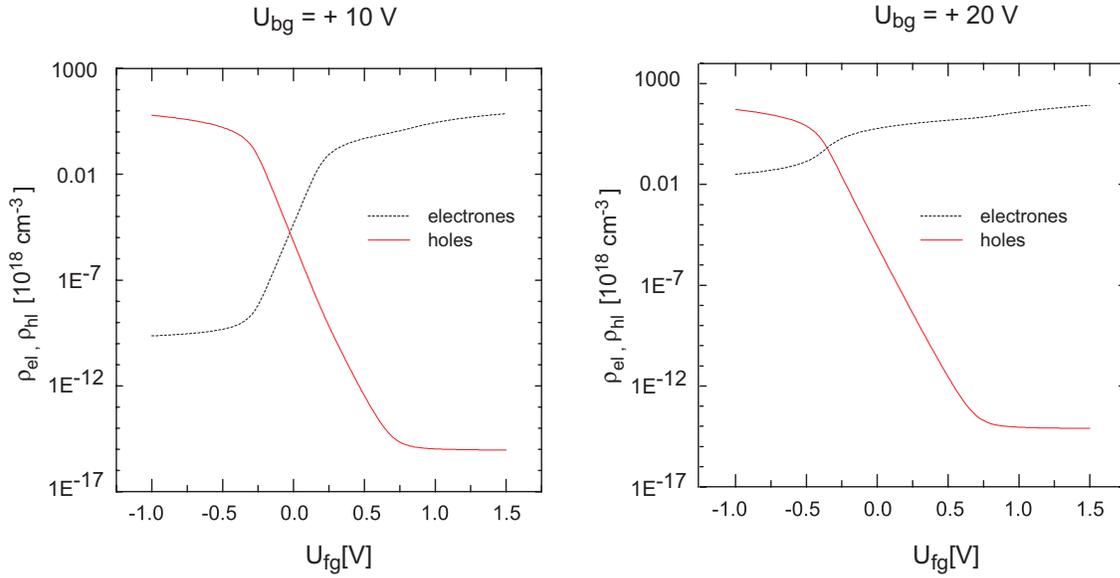
Figure 3.3: Integrated charge carrier density for a back gate voltage of $+10V$ (left) and $+20V$ (right).

gate voltage. For $+1$ V, the electron density is higher than the hole density over the complete layer and hence the complete layer is in inversion. For $U_{fg} = 0V$, the back interface is in inversion, but at the front interface the hole concentration is higher than the concentration of electrons. For -1 V applied front gate potential, the hole density is higher over the complete layer and hence the complete layer is in the state of accumulation. In other words, a smaller back gate voltage of only $U_{bg} = +10V$ results in a smaller charge carrier concentration at the back interface and consequently in a longer screening length. Therefore, variations at the front interface have an influence over the complete layer and hence should have a stronger effect on the overall channel resistance. Extrapolating this result, the sensor should have a higher sensitivity for a lower applied back gate voltage. This trend will be verified by the experimental data in section 3.1.3.

In order to get the sheet resistance, the charge carrier densities have to be integrated

$$\rho_{e,h}(U_{fg}) = \int_{x=205\,nm}^{x=235\,nm} \rho_{e,h}(x) dx \qquad . \tag{3.1}$$

Figure 3.3 shows the results for the two already discussed back gate voltages of

$U_{bg} = +10\,V$ and $U_{bg} = +20\,V$. The results are shown for front gate voltages between $U_{fg} = -1\,V$ nd $U_{fg} = +1.5\,V$. In both cases, the crossover point, i.e. the point when the density of electrons gets bigger than the density of holes and hence the dominating charge carrier species changes, is interesting. For $U_{bg} = +20\,V$, this point lies at a front gate potential of $U_{fg} = -0.3\,V$. For $U_{bg} = 10\,V$, the cross over point occurs at roughly zero front gate potentials. As the simulated device and the real sensor differ in the above mentioned points, potentials applied at the reference electrode U_{ref} are not identical to the potentials applied at the front metal contact U_{fg}. Therefore, the information about the main charge carriers involved in the sensor measurements has to be obtained indirectly by first calculating the square resistance after equation 1.20. The calculated square resistance against applied front gate potential is shown in figure 3.4.

For $U_{bg} = +10\,V$, the resistance increases with increasing front gate potential up to a value of $6 \cdot 10^7\,\Omega/square$ at approx. zero front gate, due to the depletion of holes in the sensor layer. For higher front gate potentials, the layer starts to be inverted and more and more electrons contribute to the current transport, resulting in a decrease of the resistance.

For $U_{bg} = +20\,V$, the maximum occurs at $15 \cdot 10^3\,\Omega/square$ and approx. $-0.3\,V$ front gate potential.

In the experiments, for the positive back gate voltages used, the $R(U_{ref})$ characteristics of the undoped sensors always have a negative slope (see chapter 3.1.4.). Therefore, one can conclude that the sensor is operated on the right side of the maximum of the curves in figure 3.4 for both back gate voltages. Comparing the position of the maximum in these curves with the crossover point in the integrated charge carrier densities (Figure 3.3) shows that electrons are the main charge carriers in the experimental measurements and therefore all sensor measurements are done with electrons as the main charge carriers.

This information becomes important for the production of sensors with doped contact regions in a further development of the sensor. As electrons are the main charge carriers, a n-doping of the contact regions is necessary to obtain a device being conductive for positive U_{bg}. From figure 3.4 it is also evident, that the sensitivity, i.e. the slope of the $R(U_{fg})$ curve is higher for lower U_{bg}. Summarizing, from the simulation data several points can be concluded.

- The sensor measurements are done with the thin layer in inversion, i.e. electrons
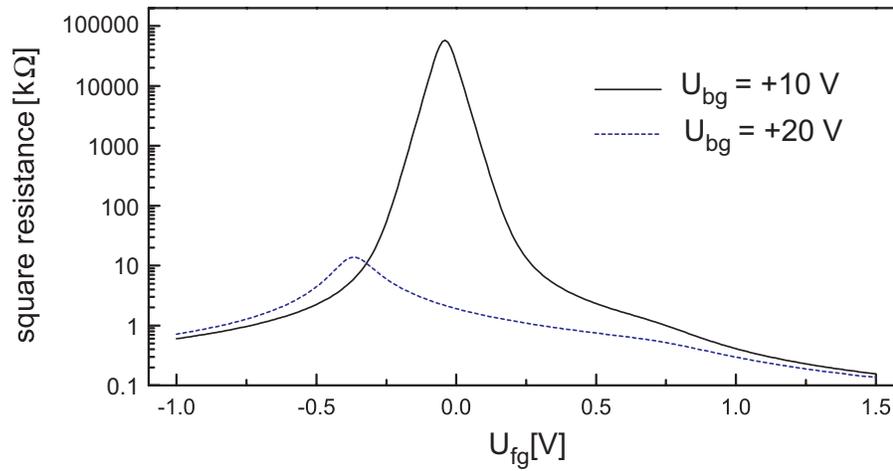
Figure 3.4: Simulated square resistance vs. front gate potential for $U_{bg} = +10V$ and $U_{bg} = +20V$. An increase in the back gate voltage decreases the overall resistance and also decreases the sensitivity towards surface events, i.e. the slope of the $R(U_{fg})$ curves is lower.

contribute the main part to the electrical conductivity.

- For positive back gate potentials, the overall resistance decreases with increasing back gate voltage.

- For positive back gate voltages, the sensitivity of the thin layer towards surface events increases for decreasing back gate voltages.

However, in the real measurements, the higher sensitivity is accompanied by an increase in resistance and by increased noise due to random fluctuations of the DC current. Therefore, an intermediate back gate voltage has to be chosen as working point for optimal sensor performance. This issue will be discussed further in section 3.1.3.
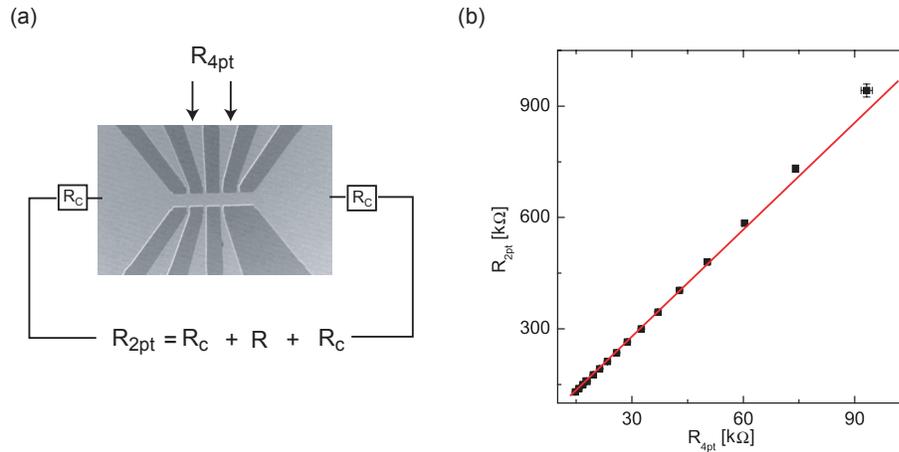
Figure 3.5: Measured 2 and 4 point resistance for back gate voltages between *+ 16 V* and *+ 30 V*. As expected for an ohmic contact, all data points lie on one line, showing that the metal contacts exhibit ohmic behavior.

3.1.2. Electrical Contacts

The electrical contacts to the thin sensor film were investigated in detail during this thesis and the results are described in detail in reference [Rauschenbach, 2002]. Summarizing, three different material systems were tested. First, a sandwich of $20\,nm$ Al and $200\,nm$ Au did not result in contacts with satisfying low contact resistances. It was shown by Rutherford back scattering (RBS) and secondary ion mass spectroscopy (SIMS) [Rauschenbach, 2002] that the gold diffuses through the aluminum layer into the sensor layer, destroying its sensing properties.

Second, pure Al contacts with $50\,nm$ thickness were tested. These contacts had satisfying low contact resistances, but were mechanically not stable. Moreover, they did not withstand the chemistry necessary to further functionalize the sensor surface.

Hence, a third system, consisting from $200\,nm$ Au on top of $20\,nm$ Ti was used. These contacts were characterized electrically by measuring the two point (R_{2pt}) and the four point resistance (R_{4pt}) as shown in figure 3.5 (a). In this setup,

$$R_{2pt}(U_{bg}) = 2R_c + g \cdot R_{4pt}(U_{bg}) \qquad , \qquad (3.2)$$

where R_c is the contact resistance and g is a geometric factor depending on the structure of the sensor device only. If the contacts are ohmic, R_c does not depend on the applied back gate potential and therefore all data point will lie on a line. In

figure 3.5 (b) the measured resistance values are shown for back gate voltages between $U_{bg} = +16V$ and $U_{bg} = +30V$. Obviously, the contacts are almost perfectly ohmic for $U_{bg} > +18\,V$ and from the data the contact resistance can be obtained to be $< 10k\Omega$ and the geometric factor $g \approx 9$ if the four point resistance is measured between two adjacent hallbar contacts.
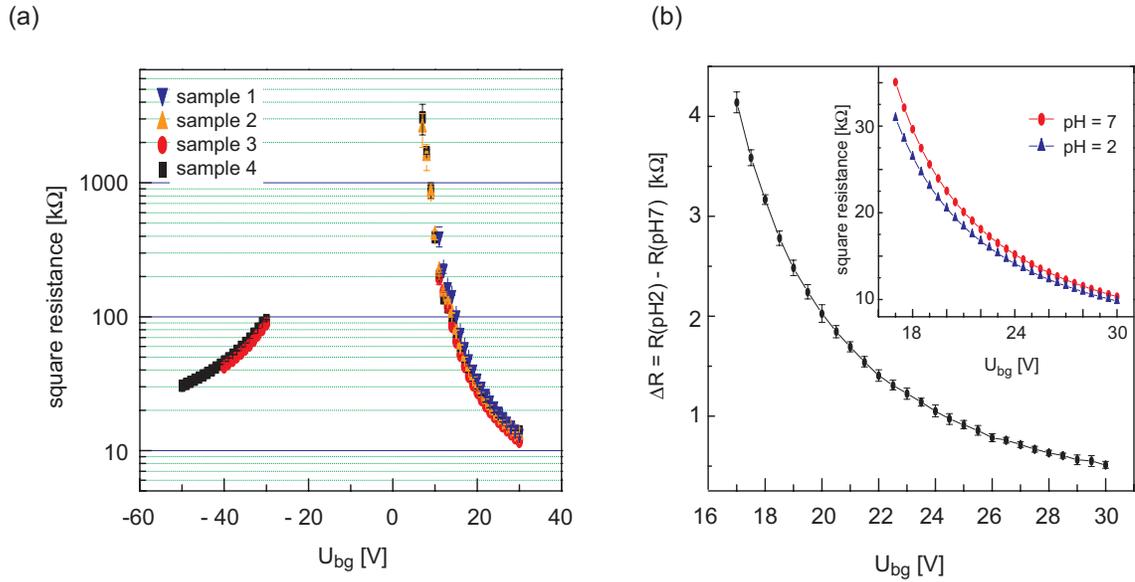
Figure 3.6: (a) Measured square resistance for varying back gate potential. The resistance of the thin sensing layer depends strongly on the applied back gate voltage. The measurement was done with the front surface of the sensor exposed to air at room temperature. Measured change in resistance if the pH of the solution was changed from pH 2 to pH 7 (b). The inset shows the measured resistance.

3.1.3.   Backgate Characterization - Tunable Sensitivity

One main result of the simulation data in section 3.1.1. was that the sensitivity is dependant from the applied back gate voltage. In this section, the experimental data supporting this result will be presented.

In figure 3.6 (a), the dependence of the thin film resistance on the applied back gate voltage (U_{bg}) is presented. The measurements were carried out while the surface was exposed to air at room temperature. A variation of the back gate voltage drastically changes the resistance of the thin film resistor. The two separated regimes can be attributed to the an accumulation of holes in the layer (negative back gate potential) and to an inversion of the layer (positive back gate potential). (see also simulation results in section 3.1.1.).

In the intermediate regime, for $|U_{bg}| < 10V$, for a source drain voltage of $50\,mV$, random fluctuations of the DC current below $1\,nA$ were disturbing the measurement and the obtained current voltage characteristics were not linear.

The tunability of the sensitivity, as predicted from the simulation data can be measured by switching the surface condition between two states for different back gate voltages and comparing the measured resistance change. Figure 3.6 (b) shows the change in the resistance of the thin silicon layer, when the pH of the electrolyte is changed from $pH = 2$ to $pH = 7$ for back gate voltages between $U_{bg} = +16\,V$ and $U_{bg} = +30\,V$. As expected from the simulation data results, the signal is higher for lower back gate voltages.

This shows impressively the tunable sensitivity of the sensor by the back gate voltage. This back gate voltage dependance is used to define a working point for the later sensor measurements. In principle, a back gate voltage which generates the fewest charge carriers at the back interface of the sensor layer produces the highest signal. However, due to the fact that the noise level is getting more and more important for higher resistance values, a compromise between the highest signal and a low noise level was made to give the best signal to noise ratio. The working point was determined separately for every single sensor before the actual sensor measurements.

3.1.4.   Frontgate Characterization - Sensor Calibration

The surface potential at the electrolyte/semiconductor interface ψ_s controls the conductivity of the thin sensor layer. It is comparable to the gate potential of metal gate in a *MOSFET* device. In our setup, not the change of the surface potential ψ_s is measured but rather the change of the square resistance of the thin silicon layer. To relate these two parameters for a theoretical interpretation of the data, a calibration measurement is performed for every sensor at the back gate voltage chosen as working point. For the calibration measurement, the substrate is exposed to an electrolyte solution and the potential of a Ag/AgCl reference electrode (U_{ref}) immersed in the electrolyte is varied. The resulting $R(U_{ref})$ curve can be used for calibration in the interpretation of the later sensor measurements. Figure 3.7 (a) shows a typical calibration measurement of a native oxide covered sensor with a $30\,nm$ thick silicon layer with a doping concentration of $10^{16}cm^{-3}$) and a buried oxide thickness of $100\,nm$. The applied back gate voltage was $U_{bg} = +16V$. For this back gate voltage of $U_{bg} = +16V$, the slope was negative and almost constant $-50k\Omega/V$ for the range of applied front gate voltages.

As already predicted by the simulation data, the shape of the calibration curve
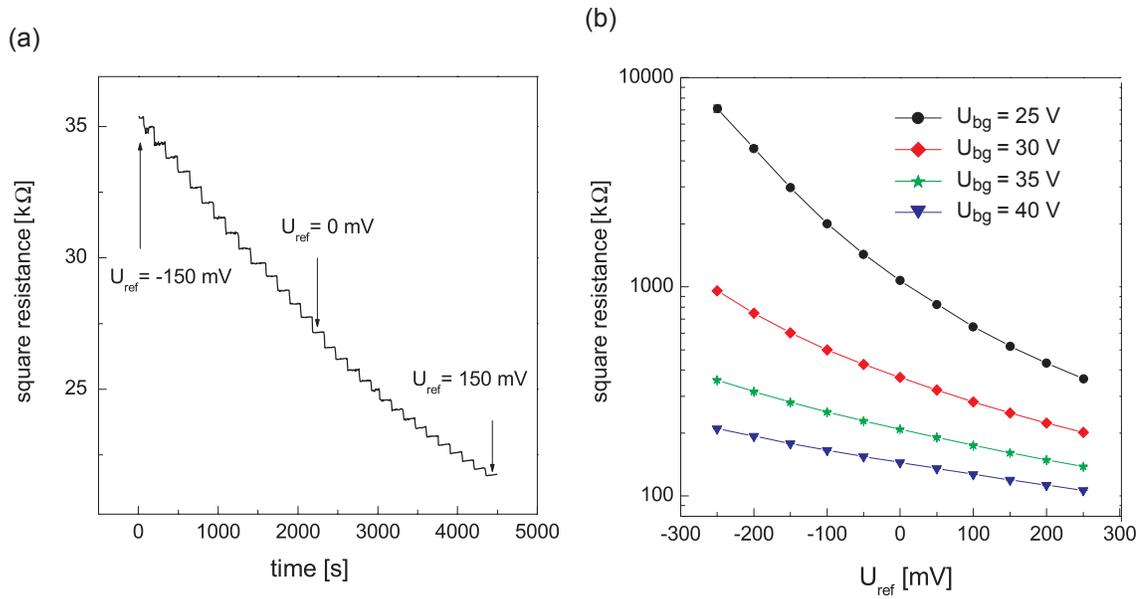
Figure 3.7: Measured change in resistance for a step like change of the applied voltage at the reference electrode for undoped sensor layer. The data was taken with a undoped sensor at a back gate voltage of $U_{bg} = +16V$. For these sensors, measurements were always performed in the linear regime of the $R(U_{ref})$ curves (a). (b) shows the change in resistance at back gate voltages of $U_{bg} = +25V$, $+30V$, $+35V$ and $+40V$ for ODTMS covered sensors. The resistance of the layer decreased with increasing back gate voltage and at the same time, the sensitivity towards front gate variations (i.e. the slope of the curves) decreased.

changes drastically when the back gate voltage or the doping concentration is varied. Figure 3.7 (b) shows the calibration curves for back gate voltages of $U_{bg} = +25V$, $+30V$, $+35V$ and $+40V$ for an ODTMS funtionalized sensor.

Comparing the predictions of the simulations in figure 3.4 with the experimental results in figure 3.7 (b) shows the qualitative agreement between theory and simulation. A higher back gate voltage decreases the overall resistance and at the same time the sensitivity, i.e. the slope of the $R(U_{ref})$ curves is decreased.

The slope of the calibration curves of the doped sensors (i.e. additionally overgrown by MBE, $c = 10^{18} cm^{-3}$) had the opposite sign, resulting in a higher resistance for higher U_{ref}, as shown in figure 3.8.

Even though from the calibration measurements the absolute value of the surface potential can not be determined, because the relation between U_{ref} and ψ_s is not known, changes in the sheet resistance ΔR can directly be related to changes in

(a)

(b)
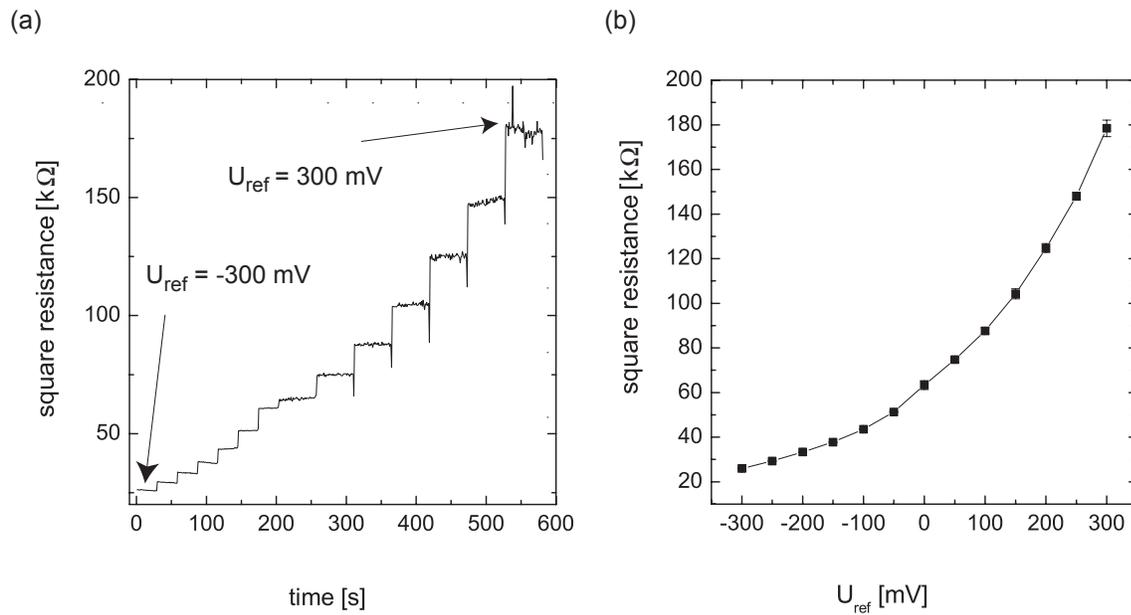
Figure 3.8: Measured change in resistance for a doped ($c = 10^{18} cm^{-3}$) sensor layer. The data was taken at a back gate voltage of $U_{bg} = 0V$. (a) shows the resistance for step like reference potential changes between $U_{ref} = -300mV$ and $U_{ref} = +300mV$. (b) shows the time averaged data against applied potential.

surface potential $\Delta\psi_s$, because the relation is almost linear for the range of the sensor measurements.

3.2 Measurements in Electrolyte Solutions

After the functionality of the sensor device has been tested in the measurement of the characteristics, i.e. the dependance of the resistance from the two gate electrodes, first sensor measurements in electrolyte solutions can be performed. As discussed in chapter 1.1, the surface potential of a charged surface immersed in an electrolyte is controlled by the surface charge density σ and the ionic strength of the solution. For SiO_2, the surface charge density is mainly controlled by the solution pH, so that the two parameters can be varied separately.

3.2.1. Variations of the Salt Concentration

For a constant pH value, the surface charge density of a SiO_2 surface in electrolyte solutions remains almost constant and the variation of the surface charge due to the specific adsorption of ions at the surface sites can be neglected. Therefore, the response of the sensor device towards variations of the salt concentration in an electrolyte of constant pH can directly be compared to the theoretical predictions of the *Grahame* equation (equation 1.5).

Figure 3.9 (a) shows the measured square resistance when the concentration of KCl is varied from *1 M* to *10 μM*. The pH of the solution was kept constant at a value of *6.4* with *10 mM* Phosphate buffer.

The sensor used in this study was p-doped with a boron concentration of $10^{18}cm^{-3}$, so that a higher resistance corresponds to a higher surface potential (See discussion in section 3.1.4.). Consequently, in agreement with the prediction of equation 1.5, for *1 M* monovalent salt solution, the surface potential is higher than for lower concentrations. With the help of the calibration measurement, the resistance changes can be related to relative changes of the surface potential.

Figure 3.9 (b) shows the time averaged resistance values from the measurement in figure 3.9 (a) along with the theoretical prediction of the Grahame equation (equation 1.5). For the theoretical calculation, a concentration of divalent buffer ions of *3.2 mM* or a dissociation of *20 %* and a surface charge density of $0.036\,C/m^2$. Both values are in good agreement with the literature values for a pH value of *6.4*, as used in this experiment [P. Atkins, J. de Paula, 2002, Sonnefeld, J. and Löbbus, M. and Vogelsberger, W., 2001].
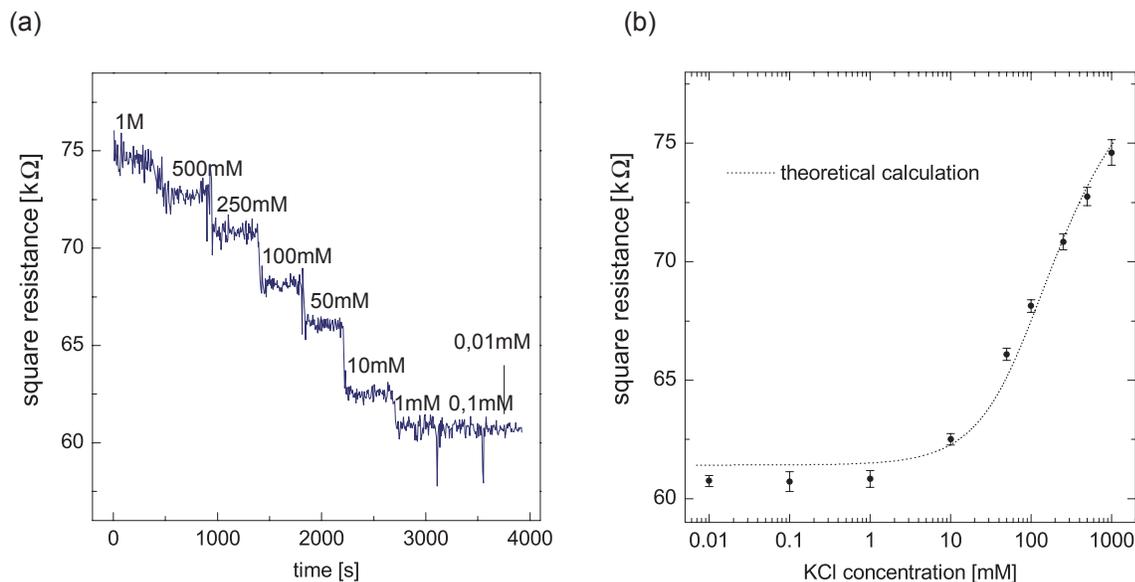
Figure 3.9: Measured square resistance on a doped sensor for a variation of the KCl concentration at $pH = 6.4$. The total concentration of buffer salts was *10 mM* (a). (b) shows the time averaged resistance against the concentration of monovalent salt. The broken line shows the prediction of the *Grahame* equation for a concentration of divalent buffer ions of *3.2 mM* or a dissociation of *20 %* and a surface charge density of $0.036\,C/m^2$.

3.2.2.   Variations of the Surface Charge Density

Detection of pH

As discussed in chapter 1, a variation of the pH value results in a change of the surface charge density σ at the SiO_2/electrolyte interface. If at the same time, the salt concentration is constant, the measured resistance change can be compared to the theoretical predictions of the site binding theory for SiO_2 surfaces (equation 1.16).

Figure 3.10 (a) shows the measured resistance for a pH variation between *4.9* and *9* with an undoped sensor at a backgate voltage of $U_{bg} = +16V$. In addition to *10 mM* phosphate buffer, the electrolyte contained *90 mM* KCl, to keep the salt concentration almost constant. A change in pH is detected instantaneously with high sensitivity. A linear fit to the response shows that each step in pH results in an instantaneous change of the square resistance of about $2.6\,k\Omega$. The calibration measurement for this device at $U_{bg} = +16V$ shows a relation of the square resistance to the surface potential of $-50k\Omega/V$. Therefore, a pH step of one unit corresponds
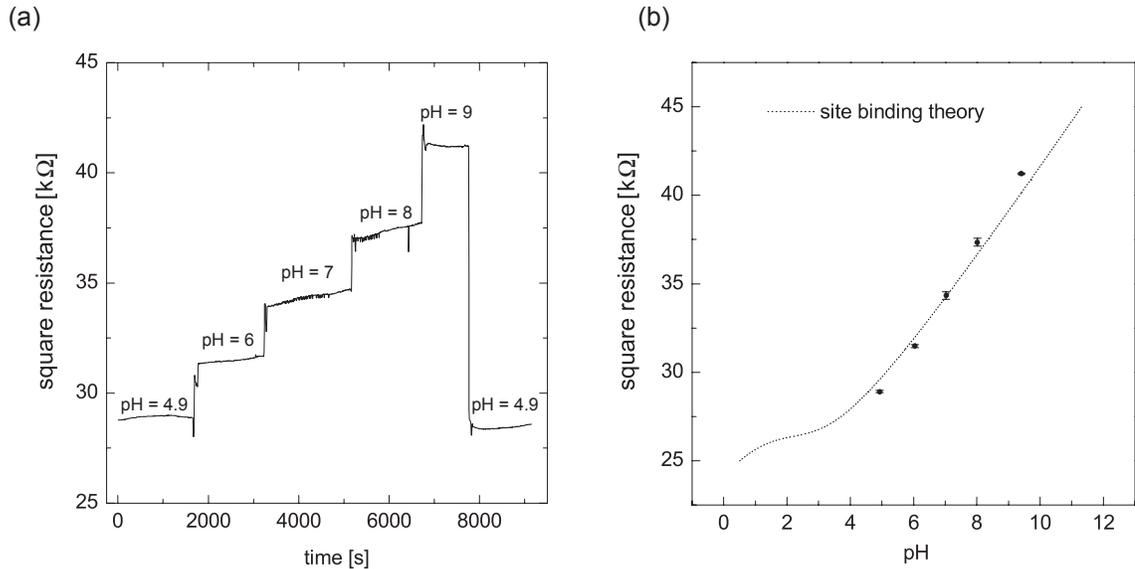
Figure 3.10: (a) Measured resistance change of a undoped sensor device for a backgate voltage of $U_{bg} = +16V$. The electrolyte contained *90 mM KCl* to keep the salt concentration constant. In (b), the comparison of the measured data with the theoretical predictions by the site-binding model is shown. The measured response (black dots) agrees very well with the theoretical predictions from the site-binding theory (broken line).

to a variation of the surface potential of $\Delta\psi/pH = -52mV/pH$.

Although some papers report similar close Nernstian responses [Siu and Cobbold, 1979], this value is higher than pH responses of SiO_2 surfaces reported in many publications of *30-40 mV/pH* [Bousse et al., 1983]. These different responses are attributed to different oxide qualities and different densities of *Si-OH* surface groups on the different SiO_2 surfaces. The pH response of SiO_2 surfaces is caused by the protonation and deprotonation of the *Si-OH* surface groups present at the electrolyte/native oxide interface and can be calculated in the site binding model as discussed in chapter 1.1.

In figure 3.10 (b), the time averaged data from figure 3.10 (a) is shown together with the theoretical predictions of equation 1.16. The parameters used for the theoretical calculation are $pH_{pzc} = 2.2$ and $\beta = 0.15$, in good agreement with literature values [Bergveld and Sibbald, 1988].

The observed noise in the signal of the devices is typically $50 - 100\,\Omega$ in sheet resistance or $1 - 2mV$ in potential. Assuming this value as detection limit and taking

the response of $2.6\,k\Omega$ per pH step, a detection of pH variations of *0.02 - 0.04* units is possible with the device.

Adsorption of poly-l-lysine

To get an estimate of the sensitivity, the adsorption of charged polyelectrolytes provides an easy experimental system. As the SiO_2 surface is charged negatively at physiological pH, a positive molecule strongly adsorbs on the surface. Because of that, the adsorption of poly-l-lysine is often used for passivation and functionalization of SiO_2 surfaces.
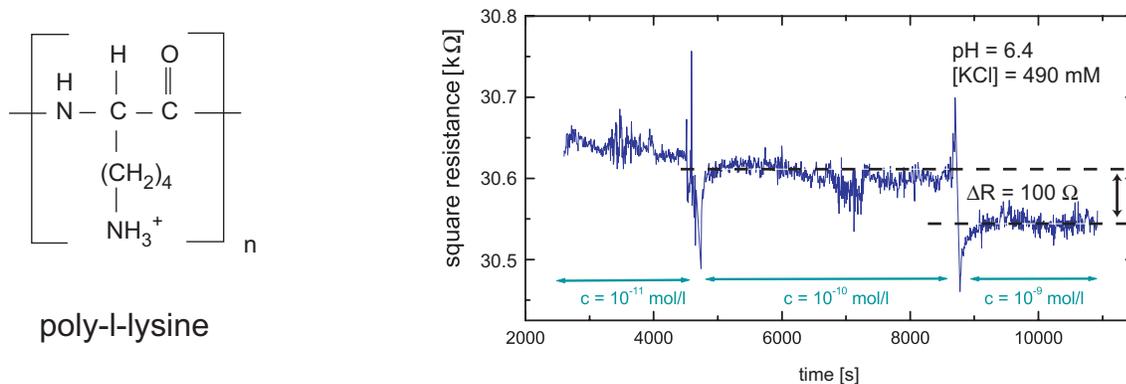
Figure 3.11: Change of square resistance for different poly-l-lysine concentrations in *490mM* KCl solution buffered with $10\,mM$ phosphate buffer. For $0.1\,nM$ no change was recorded, whereas for $1\,nM$, a clear decrease of the resistance was obtained. A linear drift of the device was subtracted, which could be caused by the diffusion of ions into the oxide layers.

Figure 3.11 shows the change of the resistance after exposure to electrolytes containing different poly-l-lysine concentrations. The measurements were done at *pH=6.4* and in the presence of *490 mM* KCl buffered with $10\,mM$ phosphate buffer on an undoped sensor device at a back gate voltage of $U_{bg} = +16V$. The molecular weight of the poly-l-lysine was *70.000 g/mol*, corresponding to approx. *600* lysine monomers per molecule. Injection of a solution of *0.1 nM* poly-l-lysine into the fluidic chamber was not detectable, whereas a solution of *1 nM* poly-l-lysine *(80 ng/ml)* resulted in a clear change of the conductance. Additional injection of buffer solution did not alter the measured conductivity, indicating the stability of the adsorbed poly-l-lysine layer. The calibration measurement can be used to relate the observed jump in resistance
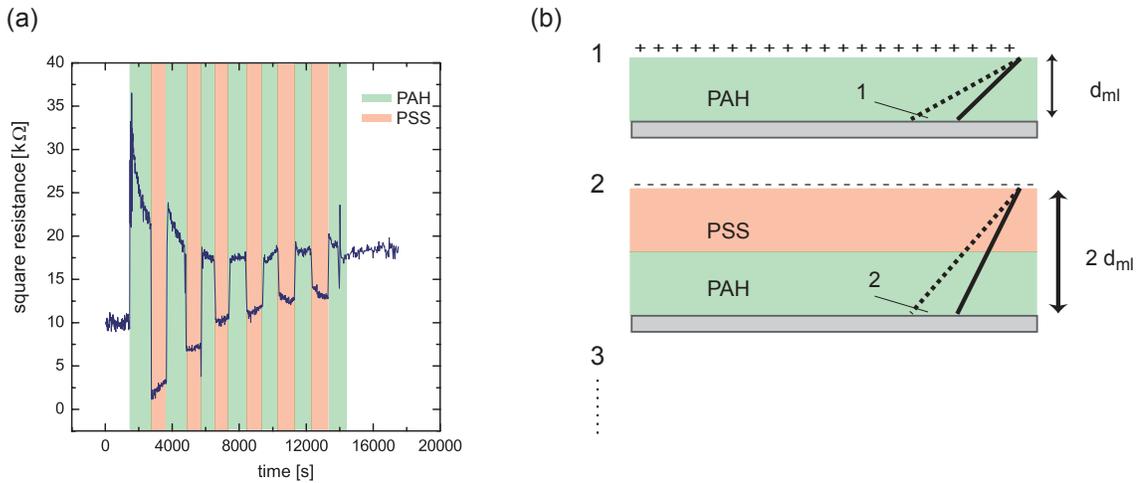
Figure 3.12: Typical resistance changes for the adsorption of PAH/PSS multilayers on a p-doped sensor device (born concentration $c = 10^{18} cm^{-3}$)(a). Times with PSS as last layer are shaded red, whereas green stands for PAH. After the last layer, the measurement chamber is rinsed with PBS buffer. The obtained response can be explained with the help of a simple model as depicted in (b).

of $\Delta R = 100\,\Omega$ to a change of the surface potential of $\Delta \psi = 2.2\,mV$. Using the *Grahame* equation, this computes to a charge density of around $0.025\,e^-/nm^2$, neglecting screening effects in the electrolyte solution and assuming that the charge sits directly at the native oxide surface. The typical signal to noise ratio would already allow the detection of resistance changes of $50\,\Omega/square$ or $0.01\,e^-/nm^2$. Using a rough estimate of an average diameter of *3-5 nm* for a typical biomolecule such as a protein, this would mean that the SOI-sensor device would be able to detect between *0.3* and *0.8* net charges per molecule in physiological solutions.

Adsorption of Polyelectrolyte Multilayers

Apart from the development of a sensor device for protein detection, a lot of other interesting questions might be answered by the application of a two dimensional electron system as sensor device. Among these, getting a better understanding of the mechanisms involved in the adsorption of polyelectrolyte multi layers is highly discussed question [Schoenhoff, 2003, Lavalle et al., 2004].

On the sensors with native oxide, multi layers composed of PAH and PSS were deposited by exchanging the buffers several times (see section 2.2.1.) and measuring

the change in sheet resistance. Figure 3.12 (a) shows a typical response of an p-doped
sensor at a back gate voltage of $U_{bg} = 0\,V$ when the polyelectrolytes are adsorbed.
Different colors indicate an exchange of buffer. Green represents PAH, red stands for
PSS. At the pH of our experiments of 7.5, PAH has a positive net charge, PSS is
negative. Together with the information from the calibration measurement, which had
a positive slope (higher potential at the front interface results in higher resistance),
the sign of the responses has the correct direction. For positive PAH, the resistance
increases, for negative PSS it decreases. After the measurement the chamber was
intensively rinsed with buffer and the obtained offset showed that the polyelectrolyte
multilayers were still present after the rinsing step.

To understand the signal a model of the polyelectrolyte layers can be developed
and compared to the measurement. In figure 3.12 (b), a sketch of the model is
showed. Every deposition of an additional layer can be modelled by a plate capacitor
with an increased plate distance of d_{ml} and a change of the surface charge of $\Delta\sigma$.
The layer itself is modelled as ideal dielectric, meaning that in this model, ions inside
the electrolyte layers are immobile, a question which is highly discussed in literature
[Schoenhoff, 2003].
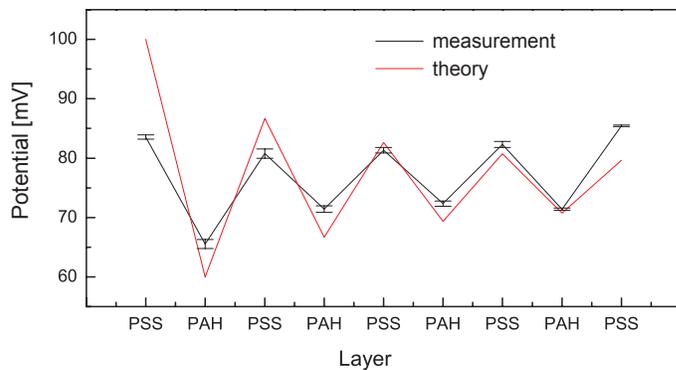
Figure 3.13: Comparison of the measured resistance changes when PAH/PSS multilayers are de-
            posited on the sensor surface (black) with the expected values from the theoretical
            model (red).

For the potential change at the surface of the semiconductor $\Delta\psi$, one obtains in
this model

$$\Delta\psi_n = \frac{\Delta\sigma}{\epsilon_0\epsilon_r}\frac{1}{n \cdot d} \qquad , \tag{3.3}$$

where n is the number of the monolayers deposited and d is the thickness of one

additional polyelectrolyte monolayer, taken to be $1.5\,nm$ [Decher, 1997].

Figure 3.13 shows the measured jumps in surface potential of another experiment done with an undoped sensor together with the prediction of the theory after equation 3.3. For the number of layers deposited, one gets reasonable agreement between measurement and model. However, in order to answer the question, whether or not the ions inside polyelectrolyte multilayers are immobile, additional experiments will be performed to verify that the signal really falls of as $1/d$.

Nevertheless, the adsorption experiments show that even after the deposition of 10 monolayer, corresponding to approx. $18\,nm$, the sensor is able to detect the charging of the outer layer. Similar experiments with poly-l-lysin and DNA can be used in future experiments for the immobilization of primary DNA and the detection of the hybridisation of the complementary strand.

3.3   Summary and Discussion

With the bare surface device a quantitative understanding of the semiconductor device was obtained and qualitative agreement with the simulated data could be achieved.

The performance of the sensor devices if exposed to electrolyte solutions was measured and the results for pH variations and variations of the salt concentration were measured. The experimental data agreed very well with the theoretical predictions for a surface charge density of $0.036\,C/m^2$ and a dissociation degree of the buffer ions of 20%. The sensitivity of the sensor device towards pH changes was determined to be $0.02 - 0.04\,pH$ -steps. From the adsorption experiments with poly-l-lysine, the sensitivity of the device towards surface charge changes was estimated to be $0.01\,e^-/nm^2$, making the further attempts to detect biological molecules reasonable. Experiments with the adsorption of polyelectrolyte multilayers composed from PAH/PSS showed that the charge reversal of the outer layer can be detected up to a thickness of approx. $18\,nm$. The experiments so far hint towards the fact that the ions inside the polyelectrolyte layers are immobilized.

However, in all measurements the signal drifted over long times. This might be caused by the instability of the native oxide surface or the diffusion of ions into the sensor material. Both effects can be reduced, if the surface is passivated with an additional layer covering the native oxide. In the next section, experimental results of the surface passivation with organic PMMA and ODTMS layers will be presented.

4 Results II - Surface Funtionalization

As described in chapter 2, SOI is covered by a thin layer of SiO_2, the native oxide. This native oxide is not electrochemically stable over long times for extreme pH conditions and surface groups being sensitive to changes of pH are dissociated (see chapter 3). A lot of different anorganic materials have therefore been used to passivate the surface of silicon based *ISFET* devices [Bergveld and Sibbald, 1988], for example thermally grown silicon oxides or silicon nitride films. Even though these layers improve the stability and performance of the native oxide, for a biological application organic passivation layers are preferable. They combine the requirements of a surface passivation and biocompatibility. In principle, a passivation layer can be adsorbed to the surface or covalently bound to it. During this thesis, various materials and methods have been tested, because many standard technologies and methods known from the functionalization of pure glass slides resulted in the destruction of the composite material system represented by the final encapsulated sensor devices.

Two methods, the adsorption of a thin film of Poly-Methyl-MethAcrylate (PMMA) by spin coating and the covalent binding of OctadecylTriMethoxySilane (ODTMS) resulted in satisfying passivation and hydrophobization of the sensor surface and the results will be discussed in this chapter.

4.1 Hydrophobization with PMMA

For the deposition of a thin PMMA layer, a sensor chip was cleaned after the metallization step according to the procedure described in chapter 2.2.2. A thin layer of PMMA was deposited by a spin coating technique on the cleaned wafer (see section 2.2.2.) and the resulting thickness of the PMMA layer was measured by ellipsometry. For the measurement of the ellipsometric thickness of the PMMA layer, silicon substrates with chemically identical surface were treated in parallel with the sensor

(a)   (b)
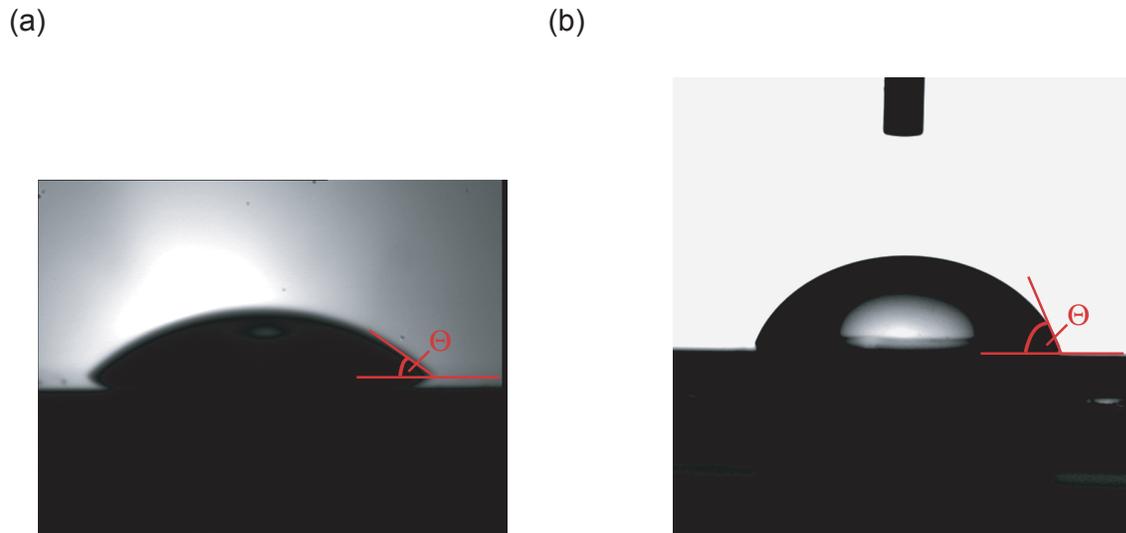
Figure 4.1: Crossection of a water droplet on a sensor device before (a) and after (b) the deposition of the PMMA layer. The contact angle changed from $< 10^o$ on the hydrophilic SiO_2 to $\approx 60^o$ on the PMMA covered surface.

devices. The measurement of the ellipsometric thickness on the multilayer SOI substrates was not possible due to multiple reflections at the various interfaces. As the thickness of the resulting PMMA layer is determined by the surface conditions, the concentration of PMMA in solution and the spinning rate and not by the underlying layer structure of the substrate, the measured thickness on the sample silicon wafers will be the same than the thickness on the sensor devices. A PMMA/toluene solution with $1\,mg/ml$ spun at an average speed of *1000 rpm* for $60\,s$ resulted in a layer with a thickness of $(20 \pm 3)\,nm$, indicating a thick mutlilayer.

In addition to the thickness, the contact angle of a water drop on the PMMA covered surface was measured. The contact angle changed from $< 10^o$ on the hydrophilic and freshly cleaned SiO_2 surfaces to $> 65^o$ on the PMMA covered surface. Figure 4.1 shows the digitized images of water droplets on the surface before (a) and after (b) the PMMA deposition. The increase in contact angle can be explained by the hydrophobic character of the PMMA in comparison with the completely hydrophilic SiO_2 surface.

In addition to the measured thickness and the change in contact angle, a direct test of the PMMA passivation can be performed on the sensor surface. If the surface

(a)

(b)
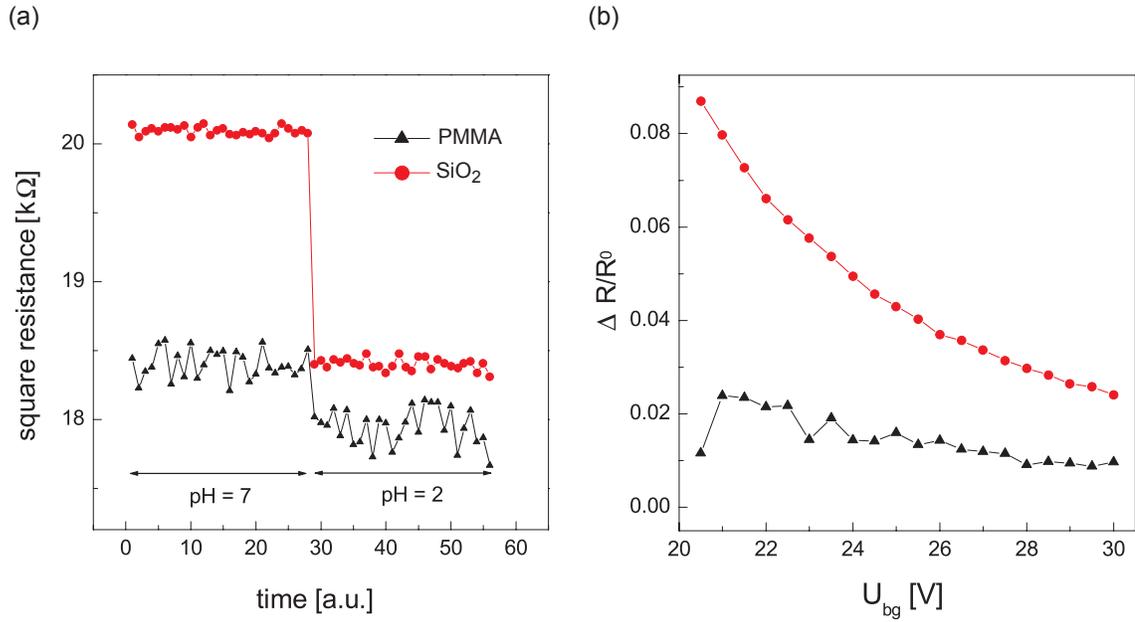
Figure 4.2: Measured response of a device to a pH step from $pH = 7$ to $pH = 2$ of the electrolyte before and after the deposition of a PMMA passivation layer. In (a), the response is shown for an applied back gate voltage of $U_{bg} = +21\,V$. (b) shows the relative change in sheet resistance for various back gate voltages.

is covered with a thick passivation layer, being impermeable to H^+ ions, the response towards pH changes will disappear as the surface hydroxyl groups are no longer accessible to the electrolyte. Figure 4.2 shows the measured response (change in resistance) for a sensor device with PMMA coating (black triangles) and without coating (red dots). On the left the time resolved response for both surfaces is shown at an applied back gate voltage of $U_{bg} = +21V$. For the bare SiO_2 surface, the resistance drops instantaneously when the pH is changed from $pH = 7$ to $pH = 2$ in agreement with the measurements in chapter 3.2.2. Obviously, for the PMMA covered surface, the response is greatly reduced. The seemingly higher noise level is due to the fact, that the sensor was connected a second time after the PMMA deposition step and that the electrical contacts were worse. In part (b) of figure 4.2, the relative change in resistance upon the pH change from $pH = 7$ to $pH = 2$ is shown for applied back gate voltages between $U_{bg} = +21V$ and $U_{bg} = +30V$. The relative change in resistance decreases from ≈ 0.09 to ≈ 0.03 for the bare surface device and almost stays constant at $\approx 0.01 - 0.02$ for the PMMA coated device. For the PMMA

covered surface, the response is greatly reduced.

In addition, the response for the native oxide covered device decreases for increasing back gate voltage, in good agreement with the sensitivity considerations in chapter 3.

4.2   Hydrophobization with ODTMS

Although the deposition of PMMA by the spin coating technique worked nicely, it had two major drawbacks with respect to the later deposition of a lipid monolayer as functional coating. First, the layer of hydrophobic material was only adsorbed to the hydrophilic SiO_2 surface. If water got between the PMMA layer and the SiO_2 surface (for example, when the layer was damaged at some point during the later binding of encapsulation process), the complete layer was lifted off and the surface was hydrophilic again. The second drawback was the only partial apolarity of the PMMA, which results in a smaller degree of hydrophobicity of the surface.

Both of these drawbacks could be overcome by the covalent binding of a silane molecule to the SiO_2 surface. OctadecylTriMethoxySilane (ODTMS) turned out to be the best working material for the surface hydrophobization. All sensors for the later deposition of a functional lipid monolayer were functionalized with ODTMS after the procedure described in section 2.2.2. Again, the layer quality and presence was verified with ellipsometry and contact angle measurements. Figure 4.3 shows the digitized images of water droplets on the surface before and after the binding of ODTMS. The contact angle changed from $< 10^{\circ}$ on the hydrophilic SiO_2 surface to $\approx 90^{\circ}$ on the ODTMS functionalized surface. This increase in contact angle can be explained by the hydrophobic character of the ODTMS alkyl chains in comparison with the completely hydrophilic SiO_2 surface.

The thickness of the ODTMS layers was determined to be $(2.0 \pm 0.3)\, nm$, indicating a monolayer. For the measurement of the ellipsometric thickness of the ODTMS layer, silicon substrates with chemically identical surfaces were treated in parallel with the sensor devices. The measurement of the ellipsometric thickness on the multilayer SOI substrates was not possible due to multiple reflections at the various interfaces. As the thickness of the resulting ODTMS layer is determined by the surface conditions and the reaction parameters during the deposition and not by the underlying layer structure of the substrate, the measured thickness on the sample silicon wafers will

(a)   (b)
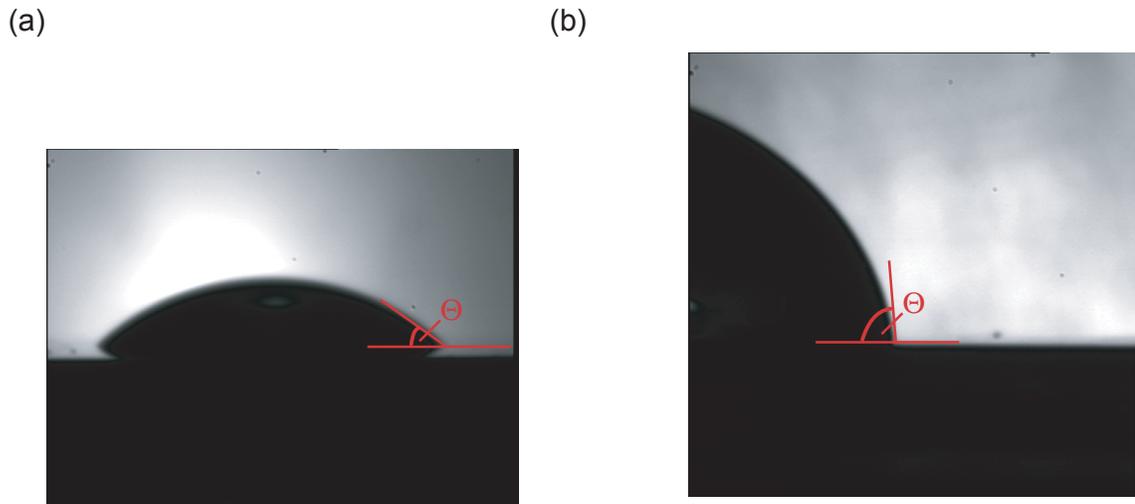
Figure 4.3: Crossection of a water droplet on a sensor device before (a) and after (a) the deposition of the ODTMS layer.

be the same than the thickness on the sensor devices.

All experiments to see a reduced pH response on the ODTMS covered devices did not work. Rather, the response of the device towards changes of the electrolyte pH remained almost unchanged before and after the ODTMS deposition. This can be explained by he fact, that the monolayer of ODTMS layer is not perfectly impermeable to H^+ ions and that only part of the Si-OH surface groups are occupied by silane molecules. Consequently, a change of pH in the electrolyte solution on top of the ODTMS still influences remaining surfaces groups and leads to a change of the sheet resistance.

4.3   Summary and Discussion

The experiments to functionalize the surface with an adsorbed layer of PMMA showed that the surface is rendered hydrophobic after the adsorption and that the pH response of the sensors is drastically reduced. However, the stability of these layers was not sufficient and the layers were lost, once water got between the PMMA and the sensor surface.

A covalent binding of ODTMS to the sensor surface worked fine, the contact angle changed from from $< 10^{o}$ on the hydrophilic SiO_2 surface to $\approx 90^{o}$ on the ODTMS functionalized surface. The ellipsometric thickness of the ODTMS layers was determined to be $(2.0 \pm 0.3)\,nm$, indicating a monolayer. However, the sensor devices did not show a reduced pH response, probably due to the fact that hydrogen ions can still penetrate the thin ODTMS layer. Nevertheless, because of the high degree of hydrophobicity and the high stability of the covalent bond, this passivation technique can be used for the immobilization of lipid monolayers in the experiments described in the next section.

5 Results III - Lipid Membrane Based Charge Sensor
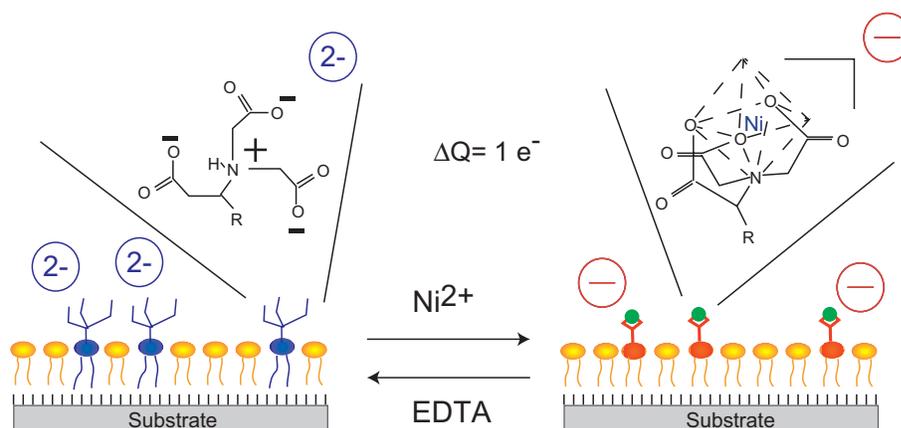
Figure 5.1: Sketch of the lipid membrane used to measure the charging and decharging of the NTA headgroups with the semiconductor sensor. Upon injection of EDTA containing buffer, the nickel ions were solved out of the NTA headgroups. To account for the different composition of the buffers, both buffers were equilibrated on lipid systems with no NTA headgroups.

The interaction of proteins with the lipid membrane is one of the most important regulation mechanisms in cell biology and its understanding is therefore crucial for many biological processes. This interaction can be mimicked by the interaction of proteins with solid supported lipid membranes. These membranes are a very flexible and robust system to measure specific reactions on surfaces. In this thesis, a lipid layer consisting of DMPC, cholesterol and DOGS-NTA was chosen as model system (see section 2.2.3.). The surface of the sensor device was functionalized with a lipid bilayer for the hydrophilic SiO_2 surface and a lipid monolayer for the hydrophobic, ODTMS covered surfaces.

In both cases, mono- and bilayer systems, the outer leaflet of the lipid layer facing the solution is the same. Figure 5.1 shows a schematic of a monolayer composed of DMPC and DOGS lipids with functional NTA headgroups. These can be charged

with divalent nickel ions and decharged by adding a competitor like EDTA to the
solution, resulting in a net change in charge during this reaction of $1\,e^-$ per DOGS-
NTA headgroup [Schmitt et al., 1994, Sackmann, 1996]. As this process is reversible,
a switch of the semiconductor conductivity upon buffer exchange can serve as a proof
of the presence of functional NTA binding sites. In order to account for the different
bulk properties of the buffer systems, the nickel containing buffer was equilibrated to
the EDTA buffer by adding KCl on a lipid membrane covered sensor containing no
NTA headgroups (see section 5.1).

5.1 Lipid Bilayer on Bare SiO_2

Supported lipid bilayers mimic the native cell membrane with the incorporated transmebrane proteins. Therefore, in a first approach a functional lipid bilayer was deposited on top of the native oxide by vesicle fusion as described in chapter 2.2.3.
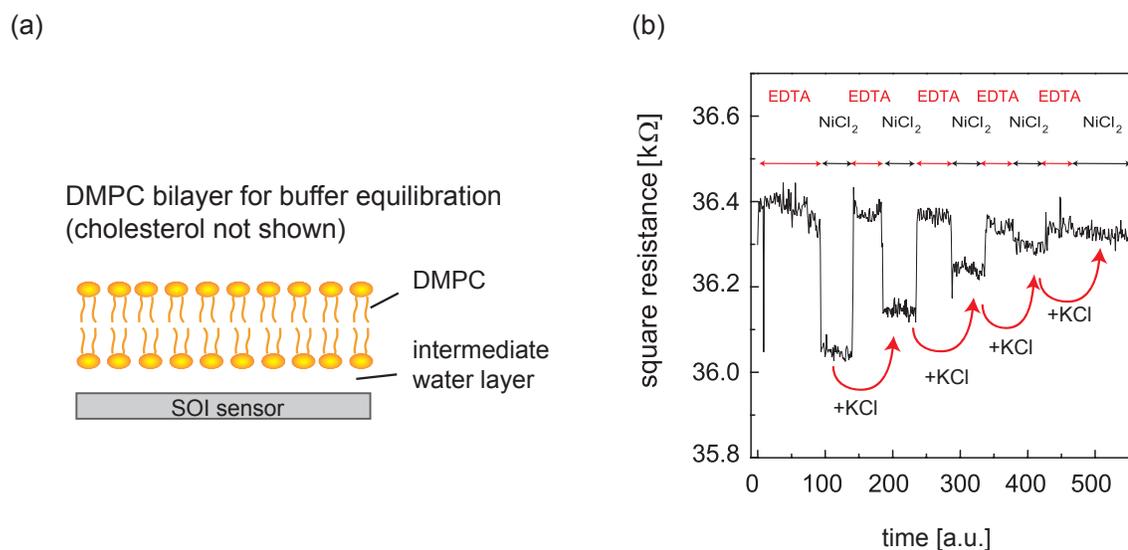
Figure 5.2: Sketch of a bilayer on top of the hydrophilic substrate used for the equilibration of the buffers, containing no functional DOGS-NTA lipids (a). The cholesterol molecules used to keep the bilayers in the fluid phase are not shown. For the equilibration, KCl was added to the nickel buffer until the difference between the two buffer systems was minimized (b).

Before the specific binding of Ni to the NTA headgroups can be detected, the two buffers were adjusted to yield the same resistance value on a lipid bilayer composed of 65% DMPC and 35% cholesterol as shown in figure 5.2 (a). As this system is identical to the charge sensor membrane except for the functional DOGS-NTA lipids, all bulk and other buffer effects are taken into account by this reference method. After each buffer exchange, $1ml$ of a $1M\ KCl$ solution was added to the $NiCl_2$ buffer, until the resistance change upon buffer exchange disappeared in the noise level of the measurement, as shown in figure 5.2 (b).

Once this equilibration was done, the chamber was rinsed extensively with ethanol to remove the DMPC bilayer and a bilayer containing DOGS-NTA lipids was deposited on the surface by vesicle fusion as described in section 2.2.3. Figure 5.3 (b)
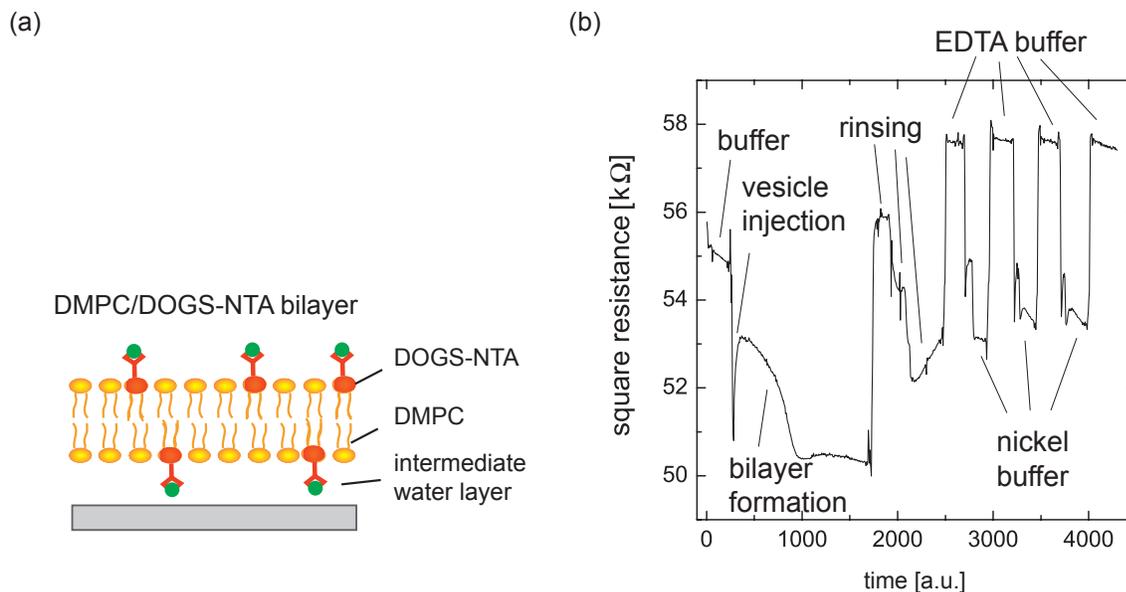
Figure 5.3: Sketch of the lipid bilayer used for the charging and decharging experiments (a). Complete measurement of the time dependant sheet resistance for the formation of a lipid bilayer and a charging and decharging experiment (b). For the charging experiments, 20% functional lipids were incorporated.

shows the complete measurement for a DOGS-NTA concentration of 20%. As depicted in the figure, the resistance drops upon injection of the vesicle solution. The bump in the signal is attributed to the formation of the bilayer and the adsorption of vesicles to it. After the signal stabilized, the chamber was flushed with standard buffer several times and the remaining nickel ions were removed by EDTA buffer. After that, the reversible charging and decharging of the NTA headgroups was measured.

The resistance changes were converted to changes in the potential by calibration measurements, which were done prior to the experiments. For the resistance values of interest (in this case between 50 and $60\,k\Omega$ /square), a relation between resistance and potential of $-46\,k\Omega$/Volt was obtained. Consequently, all measurements can be analyzed in terms of potential changes as shown in figure 5.4. In part (a), the obtained change in potential is shown versus time, whereas part (b) shows the time averaged signals. The red curve corresponds to the 2 point resistance, the black curve corresponds to the 4 point resistance. An exchange of buffer and hence a binding of Ni resulted in a change of the potential of $\Delta\psi = (13.8 \pm 1.3)\,mV$.

To further interpret this result, an easy plate capacitor model can be used as
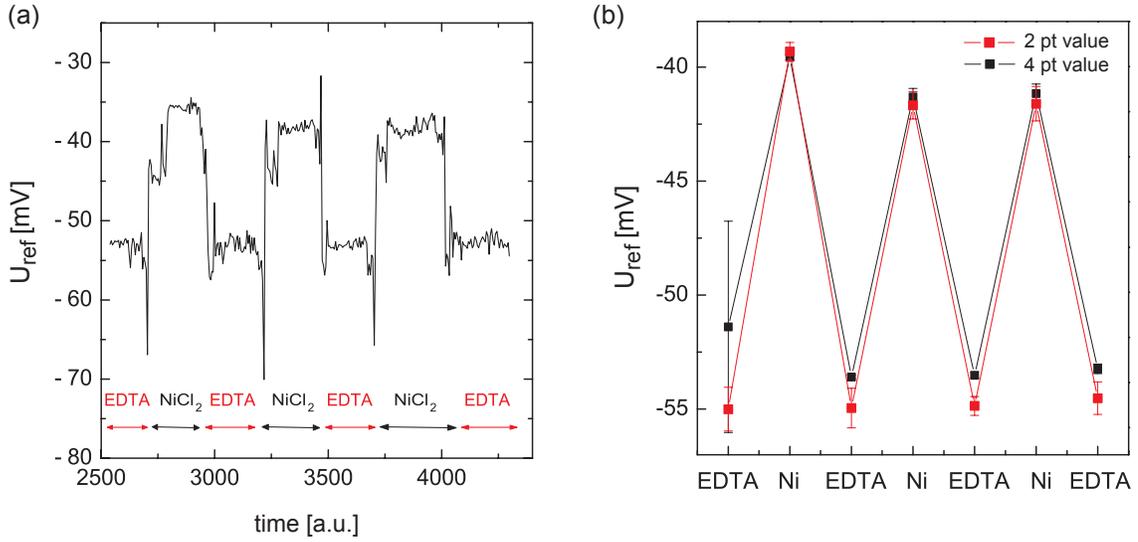
Figure 5.4: Potential change for the charging and decharging of the NTA headgroups. (a) shows the response versus time, (b) shows the time averaged potential values for the two (red) and the four point (black) measurement.

schematically shown in figure 5.5. In this model, the lipid bilayer is approximated as a dielectric layer, separated from the substrate through an intermediate water layer. The intermediate water layer is present, because both surfaces (lipid headgroup and SiO_2) are hydrophilic. A change of the surface charge at the outer leaflet of the membrane of $\Delta\sigma$ is related to a potential change at the inner leaflet (assuming a linear potential drop over the alkyl chains as for a ideal dielectric)

$$\Delta\psi_2 = \frac{\Delta\sigma}{\epsilon_0\epsilon_r}d_{bl} \qquad . \tag{5.1}$$

For the conditions of our experiment, the distance between the bilayer and the substrate is known to be roughly $d_{water} = 2\,nm$, whereas the screening length due to the presence of mobile ions in the water layer is $1/\kappa \approx 0.4\,nm$. Therefore, it is reasonable to include screening effects into the model and as a first approximation, it can be assumed that the potential in the electrolyte follows the *Debye Hückel* approximation

$$\Delta\psi(x) = \Delta\psi_2 e^{-\kappa x} \qquad , \tag{5.2}$$

where $1/\kappa$ is the *Debye* screening length. In total, a charge density change at the
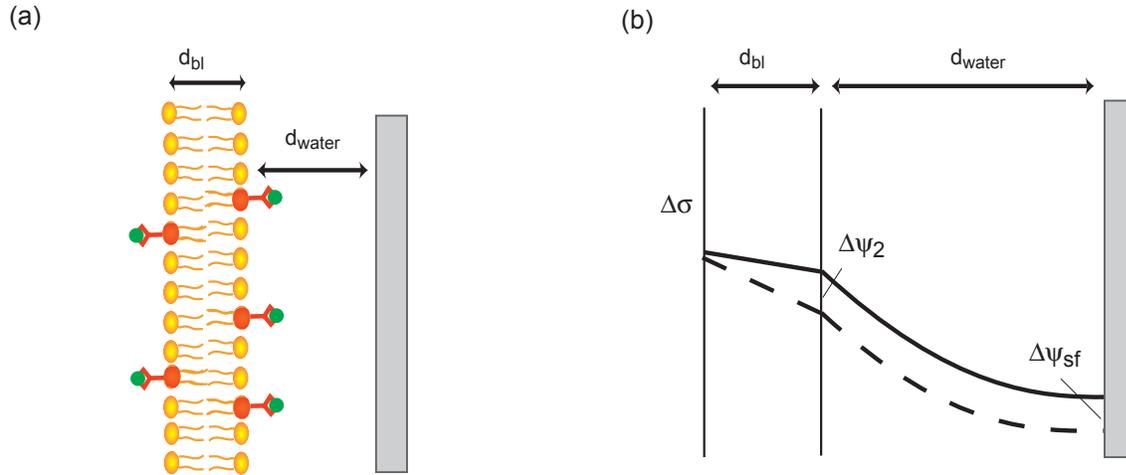
Figure 5.5: Sketch of the plate capacitor model used to interpret the data. The bilayer is approximated as ideal dielectric and in the water layer between bilayer and substrate, the *Debye Hückel* approximation is used.

outer leaflet results in a potential shift at the surface of the substrate of

$$\Delta\psi_{sf} = \frac{\Delta\sigma}{\epsilon_0\epsilon_r}d_{bl}\,e^{-\kappa\,d_{water}} \qquad . \tag{5.3}$$

If one assumes that all charges sit at the outer leaflet and that the area per lipid is $\approx 65\mathring{A}^2$ [Cevc, G., 1993], the change of the surface charge density is given by

$$\Delta\sigma = \frac{1e^-}{65\mathring{A}^2}\left[\frac{\%DOGS - NTA}{100}\right] \qquad , \tag{5.4}$$

and one arrives for $\%DOGS - NTA = 20$ at $\Delta\sigma = \frac{1e^-}{325\mathring{A}^2}$. Inserting the known values for our experiments of $d_{bl} \approx 3\,nm$, $\epsilon_r = 2.2$ [Dilger et al., 1979], $1/\kappa = 0.4\,nm$, $d_{water} \approx 2\,nm$, the expected change of potential in this model is $\Delta\psi \approx 51\,mV$.

This value is higher than the measured value, indicating that the simple model used is not able to account for the details of the measurement. Obviously, there are two reasons for that. First, the assumption that the charges directly sit on the plate represented by the lipid layer is not correct. They rather sit in the headgroup region of the NTA chelator lipid, which is accessible to water [Dorn et al., 1998] and they will therefore be screened already at the outside of the assumed plate capacitor, drastically reducing the measured signal compared to the model. Moreover, for the composite material used it is not surprising that a bilayer will not be perfect but have some holes,

also reducing the overall measured signal. The effect of the screening of the charges in the headgroup region will be discussed in the next section for monolayer systems, as the defined geometry there allows a quantification of the effect. Additionally one has to take into account that functional NTA lipids will also be incorporated in the lower leaflet, making the analysis even more cumbersome.

Summarizing, the bilayer experiments were successful to detect the molecular charging in a lipid bilayer with the SOI sensor device, proofing its suitability to detect more complex interactions, such as the binding of proteins to the lipid layer. However, experiments to detect this protein binding to the complexed NTA groups were not successful in high ionic strength buffers and the distribution of the NTA groups over the lipid bilayer is unknown.

Therefore, to have a well defined geometry and density of the linker molecules and get rid of the intermediate water layer, experiments with a monolayer system on a hyrophobic substrate were performed and will be presented in the next section.

5.2   Lipid Monolayer on Hydrophobic Surfaces

Instead of using vesicle fusion, the lipid monolayers were prepared by the solvent exchange method on the ODTMS covered sensor devices (see section 2.2.3.). Similar to the bilayer system, the headgroups of the DOGS-NTA lipids will switch their charge upon the exchange of the buffer by $1e^-$/DOGS-NTA headgroup. Again, the buffers were equilibrated on monolayers with no functional lipids by adding KCl to the nickel buffer. After each experiment, the chamber was flushed with ethanol and rinsed intensively with buffer to remove the excess lipids. Different concentrations of functional lipids were used and the response depended linearly on the concentration of DOGS-NTA lipids incorporated into the lipid layer.
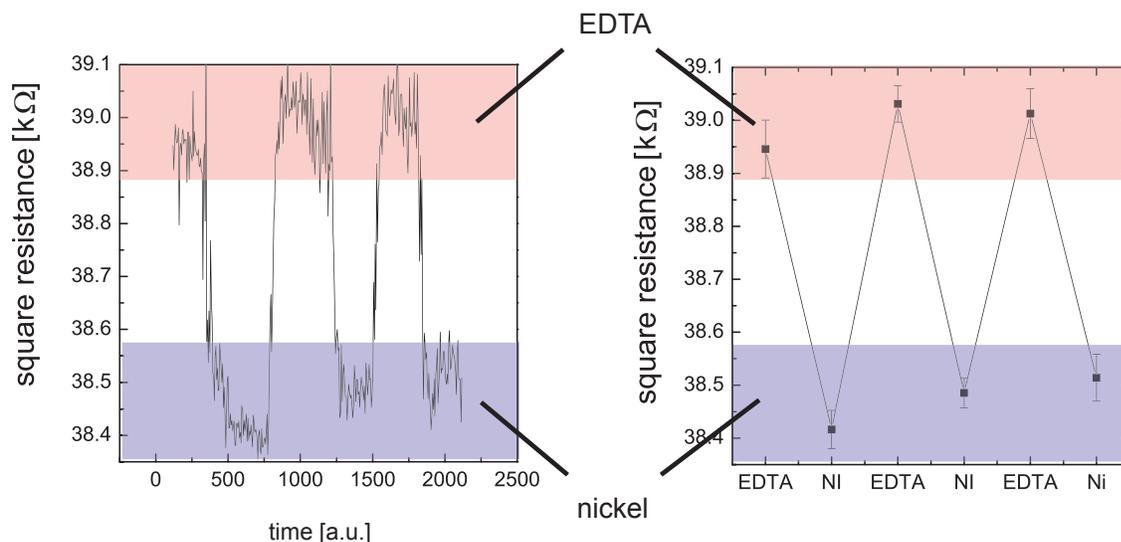
Figure 5.6: Typical signal for a charging and discharging experiment with DOGS-NTA functional lipids. (a) shows the time resolved data for a DOGS-NTA concentration of 5%. The slight drift of the levels is typical for all measurements and can be attributed to either unspecific adsorption of ions at the surface or drift of ions into the respective oxides of the sensor. (b) shows the time averaged jumps in resistance upon buffer exchange.

Figure 5.6 shows a typical response curve for a DOGS-NTA concentration of 5%. The left part shows the original time resolved resistance signal, the right part shows the time averaged potential changes. Again, a calibration measurement was used to relate changes in resistance to potential changes. A change of the electrolyte buffer resulted in an instantaneously resistance change of the SOI layer of $\Delta R \approx (0.55 \pm 0.05)\, k\Omega$/square or $\Delta \psi \approx (6.3 \pm 0.5)\, mV$. The same measurement was performed for
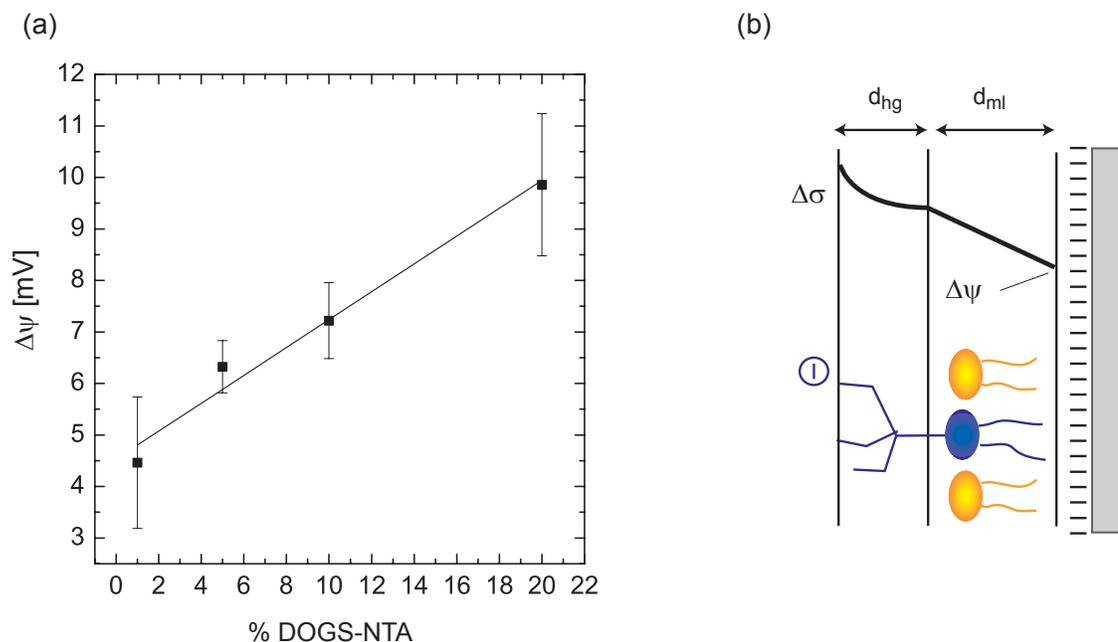
Figure 5.7: Measured changes in potential for different concentrations of DOGS-NTA lipids. The solid line corresponds to a linear fit to the data, indicating a linear dependance of the signal from the concentration of functional lipids (a). Sketch of the simple plate capacitor model used to interpret the measured data. The lipid layer is modelled as ideal dielectric (b).

DOGS-NTA concentrations between 1% and 20% and the resulting change in potential for the buffer exchange was measured. Figure 5.7 (a) shows the measured changes in potential $\Delta\psi$ for the lipid monolayer charge sensor for concentrations between 1% and 20%, averaged over many experiments. A linear fit to the data shows that the measurements correspond to an increase of the signal of $\Delta\psi \approx 0.3\,mV$ for an increase of the DOGS-NTA concentration of 1%.

In order to understand that result, a model as shown in figure 5.7 (b) can be used. As discussed in the previous section, for a monolayer on a hydrophobic substrate no intermediate water layer exists between the substrate and the lipids, but in the head-group region, screening effects will take place, because the NTA groups are hydrated [Dorn et al., 1998]. Therefore the theoretical model for the interpretation of the data is modified. The lipid monolayer is treated as an ideal dielectric material, having a dielectric constant of $\epsilon_r = 2.2$ and a thickness of $d_{ml} = 1.5\,nm$ [Dilger et al., 1979]. Additionally, in the head group region, the *Debye Hückel* approximation is assumed

to be valid. Consequently, in the head group region the potential is given by

$$\psi(x) = \psi_o e^{-\kappa x} \qquad , \qquad (5.5)$$

where $1/\kappa$ is the *Debye* screening length and ψ_o is the potential at the position of the nickel ions. Within the *Debye Hückel* approximation, a change of the surface charge is related to a change of the potential as $\Delta\sigma = \epsilon_o \epsilon_r \kappa \Delta\psi_o$ and thus the charging of the head groups a distance d_{hg} away from the alkyl chains of the lipids causes a potential change of

$$\Delta\psi = \frac{\Delta\sigma}{\epsilon_o \epsilon_r} \frac{1}{\kappa} e^{-\kappa d_{hg}} \qquad . \qquad (5.6)$$

In the alkyl chains, the potential is given by

$$\psi(x) = \tilde{\psi}_o - \frac{\Delta\sigma}{\epsilon_o \epsilon_r} x, \qquad (5.7)$$

where $\tilde{\psi}_o$ is the potential at the interface to the electrolyte. Again, a change in $\tilde{\psi}_o$ is related to a change in σ as $\Delta\sigma = \epsilon_o \epsilon_r \kappa \Delta\tilde{\psi}_o$, so that one arrives at

$$\Delta\psi(x) = \Delta\tilde{\psi}_o(1 - \kappa x) \qquad . \qquad (5.8)$$

Combining equation 5.9 and 5.8, one arrives at a prediction for the measured potential

$$\Delta\psi = \frac{\Delta\sigma}{\epsilon_o \epsilon_r} \frac{1}{\kappa} e^{-\kappa d_{hg}} \frac{1}{1 - \kappa d_{ml}} \qquad . \qquad (5.9)$$

The surface charge density change for a buffer exchange $\Delta\sigma$ is related to the density of functional DOGS-NTA lipids as

$$\Delta\sigma = \frac{1e^-}{65\text{Å}^2} \left[\frac{\%DOGS - NTA}{100} \right] \qquad , \qquad (5.10)$$

so that one arrives at

$$\Delta\psi = \frac{1e^-}{65\text{Å}^2} \frac{1/\kappa}{\epsilon_r \epsilon_0} \frac{\%DOGS - NTA}{100} e^{-\kappa d_{hg}} \frac{1}{1 - \kappa d_{ml}} \qquad . \qquad (5.11)$$

From the measured data, the effective measured distance of the charges from the alkyl chains d_{hg} can be determined. Inserting the values of our experiment of $1/\kappa \approx 0.4\,nm$, $\epsilon_r = 2.2$, $d_{ml} = 1.5\,nm$ and $\Delta\psi \approx 0.3\,mV$ for a concentration increase of 1% DOGS-NTA, one gets $d_{hg} \approx 1.6\,nm$, which is in the same order of magnitude as the value one would expect from an estimation of the molecular structure of the NTA

head group. The chelate complex is connected to the lipids over 12 atoms. Taking a bond length of C-C bond of $\approx 0.15\,nm$ one arrives at a distance of $1.8\,nm$. With respect to the fact that the exact charge distribution in the NTA head groups and the ion concentration near the surface are only approximately known, the measured data can very well be explained within the plate capacitor model. However, by using this model one has to be careful, as it makes several approximations. For example, one neglects the Stern layer at the interfaces and hence the atomic structure of the ions in the electrolyte. To get a deeper understanding of the measured signals, further theoretical work is necessary.

The sensitivity of the senor in the measurements can be calculated from the obtained signal for a DOGS-NTA concentration of 1%. Assuming a perfect layer, the molecular charge sensor had a realized sensitivity of $1e^-/65\,nm^2$. As the signal depends linearly from the concentration of functional lipids, one can extrapolate the signal height to lower concentrations. The noise in the measurement would allow to detect signals being a factor of 10 smaller, resulting in a maximum sensitivity of the charge sensor of $1e^-/650\,nm^2$.

Summarizing, the monolayer charge sensor experiments confirmed that the developed sensor is suitable to detect the charging and decharging of the lipid headgroups and that the specific binding of proteins should be detectable. In a next step, the Ni loaded DOGS-NTA lipids can be used as specific binding site for His-tagged proteins. The results of these experiments will be discussed in the next chapter.

5.3   Summary and Discussion

The experiments with a functional lipid bilayer on the hydrophilic substrates showed that in principle the detection of charged molecules on biofunctional sensor devices is possible. For high (20%) concentrations of functional lipids, stable signals were obtained. The interpretation of the obtained signals is difficult due to the fact that the distribution of the functional lipids over the upper and lower leaflet is unknown and an intermediate water layer between lipid layer and substrate is unavoidable. Moreover, the screening of the charge in the headgroup region has to be taken into account. Additionally, the detection of a His-tagged proteins was not possible in the bilayer system for high ionic strength buffer.

A lipid monolayer on a hydrophobic substrate gave reasonable responses even for functional lipid concentrations of 1%. The response for different concentrations scales linearly with the concentration of functional lipids in the layer. The achieved sensitivity for this biofunctional system was $1e^-/65nm^2$, but the signal to noise ratio would allow the measurement of signals, which are a factor of 10 smaller. Because of the linear relation between potential change and functional lipid concentration, this translates to a maximum sensitivity of $1e^-/650nm^2$. In an optimized measurement setup with an effective shielding so that lower back gate voltages can be used as working point (see section 3.1.3.), this value can be further optimized.

To compare this sensitivity with other techniques, one can look at the obtained sensitivity of SPR or impedance spectroscopy as reported in the literature. Hillebrand et al. estimate the maximum sensitivity for the detection of the charging of the DOGS-NTA lipids on ITO substrates to be $1e^-/100nm^2$ and demonstrate the measurement of $1e^-/40nm^2$. However, they did not succeed to detect the further binding of a histidine tagged protein to the complexed chelator lipids [Hillebrandt et al., 2002].

For chelator lipid monolayers on gold surfaces, Dorn et al. observed the binding of Ni ions to the chelator lipids by SPR [Dorn et al., 1998]. For a molar concentration of the functional lipids of 1%, they obtained a signal of 50 resonance units (RU) at a noise level of ≈ 5 RU. Taking $65\mathring{A}^2$ per lipid molecule in a fluid lipid monolayer, this measurements can be extrapolated to a maximum sensitivity of $\approx 1e^-/650nm^2$, equal to the sensitivity obtained in our setup.

6 Results IV - Specific Protein Binding
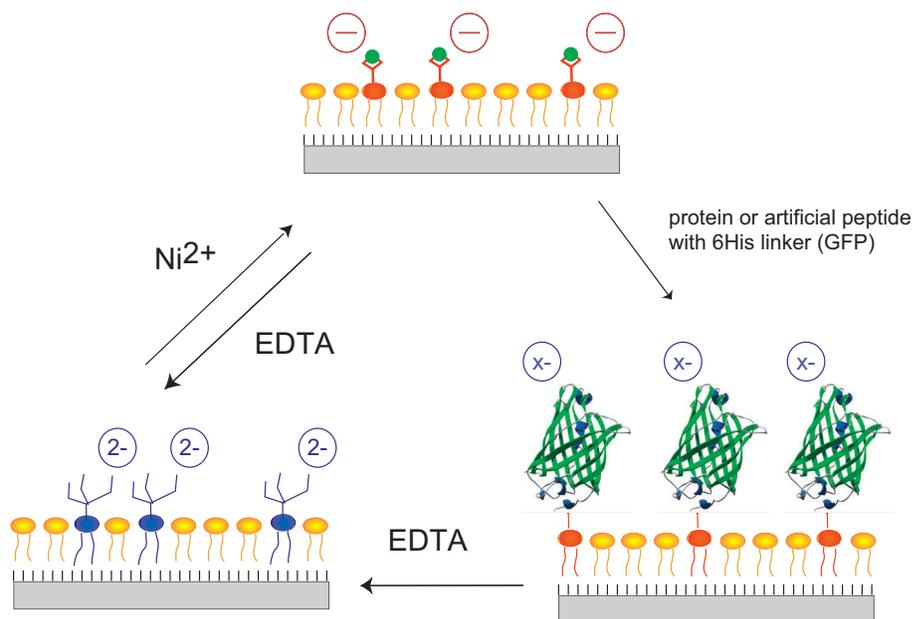
Figure 6.1: Sketch of the biomimetic model surface system used to test the semiconductor sensor. The DOGS-NTA headgroups can be charged and decharged by nickel and EDTA. In the complexed state, the chelator lipids serve as specific binding sites for histidine tagged artificial peptides or proteins (In this case GFP is shown).

As discussed in the last section, the SOI sensor was able to detect the charging and decharging of the NTA chelator lipids with very high sensitivity, hence proofing its suitability for further biological detection measurements. One reason to use the DOGS-NTA functional lipid monolayer as test system was that one can directly use them in the charged state to specifically bind proteins or artificial peptides, which have 6 additional histidine amino acids added to their primary structure, a so called His-tag.

Figure 6.1 shows the principle cycle for the surface reaction. The NTA headgroups can be charged and decharged by nickel and EDTA as discussed and measured in the

last section. In addition, the nickel loaded head group also serves as a specific binding site for the His-tagged proteins. As only the complexed state is binding His-tags, this binding can be undone again by adding EDTA, opening the possibility to run the full cycle several times and reusing the lipid interface.

Experiments with pure His-tags, artificial aspartic acid peptides with His-tags, His-tagged Green Fluorescent Protein (GFP) and His-tagged LumazinSynthase (LuSy) will be presented and discussed. Figure 6.2 shows schematics of the four different types of molecule used in the binding experiments in this chapter.
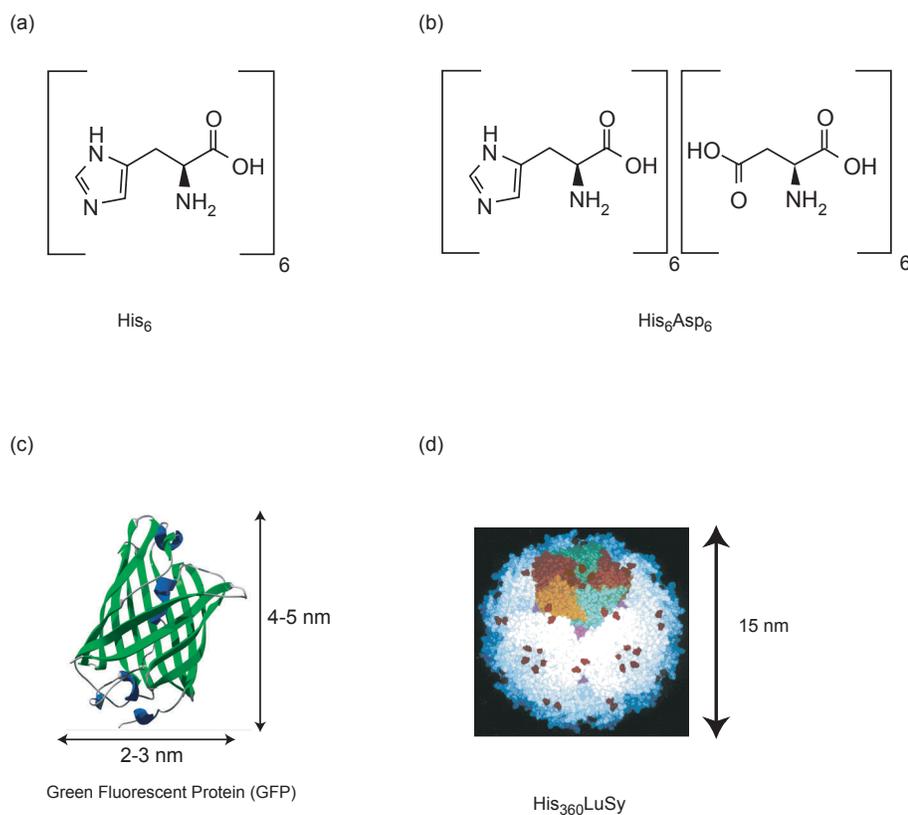
Figure 6.2: For the binding experiments, four different molecules were used. (a) and (b) show sketches of the artificial peptides His6 and His6Asp6. (c) and (d) show the natural proteins GFP and His360LuSy. Except for the His6, all other molecules have an excess of negatively charged amino acids at $pH = 7.5$ and hence the binding should result in an increase of the resistance of the undoped sensor devices.

The binding experiment were done in the same way for all His-tagged peptides and proteins and will be presented in the next sections.

6.1 Specific Detection of Artificial Peptides

In the loaded state, the NTA headgroups of the DOGS lipids represent a specific binding site for His-tags, a sequence of 6 histidine amino acids. In principle, already two histidne amino acids can bind to the chelate complex, but for six histidines the bond formation is optimized. As they consist of natural amino acids, these His-tags can be added to the primary sequence of any natural protein or artificial peptide. The bond of a His-tag to a metal chelate complex is a standard method used in molecular biology and is a very flexible linker system for many different molecules.

6.1.1. Binding of His-tags

To make sure that possible signals in protein binding experiments are really caused by the charge of the protein and not by the His-tags themselves, the binding of the His-tags without attached peptide was measured. Figure 6.3 (a) shows the molecular structure of histidine, figure 6.3 (b) shows the measured change in the sheet resistance for the binding experiment. The measurement was done on a ODTMS covered undoped sensor at a back gate voltage of $U_{bg} = +25V$. The concentration of the functional DOGS-NTA lipids was 5% and the presence of the functional mono layer was verified by the reversible charging and decharging of the head groups with nickel and EDTA containing buffer. The two buffers were equilibrated before the experiment as described in the previous section. The histidine containing buffer was not matched with the other two buffers before the binding experiment and therefore, the difference in the signal with this buffer on the surface is a combination of the bulk buffer effect and the surface modification due to the His-tag binding.

The monolayer headgroups were decharged and charged two times, followed by the binding of the pure His-tags. After the binding, the mono layer with His-tags was measured in nickel containing buffer, to have the same bulk effect and then the NTA headgroups were decharged and charged again several times. The difference between the nickel level before the addition of His-tags (level 1 in figure 6.3) and the nickel level directly after the addition of His-tags (level 2 in figure 6.3) is caused by the combination of specific and unspecific binding of the His-tags to the lipid mono layer. The difference between level 2 and the next nickel level after the bond was opened by EDTA (level 3 in figure 6.3) is caused by the specific binding of the His-tags only.

For the His-tag binding, no effect was measured. Obviously, the noise and the drift

(a)

(b)
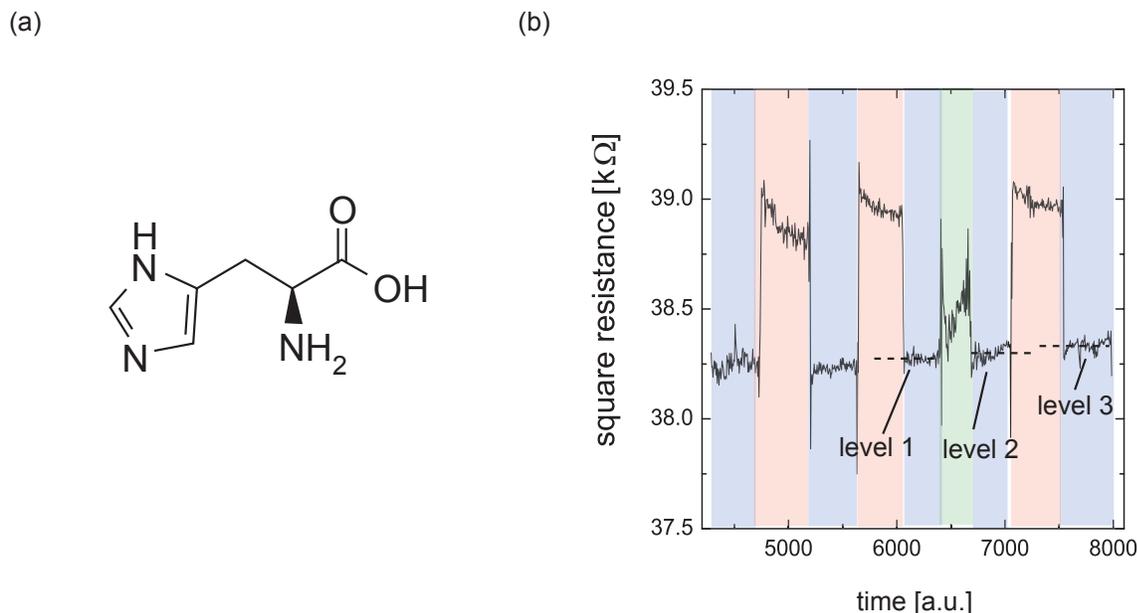
Figure 6.3: Molecular structure of the amino acid histidine. A His-Tag consists of 6 of these histidines connected with the covalent peptide bond (a). Response curve as obtained for the specific binding of his-tags (b). Different buffers are shaded in different colors, blue stands for nickel containing buffer, red for EDTA buffer and green for the His-tag buffer.

of the measurement limit the measurable effects to charge variation being bigger than the one caused by the His-tag binding. This is exactly what one expects, considering that for $pH = 7.5$ the histidine side chain is neutral and therefore the complete His-tag is uncharged.

6.1.2.   Binding of His-tagged Aspartic Acid

By adding a charged amino acid to the pure His-tag, a peptide with a controlled charge can be produced and the effect on the sensor signal can be measured. The natural amino acid aspartic acid has a negative charge at $pH = 7.5$ and the molecular structure is shown in 6.4 (a). An artificial peptide with 6 aspartic acids was chosen, having a net negative charge of $-6e^-$.

The binding experiment was done completely analog to the experiments with the pure His-tag. The measurement was also done on a ODMTS covered undoped sensor at $U_{bg} = +25\,V$ and with a DOGS-NTA concentration of 5%. Again, the three levels with nickel buffer at the surface, before the binding of His6Asp6 (level 1 in figure 6.4),

(a)

(b)
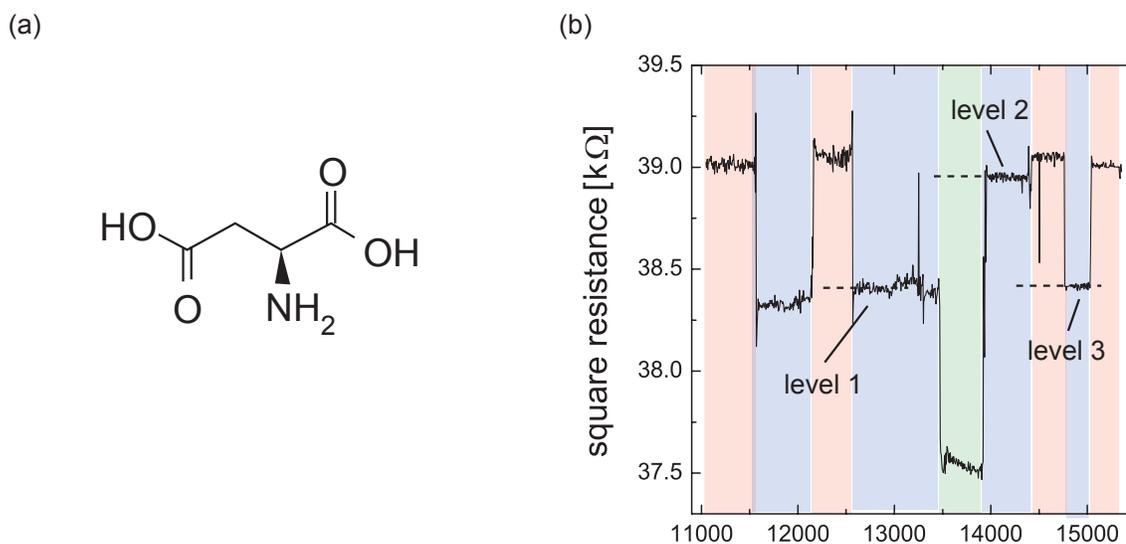
Figure 6.4: Molecular structure of the amino acid aspartic acid. At $pH = 7.5$, the left carboxylic acid in the side chain is dissociated and hence the net charge of aspartic acid is $-1e^-$. Response curve as obtained for the specific binding of the peptide His6Asp6 (b). Different buffers are shaded in different colors, blue stands for nickel containing buffer, red for EDTA buffer and green for the peptide buffer.

directly after the binding (level 2 in figure 6.4) and after the bond was opened again by EDTA (level 3 in figure 6.4) are compared. Again, the peptide containing buffer was not matched with the other two buffers before the binding experiment and therefore the difference in the signal with this buffer on the sensor surface is a combination of the bulk buffer effect and the surface modification due to the His6Asp6 binding.

The measured change in resistance for the binding experiments of the His6Asp6 peptide is shown in figure 6.4 (b). In the experiment, the difference between level 1 and level 2 is almost the same as between level 2 and 3, indicating that the binding of the peptide was mostly specific and therefore unspecific binding of the peptide is suppressed by a dense lipid layer. The measured change in resistance was $\Delta R = (533 \pm 19)\,\Omega$, corresponding to $\Delta\psi = (-7.3 \pm 0.3)\,mV$.

By looking at the sign of the measured signal, a sanity check can be performed. The resistance signal gets bigger after the binding of the peptide, which corresponds to added net negative charge at the surface of the undoped sensor devices. This fact corresponds well to the predictions of the net negative charge of the aspartic acids at neutral pH. A more quantitative interpretation of the obtained signal can be achieved
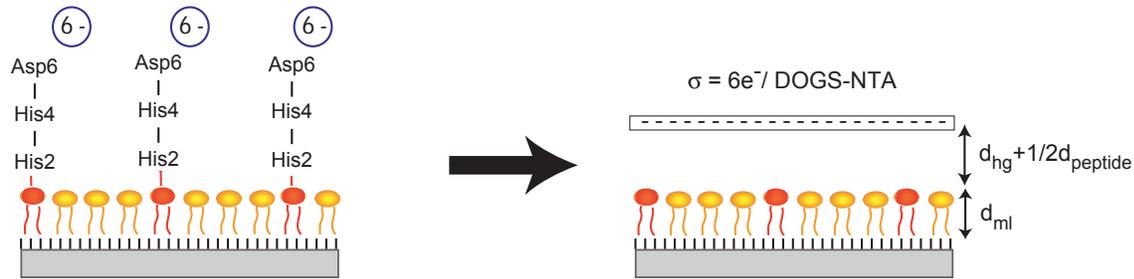
Figure 6.5: Sketch of the simplified model used to interpret the resistance changes for the specific binding of GFP to the DOGS-NTA lipids. The layer of bound, net negative charged GFP is approximated as a charged plate above the lipid layer.

by applying the adapted plate capacitor model from section 5.2 and modify it slightly as shown in figure 6.5. As the sensitive area of the device is huge ($80\mu m$ x $80\mu m$) in comparison to the average area per functional DOGS-NTA lipid ($65\mathring{A}^2$), the charges of the peptide can be assumed to be homogenously distributed over a plate. The discrete charges of the molecules bound to the DOGS-NTA can be approximated as a homogenous charge density σ, given by

$$\sigma = z\frac{1e^-}{65\mathring{A}^2}\frac{\%DOGS-NTA}{100} \qquad , \qquad (6.1)$$

where z is the number of charges per bound molecule. The lipid monolayer is modelled as ideal dielectric and as already discussed in the previous chapter, screening effects following the *Debye Hückel* approximation are assumed to take place in the head group region and the electrolyte. In a first approximation, the distance of the charge density from the head groups of the lipid layer can be assumed to be $\frac{1}{2}d_{peptide} + d_{hg}$, where $d_{peptide}$ is the persistence length of the artificial peptide and d_{hg} is the size of the chelate head group as obtained in section 5.2. If one assumes the size of an amino acid to be $3.6\mathring{A}$ [Stryer, L., 1994], one arrives at a length for the six aspartic acids of $6 \cdot 3.6\mathring{A} \approx 2.16\,nm$. According to equation 5.11, the expected change in potential for the binding of the artificial peptide in this model is given by

$$\Delta\psi = \frac{-6e^-}{65\mathring{A}^2}\frac{1/\kappa}{\epsilon_r\epsilon_0}\frac{\%DOGS-NTA}{100}e^{-\kappa\left(\frac{d_{peptide}}{2}+d_{hg}\right)}\frac{1}{1-\kappa\,d_{ml}} \qquad . \qquad (6.2)$$

Inserting the values of $d_{ml} = 1.5\,nm$, $\epsilon_r = 2.2$, $1/\kappa = 0.4\,nm$, $\%DOGS-NTA = 5$ and $d_{hg} \approx 1.6\,nm$, one obtains a theoretical prediction of $\Delta\psi \approx -0.7\,mV$. Compared

to the measured effect of $\Delta\psi = (-7.3 \pm 0.3)\,mV$ this is an order of magnitude smaller. This difference can be explained by a smaller screening length near a surface and additionally, because the assumption of all charges sitting at half the distance is a rather crude estimate. The exact geometry of the His6Asp6 peptide sitting on the lipid head groups is not known and a slight tilt angle will have a big effect on the expected response due to the exponential dependance of the signal from the distance of the charges.

Nevertheless, the obtained signal is excellent and the binding was specific, proofing that unspecific adsorption of the peptide did not occur due to a good passivation layer. With these experiments, the detection of a natural protein with His-tag is shown to be possible and the results of these measurements are shown in the next section.
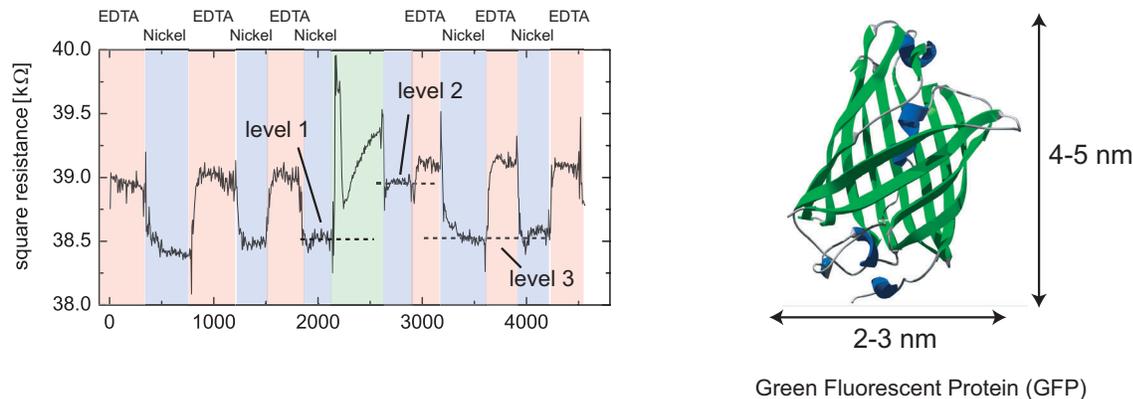
Figure 6.6: Response curve as obtained for the specific binding of GFP (shown on the right). The charging and decharging was observable before and after the binding. The specific GFP binding corresponds to a change in the resistance between level 2 and 3 of $\Delta R = (411 \pm 32)\,\Omega$ or $\Delta \psi = (-4.8 \pm 0.4)\,mV$.

6.2   Specific Detection of His-tagged GFP

The binding of His-tagged GFP to NTA chelator lipids has been studied quite extensively using SPR and fluorescence microscopy [Rädler et al., 2000, Thess et al., 2002, Hutschenreiter et al., 2003]. The binding is highly specific and reversible upon the addition of EDTA, which opens the chelate complex by taking out the nickel ion. The primary sequence of GFP contains 238 amino acids with a molecular weight of $\approx 30 kDa$. The size of a GFP protein is roughly $2.5\,nm$ x $4.8\,nm$ (figure 6.6) and in the amino acid sequence of GFP there are eight amino acids with negative side chain more than amino acids with positive side chains, indicating that GFP has a net negative charge at neutral pH.

Again, the binding experiment was done completely analog to the experiments with the pure His-tag. The measurement was also done on a ODMTS covered undoped sensor at $U_{bg} = +25\,V$ and with a DOGS-NTA concentration of 5%. Again, the three levels with nickel buffer at the surface, before the binding of GFP (level 1 in figure 6.6), directly after the binding (level 2 in figure 6.6) and after the bond was opened again by EDTA (level 3 in figure 6.6) are compared. Again, the protein containing buffer was not matched with the other two buffers before the binding experiment and therefore the difference in the signal with this buffer on the sensor surface is a combination of the bulk buffer effect and the surface modification due to the GFP
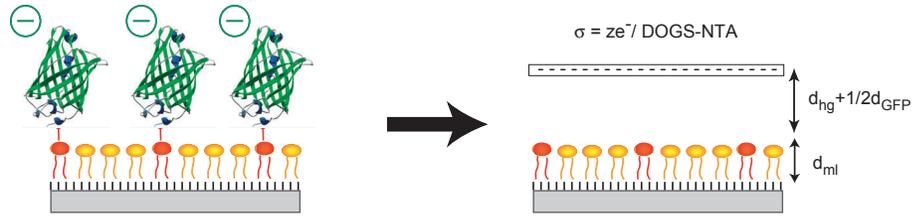
Figure 6.7: Sketch of the simplified model used to interpret the resistance changes for the specific binding of GFP to the DOGS-NTA lipids. The layer of bound, net negative charged GFP is approximated as a charged plate above the lipid layer.

binding.

The measured change in resistance for the binding experiments of GFP is shown in figure 6.6 (b). In the experiment, the difference between level 2 and 3 was $\Delta R = (411 \pm 32)\,\Omega$. From the calibration measurement, the corresponding change in potential is $\Delta\psi = (-4.8 \pm 0.4)\,mV$. The effect of the unspecific binding (difference between level 1 and level 3) could not be resolved in the noise and the signal drift of the measurement, indicating that the binding of GFP was mostly specific.

As a first interpretation of the signal, a sanity check can be performed by looking at the sign of the measured resistance change. The resistance gets bigger after the binding of GFP, showing that the net charge added at the surface is negative, which corresponds well to the predictions of the net negative charge of a GFP protein at a $pH = 7.5$ as used in this experiments. In addition, to interpret the obtained signal more quantitively, one can apply the same simple plate capacitor model as for the binding of the His6Aps6 in the previous section. The resulting model is shown in figure 6.7. With the same argumentation as before, the discrete charges on the GFP molecules bound to the DOGS-NTA can be approximated as a homogenous charge density σ and in a first approximation, the distance of the charge density from the head groups of the lipid layer can be assumed to be at the middle of the maximum size of a GFP molecule. Analog to the model for the artificial peptide, screening effects are assumed to occur in the head group region and in the electrolyte. Completely analog to equation 5.9, the expected change in potential is then given by

$$\Delta\psi = z\,\frac{1e^-}{65\mathring{A}^2}\,\frac{1/\kappa}{\epsilon_r\epsilon_0}\,\frac{\%DOGS-NTA}{100}\,e^{-\kappa\left(\frac{d_{GFP}}{2}+d_{hg}\right)}\,\frac{1}{1-\kappa\,d_{ml}} \qquad . \qquad (6.3)$$

Inserting the values corresponding to the experimental conditions, $d_{GFP} = 4\,nm$,

$1/\kappa = 0.4\,nm$, $d_{ml} = 1.5\,nm$, $\epsilon_r = 2.2$, $\%DOGS - NTA = 5$ and $\Delta\psi = (-4.8 \pm 0.4)\,mV$ and assuming $z \approx -8$, one gets $\Delta\psi \approx -0.1\,mV$, which is again smaller than the measured response. The difference can be explained completely analog to the argumentation for the His6Asp6 peptide in the previous section: The screening length near a charged surface is smaller than the bulk value and additionally the exact orientation of the GFP molecules at the surface is not known. The assumption that all proteins are arranged and sitting perpendicular to the surface is not valid. A slight tilt angle of the molecules will have a big effect on the expected response due to the exponential dependance of the signal from the distance of the charges and therefore the measured signal is higher than the predicted one.

The maximum sensitivity can be estimated by assuming that all DOGS-NTA lipids were charged with one GFP molecule. Under this assumption, the presented measurement with 5% functional lipids corresponds to a sensitivity of 1 GFP / 1300 $\mathring{A}^2$. The detection of signals being a factor of 5 smaller is possible before the signal disappears in the noise level and as shown for the lipid membrane charge sensor, the signal depends linearly on the deposited surface charge. Therefore, the maximum sensitivity of this sensor device towards the detection of GFP can be taken to be $1\,GFP/\,65\,nm^2$.

6.3 Specific Detection of His-tagged LuSy

As a second example for the detetion of a natural protein, Histidine$_{360}$ Lumazin-synthase (His$_{360}$LuSy) was used. His$_{360}$LuSy is a 60-mer icosaedric protein with a diameter of $15\,nm$. Each monomer has one 6-His linker, resulting in 360 histidines or 60 functional linkers for the NTA headgroups. In the primary amino sequence, at $pH = 7.5$ there are 3 more amino acids with negative than with positive side chain, resulting in a predicted net negative charge of $-180\,e^-$ for LuSy without the histidine linkers.
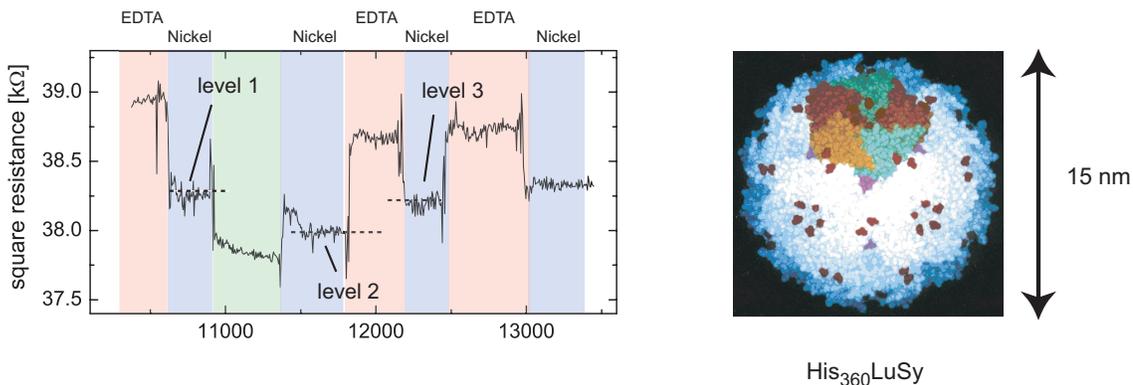
Figure 6.8: Obtained resistance signal for the specific detection of LuSy (shown on the right). EDTA buffer is shaded red, nickel buffer blue. Again, the shift of the signal after the binding was undone and the slight offset of the signal shows that part of signal was due to unspecific adsorption.

Figure 6.8 shows the obtained signal for the binding of LuSy to a lipid monolayer with 5% DOGS-NTA. Again, the presence and functionality of the DOGS-NTA was verified by measuring the charging and decharging with Ni/EDTA before the binding. The LuSy containing buffer was not matched with the other two buffers, resulting in a mix of bulk effect and surface effect of the LuSy during the surface is exposed to this buffer. However, if the bulk buffer is switched back to nickel buffer, the obtained difference in signal is due to the specific binding of the LuSy only. The same argumentation as for the GFP binding in the previous section for the specific and unspecific part of the signal leads to a net change in resistance of $\Delta R = (-175 \pm 86)\,\Omega$ or $\Delta \psi = (2 \pm 0.4)\,mV$ for the specific binding.

This result is surprising, because for such a strong negative charge of $-180e^-$ as predicted from the primary amino acid sequence, one would expect first, a bigger

effect and second, the effect measured here goes to the direction of a more positive surface, contradicting the excess of amino acids with negative side chains.

However, this seemingly contradictory result can easily be explained by taking into account that each monomer has the possibility to bind positive nickel ions, contributing a high positive charge on the outer edge of the LuSy. Hence a net charge of the His_{360} LuSy complexed with many nickel ions close to zero or even slightly positive seems to be reasonable.

6.4   Summary and Discussion

The experiments to detect the specific binding of artificial peptides and natural proteins with His-tag were successful and represent the first measurement of protein binding events to a biocompatible surface with a semiconductor based sensor device. The pure His-tag was shown to have no effect and for the artificial His6Asp6 peptide a signal of $\Delta\psi = (-7.3 \pm 0.3)\,mV$ was detected. For the binding of natural GFP, a signal of $\Delta\psi = (-4.8 \pm 0.)\,mV$ was obtained. The direction of both signals agrees with a net negative charge deposited on the surface, as expected from the primary amino acid sequence. Moreover, the size of the measured signals are explainable in a simple plate capacitor model with the assumption of the Debye Hückel approximation being valid in the headgroup region and the electrolyte. Extrapolating the result, the maximum sensitivity of the sensor device covered with the functional lipid mono layer can be estimated to be in the range of 1 peptide/$65\,nm^2$. As the net charge of the GFP is several elementary charges, on a miniaturized sensitive area the detection of only a few proteins should be possible.

Compared to impedance spectroscopy experiments with lipid monolayers on ITO, the obtained sensitivity is much higher, as impedance spectroscopy was not sensitive enough to detect the specific binding of GFP to the chelator lipids [Hillebrandt et al., 2002].

SPR measurements on lipid mono layers on hydrophobic gold surfaces were successful to detect the binding of GFP [Dorn, 1998]. The noise of the signal in these experiments was about 10 RU, where 1000 RU corresponds to a protein concentration of $1 ng/mm^2$ and hence the maximum sensitivity was $0.01\,ng/mm^2$. This can be calculated to a sensitivity against charges by accounting for a molecular mass of the GFP of $30 kDa$ and assuming a net charge per GFP of $\approx 5e^-$, resulting in a sensitivity of $1e^-/10000\,nm^2$. This value is two orders of magnitude higher than the obtained

sensitivity with the SOI sensor devices. As discussed before, this is not very surprising, as SPR measures the change of refractive index, which scales with the mass deposited at the surface, whereas the SOI sensor measures charges. Consequently, for the charging experiments with nickel ions, the sensitivity is comparable, whereas for the protein binding SPR has a much higher sensitivity, because the ratio of deposited mass to deposited charge is much higher for GFP than for nickel.

However, as discussed in section 3, the sensitivity of the developed SOI sensor can be drastically increased by improving the measurement setup or optimizing the doping concentration and it will be a task for future experiments to increase the sensitivity.

Additionally, the developed SOI sensor device has several advantages, such as the possibility for a parallel detection of many proteins and the direct electrical signal caused by the binding event. The SOI sensor measures the effective charged rather than the deposited mass at the surface. Therefore, by inverting the argumentation used in the last chapters, for a known geometry the SOI sensor is an excellent tool to determine the charge of unknown proteins, a very important problem in the classification of proteins.

7 Outlook

The experiments performed in this work successfully showed the suitability of SOI as substrate for semiconductor based sensor devices. With the developed sensor, a lot of different experiments can be performed in the future and some of them will be presented here.

Certainly, the first step will be to optimize the measurement setup and the semiconductor technology. Employing a differential setup will increase the sensitivity because drift effects can be subtracted. Optimizing the shielding and the doping profile in the sensor layer will increase the slope of the $R(U_{ref})$ curves and therefore increase the sensitivity. The development of a differential sensor already started and first experiments are planed in the near future.

Apart from the technological optimizations, experiments with biological background are very interesting to perform. First experiments to detect the hybridization of DNA show very promising results [Neff et al., 2004]. The primary strand of DNA can be immobilized either by polyelectrolyte adsorption with a poly-l-lysine/DNA system or covalently coupled to the surface with biotinylated BSA and streptavidin. The results obtained so far show that for the detection of a single base pair mismatch, a differential setup will be needed.

Additionally, the experiments to detect the specific binding of proteins certainly need to be extendend. For example, the controlled incorporation of a charge into the primary sequence of a protein can be reached by incorporating additional charged amino acids. Enzymatic reactions can be observed with other other lipid systems such as the cutting of the phosphate headgroups of of phosphatidylinositol 4,5 bisphosphate by phospholipase C-β.

In figure 7.1, other future experiments are illustrated. In part (a), a sensor with several different sensitive fields in parallel, functionalized with different receptors is shown. Applications for such a sensor range from the screening of new drugs to the analysis of the genetic information encoded on the messenger RNA. The already started development of the differential sensor with two sensitive field is the first step into this direction.
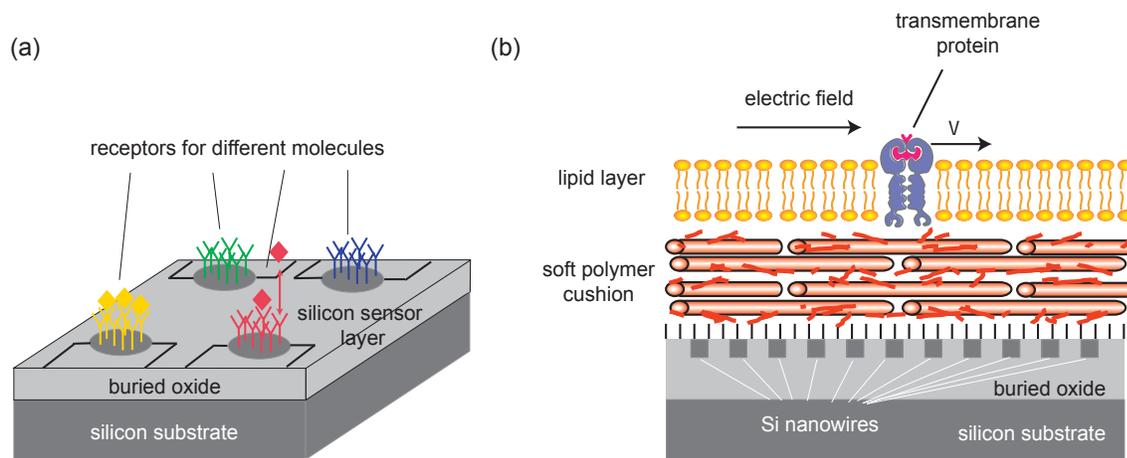
Figure 7.1: Sketch of two experiments for future work on the SOI sensor devices. (a) shows a sensor
with different sensitive fields, being able to screen many interactions in parallel. A sensor
structured into many nanowires can serve as substrate and detector for the membrane
based electrophoresis of transmembrane proteins incorporated into lipid layers as shown
in (b).

Part (b) illustrates an even more sophisticated experiment, which has already
been started by the development of a new chip design and the outsourcing of the
chip production to a professional semiconductor production facility at the *Fraunhofer
Institute*. In principle, many different narrow lines, nano wires can be produced on a
SOI wafer. On top of a suited passivation layer, amphiphilic polymers representing a
soft cushion can be deposited. These cushions allow the incorporation of big trans-
membrane proteins into lipid layers without denaturing at the surface. By applying
an electric field in the electrolyte solution, the electrophoresis of these proteins can
be monitored by the signals the protein causes in the different nanowires.

Even though some of these experiments are challenging, the experiments per-
formed in this work proofed the principle of the underlying ideas and makese a further
proceeding worthwhile to follow.

Bibliography

[Adlkofer et al., 2000] Adlkofer, K., Tanaka, M., Hillebrandt, H., Wiegand, G., Sackmann, E., Bolom, T., Deutschmann, R., and Abstreiter, G. (2000). Electrochemical passivation of gallium arsenide surface with organic self-assembled monolayers in aqueous electrolytes. *Applied Physics Letters*, 76(22):3313–3315.

[B. Alberts, A. Johnson, J. Lewis, M. Raff, K. Roberts, P. Walter, 2002] B. Alberts, A. Johnson, J. Lewis, M. Raff, K. Roberts, P. Walter (2002). *Molecular Biology of the Cell*. Garland Science, New York, 4th edition.

[Bausch et al., 1999] Bausch, A. R., Moller, W., and Sackmann, E. (1999). Measurement of local viscoelasticity and forces in living cells by magnetic tweezers. *Biophysical Journal*, 76(1):573–579.

[Bergveld, 1970] Bergveld, P. (1970). Development of an ion-sensitive solid-state device for neurophysiological measurements. IEEE *Transactions On Biomedical Engineering*, BM17(1):70–72. IEEE TRANS BIOMED ENG.

[Bergveld and Sibbald, 1988] Bergveld, P. and Sibbald, A. (1988). *Analytical and Biomedical Application of Ion-Selective-Field-Effect Transistors*, volume XXIII of *Comprehensive Analytical Chemistry*. Elsevier, Amsterdam-Oxford-New York-Tokyo.

[Bousse et al., 1983] Bousse, L., Derooij, N. F., and Bergveld, P. (1983). Operation of chemically sensitive field-effect sensors as a function of the insulator-electrolyte interface. *IEEE Transactions on Electron Devices*, 30(10):1263–1270.

[Brunner, 2002] Brunner, K. (2002). Si/Ge nanostructures. *Reports on Progress in Physics*, 65:27–72.

[Cevc, G., 1993] Cevc, G. (1993). *Phospholipids Handbook*. Marcel Dekker, New York.

[Chee et al., 1996] Chee, M., Yang, R., Hubbell, E., Berno, A., Huang, X. C., Stern, D., Winkler, J., Lockhart, D. J., Morris, M. S., and Fodor, S. P. A. (1996). Accessing genetic information with high-density DNA arrays. *Science*, 274(5287):610–614.

[Ciu et al., 2001] Ciu, Y., Wei, Q., Park, H., and Lieber, C. M. (2001). Nanowire nanosensors for highly sensitive and selective detection of biological and chemical species. *Science*, 293:1289–1292.

[Cooper et al., 2001] Cooper, E., Fritz, J., Wiegand, G., Wagner, P., and Manalis, S. (2001). Robust microfabricated field-effect sensor for monitoring molecular adsorption in liquids. *Applied Physics Letters*, 79(23):3875.

[Cornell et al., 1997] Cornell, B. A., Braach-Maksvytis, V. L. B., King, L. G., Osman, P. D. J., Raguse, B., Wieczorek, L., and Pace, R. J. (1997). A biosensor that uses ion-channel switches. *Nature*, 387(6633):580–583.

[Decher, 1997] Decher, G. (1997). Fuzzy nanoassemblies: Toward layered polymeric multicomposites. *Science*, 277(5330):1232–1237.

[Dietrich et al., 1995] Dietrich, C., Schmitt, L., and Tampe, R. (1995). Molecular-organization of histidine-tagged biomolecules at self-assembled lipid interfaces using a novel class of chelator lipids. *Proceedings of the National Academy of Sciences of the United States of America*, 92(20):9014–9018.

[Dilger et al., 1979] Dilger, J. P., McLaughlin, S. G. A., McIntosh, T. J., and Simon, S. A. (1979). Dielectric-constant of phospholipid-bilayers and the permeability of membranes to ions. *Science*, 206(4423):1196–1198.

[Dong et al., 2004] Dong, Y. M., Chen, J., Wang, X., and Chen, M. (2004). Optimized implant dose and energy to fabricate high-quality patterned simox soi materials. *Solid State Communications*, 130(3-4):275–279.

[Dorn, 1998] Dorn, I. (1998). *Chelator lipid membranes as universal biofunctional interfaces for structural and functional studies on immobilized proteins*. Dissertation, TU München.

[Dorn et al., 1998] Dorn, I. T., Pawlitschko, K., Pettinger, S. C., and Tampe, R. (1998). Orientation and two-dimensional organization of proteins at chelator lipid interfaces. *Biological Chemistry*, 379(8-9):1151–1159.

[Elender et al., 1996] Elender, G., Kuhner, M., and Sackmann, E. (1996). Functionalisation of si/sio2 and glass surfaces with ultrathin dextran films and deposition of lipid bilayers. *Biosensors and Bioelectronics*, 11(6-7):565–577.

[Florin and Gaub, 1993] Florin, E. L. and Gaub, H. E. (1993). Painted supported lipid-membranes. *Biophysical Journal*, 64(2):375–383.

[Fodor, 1997] Fodor, S. (1997). Massively parallel genomics. *Science*, 277:393–395.

[Fodor et al., 1991] Fodor, S. P. A., Read, J. L., Pirrung, M. C., Stryer, L., Lu, A. T., and Solas, D. (1991). Light-directed, spatially addressable parallel chemical synthesis. *Science*, 251(4995):767–773.

[Fritz et al., 2002] Fritz, J., Cooper, E. B., Gaudet, S., Sorger, P. K., and Manalis, S. R. (2002). Electronic detection of dna by its intrinsic molecular charge. *Proceedings of the National Academy of Sciences of the United States of America*, 99(22):14142–14146.

[Gartsman et al., 1998] Gartsman, K., Cahen, D., Kadyshevitch, A., Libman, J., Moav, T., Naaman, R., Shanzer, A., Umansky, V., and Vilan, A. (1998). Molecular control of a gaas transistor. *Chemical Physics Letters*, 283(5-6):301–306.

[Hillebrandt et al., 2002] Hillebrandt, H., Tanaka, M., and Sackmann, E. (2002). A novel membrane charge sensor: Sensitive detection of surface charge at polymer/lipid composite films on indium tin oxide electrodes. *Journal of Physical Chemistry B*, 106(2):477–486.

[Hoppe et al., 1982] Hoppe, W., Lohmann, W., Markl, H., and Ziegler, H. (1982). *Biophysik*. Springer Verlag, Berlin, Heidelberg, New York.

[Hutschenreiter et al., 2003] Hutschenreiter, S., Neumann, L., Rädler, U., Schmitt, L., and Tampe, R. (2003). Metal-chelating amino acids as building blocks for synthetic receptors sensing metal ions and histidine-tagged proteins. *Chembiochem*, 4(12):1340–1344.

[Israelachvili, J.N., 1985] Israelachvili, J.N. (1985).   *Intermolecular and Surface Forces*. Academic Press, London.

[Kern and Puotinen, 1970] Kern, W. and Puotinen, D. (1970). Cleaning solutions based on hydrogen peroxide for use in silicon semiconductor technology. *RCA Review*, 31:187–206.

[Kharitonov et al., 2001] Kharitonov, A. B., Wassermann, J., Katz, E., and Willner, I. (2001). The use of impedance spectroscospy for the characterization of protein-modified isfet devices: Application of the method for the analysis of biorecognition process. *Journal of Physical Chemistry B*, 105:4205–4213.

[Kuhner et al., 1994] Kuhner, M., Tampe, R., and Sackmann, E. (1994). Lipid mono-layer and bilayer supported on polymer-films - composite polymer-lipid films on solid substrates. *Biophysical Journal*, 67(1):217–226.

[Lang et al., 1994] Lang, H., Duschl, C., and Vogel, H. (1994). A new class of thi-olipids for the attachment of lipid bilayers on gold surfaces. *Langmuir*, 10(1):197–210.

[Lavalle et al., 2004] Lavalle, P., Picart, C., Mutterer, J., Gergely, C., Reiss, H., Voegel, J. C., Senger, B., and Schaaf, P. (2004). Modeling the buildup of polyelectrolyte multilayer films having exponential growth. *Journal of Physical Chemistry B*, 108(2):635–648.

[Lindner, 2003] Lindner, J. (2003).   The sample preparation was done at the Universität Augsburg, TEM picture taken with the help of J. Lindner, Augsburg.

[Luber, 2002] Luber, S. (2002). The processing of the lithographic mask was done by S. Luber at the Walther Schottky Institute of the TU Munich.

[Miller et al., 1990] Miller, C., Cuendet, P., and Gratzel, M. (1990). K+ sensitive bilayer supporting electrodes. *Journal of Electroanalytical Chemistry*, 278(1-2):175–192.

[Neff et al., 2004] Neff, P., Lud, S., Nikolaides, M., and Bausch, A. (2004). Unpublished results.

[Nissen et al., 1999] Nissen, J., Gritsch, S., Wiegand, G., and Rädler, J. O. (1999). Wetting of phospholipid membranes on hydrophilic surfaces - concepts towards self-healing membranes. *European Physical Journal B*, 10(2):335–344.

[Ormo et al., 1996] Ormo, M., Cubitt, A. B., Kallio, K., Gross, L. A., Tsien, R. Y., and Remington, S. J. (1996). Crystal structure of the aequorea victoria green fluorescent protein. *Science*, 273(5280):1392–1395.

[P. Atkins, J. de Paula, 2002] P. Atkins, J. de Paula (2002). *Physical Chemistry*. Oxford University Press, Oxford, UK, 7th edition.

[Parikh et al., 1999] Parikh, A. N., Beers, J. D., Shreve, A. P., and Swanson, B. I. (1999). Infrared spectroscopic characterization of lipid-alkylsiloxane hybrid bilayer membranes at oxide substrates. *Langmuir*, 15(16):5369–5381.

[Plant, 1993] Plant, A. L. (1993). Self-assembled phospholipid alkanethiol biomimetic bilayers on gold. *Langmuir*, 9(11):2764–2767.

[Plant, 1999] Plant, A. L. (1999). Supported hybrid bilayer membranes as rugged cell membrane mimics. *Langmuir*, 15(15):5128–5135.

[Rädler and Sackmann, 1997] Rädler, J. and Sackmann, E. (1997). Functionalization of solids by ultrathin soft polymer films and polymer/lipid film composites: Modeling of cell surfaces and cell recognition processes. *Current Opinion in Solid State & Materials Science*, 2(3):330–336.

[Rädler et al., 2000] Rädler, U., Mack, J., Persike, N., Jung, G., and Tampe, R. (2000). Design of supported membranes tethered via metal-affinity ligand-receptor pairs. *Biophysical Journal*, 79(6):3144–3152.

[Rauschenbach, 2002] Rauschenbach, S. (2002). *Entwicklung eines oberflächensensitiven Halbleiterwiderstandes für den Nachweis von Biomolekülen*. Diplomarbeit, Universität Augsburg.

[Riedl and Brunner, 2002] Riedl, H. and Brunner, K. (2002). The MBE overgrowth was done at the Walther Schottky Institute of the TU Munich with the help of H. Riedl and K. Brunner.

[Sackmann, 1996] Sackmann, E. (1996). Supported membranes: Scientific and practical applications. *Science*, 271(5245):43–48.

[Salafsky et al., 1996] Salafsky, J., Groves, J. T., and Boxer, S. G. (1996). Architecture and function of membrane proteins in planar supported bilayers: A study with photosynthetic reaction centers. *Biochemistry*, 35(47):14773–14781.

[Schmitt et al., 1994] Schmitt, L. Dietrich, C., , and Tampe, R. (1994). Synthesis and characterization of chelator-lipids for reversible immobilization of engineered proteins at self-assembled lipid interfaces. *Journal of the American Chemical Society*, 116:8485–8491.

[Schmitt et al., 1996] Schmitt, L., Bohanon, T. M., Denzinger, S., Ringsdorf, H., and Tampe, R. (1996). Specific protein docking to chelator lipid monolayers monitored by FTIR spectroscopy at the air-water interface. *Angewandte Chemie-International Edition in English*, 35(3):317–320.

[Schoenhoff, 2003] Schoenhoff, M. (2003). Self-assembled polyelectrolyte multilayers. *Current Opinion in Colloid and Interface Science*, 8:86–95.

[Sigl et al., 1997] Sigl, H., Brink, G., Seufert, M., Schulz, M., Wegner, G., and Sackmann, E. (1997). Assembly of polymer/lipid composite films on solids based on hairy rod LB-films. *European Biophysics Journal with Biophysics Letters*, 25(4):249–259.

[Singer and Nicolson, 1972] Singer, S. J. and Nicolson, G. L. (1972). Fluid mosaic model of structure of cell-membranes. *Science*, 175(4023):720–731.

[Siu and Cobbold, 1979] Siu, W. M. and Cobbold, R. S. C. (1979). Basic properties of the electrolyte-Sio2-Si system - physical and theoretical aspects. *IEEE Transactions On Electron Devices*, 26(11):1805–1815.

[Sonnefeld, J. and Löbbus, M. and Vogelsberger, W., 2001] Sonnefeld, J. and Löbbus, M. and Vogelsberger, W. (2001). Determination of electric double layer parameters for spherical silica particles under application of the triple layer model using surface charge density data and results of electrokinetic sonic amplitude measurements. *Colloids and Surfaces, A*, 195:215.

[Steinem et al., 1996] Steinem, C., Janshoff, A., Ulrich, W. P., Sieber, M., and Galla, H. J. (1996). Impedance analysis of supported lipid bilayer membranes: A scrutiny of different preparation techniques. *Biochimica Et Biophysica Acta-Biomembranes*, 1279(2):169–180.

[Steinhoff et al., 2003] Steinhoff, G., Hermann, M., Schaff, W. J., Eastman, L. F., Stutzmann, M., and Eickhoff, M. (2003). ph response of gan surfaces and its application for ph-sensitive field-effect transistors. *Applied Physics Letters*, 83(1):177–179. Article.

[Stelzle et al., 1993] Stelzle, M., Weissmuller, G., and Sackmann, E. (1993). On the application of supported bilayers as receptive layers for biosensors with electrical detection. *Journal of Physical Chemistry*, 97(12):2974–2981.

[Stryer, L., 1994] Stryer, L. (1994). *Biochemie*. Spektrum Chemie, Heidelberg, Berlin, Oxford, 2nd edition.

[Sze, S.M., 1981] Sze, S.M. (1981). *Physics of Semiconductor Devices*. John Wiley & Sons, New York, 2nd edition.

[Tamm and McConnell, 1985] Tamm, L. K. and McConnell, H. M. (1985). Supported phospholipid-bilayers. *Biophysical Journal*, 47(1):105–113.

[Thess et al., 2002] Thess, A., Hutschenreiter, S., Hofmann, M., Tampe, R., Baumeister, W., and Guckenberger, R. (2002). Specific orientation and two-dimensional crystallization of the proteasome at metal-chelating lipid interfaces. *Journal of Biological Chemistry*, 277(39):36321–36328.

[Tong and Gosele, 1993] Tong, Q. Y. and Gosele, U. (1993). Fabrication of ultrathin soi by simox wafer bonding (swb). *Journal of Electronic Materials*, 22(7):763–768.

[Ulman, 1991] Ulman, A. (1991). *An introduction to ultrathin organic films: From Langmuir-Blodgett to self-assembly*. Academic Press, Boston, USA.

[Vogl et al., 2004] Vogl, P., Hackenbuchner, S., Birner, S., Zandler, G., Sabathil, M., and Majewski, J. (2004). http://www.wsi.tum.de/nextnano3/.

[Wu et al., 2001] Wu, G., Cahen, D., Graf, P., Naaman, R., Nitzan, A., and Shvarts, D. (2001). Direct detection of low-concentration NO in physiological solutions by a new GaAs-based sensor. *Chemistry - A European Journal*, 7(8):1743–1749.

[Yonehara et al., 1994] Yonehara, T., Sakaguchi, K., and Sato, N. (1994). Epitaxial layer transfer by bond and etch back of porous Si. *Applied Physics Letters*, 64(16):2108.

[Zeck, G. and Fromherz, P., 2001] Zeck, G. and Fromherz, P. (2001). Noninvasive neuroelectronic interfacing with synaptically connected snail neurons immobilized on a semiconductor chip. *Proceedings of the National Academy of Sciences of the United States of America*, 98(18):10457.

Appendix

Appendix A: Semiconductor Technology - Process Details   The production process is described also in chapter 2.1. Basically the process consisted from the following steps:

- Wafer cutting and breaking on a Karl Suess Microtech Ritztisch to single pieces of *9.3 mm x 9.3 mm.*

- Ultrasound cleaning of the wafers in acetone and isopropanol for 3 minutes.

- Spincoating of the photoresist for structure etching (S*S1805*, Shipley, USA) for *40 s* with *6000 rpm.*

- Soft bake tempering step before illumination for 30 min at 90º.

- Illumination of the resist over the photo mask on a mask aligner (Karl Suss Microtec MJB 3, Munich) with a UV-lamp for *10 s.*

- Developing the resist in developer (Hoechst, AZ 351B) for 7s and drying under nitrogen.

- Hard bake for 2 hours at 120º.

- Etching in a 3:7 mixture of concentrated HNO_3 (67%) and diluted HF (1.5%) until a color change was visible when the complete silicon was removed. The etching time strongly depended on the doping concentration. For $10^{16}cm^{-3}$, the color change occurred after 90s, for $10^{18}cm^{-3}$ already after 40s.

- Cleaning of the chips in water and isopropanol. Removing the photoresist in acetone and cleaning again in isopropanol and acetone.

- Optional Dektak measurement of the etching depth.

- Spincoating photoresist for the metallization (*S1818*, Shipley, USA) with 10000 *rpm* for *40 s.*

- Soft bake tempering step before illumination for 30 min at 90º.

- Developing the resist in developer (Hoechst, AZ 351B) for 7s and drying under nitrogen.

- Hard bake for 2 hours at 120º.

- HF dip to remove the native oxide by exposing the wafer for *60 s* to HF vapor.

- Gluing the substrates to a glass slide with wax. The glass slides were placed in a sample holder facing down in the evaporation chamber.

- Evaporation of the chamber to a pressure of $10^{-7} mbar$, deposition of $10 nm$ Ti and $200 nm$ Au by e-beam.

- Lift-off by sonication of the wafer at 20% intensity in acetone and intensively rinsing with fresh acetone. After 30 s, the photoresist began to be dissolved and the metal was left only in the contact regions.

- Optional silanization with ODTMS (see section 2.2.2.).

- Bonding into a chip carrier. The contact to the chip had to be done with a two component conducting glue (*Epotek RS 20*) to avoid breakthrough of the buried oxide during the bond formation.

- Encapsulation with silicon rubber (*RTV-1*, Roth Chemicals, Germany)
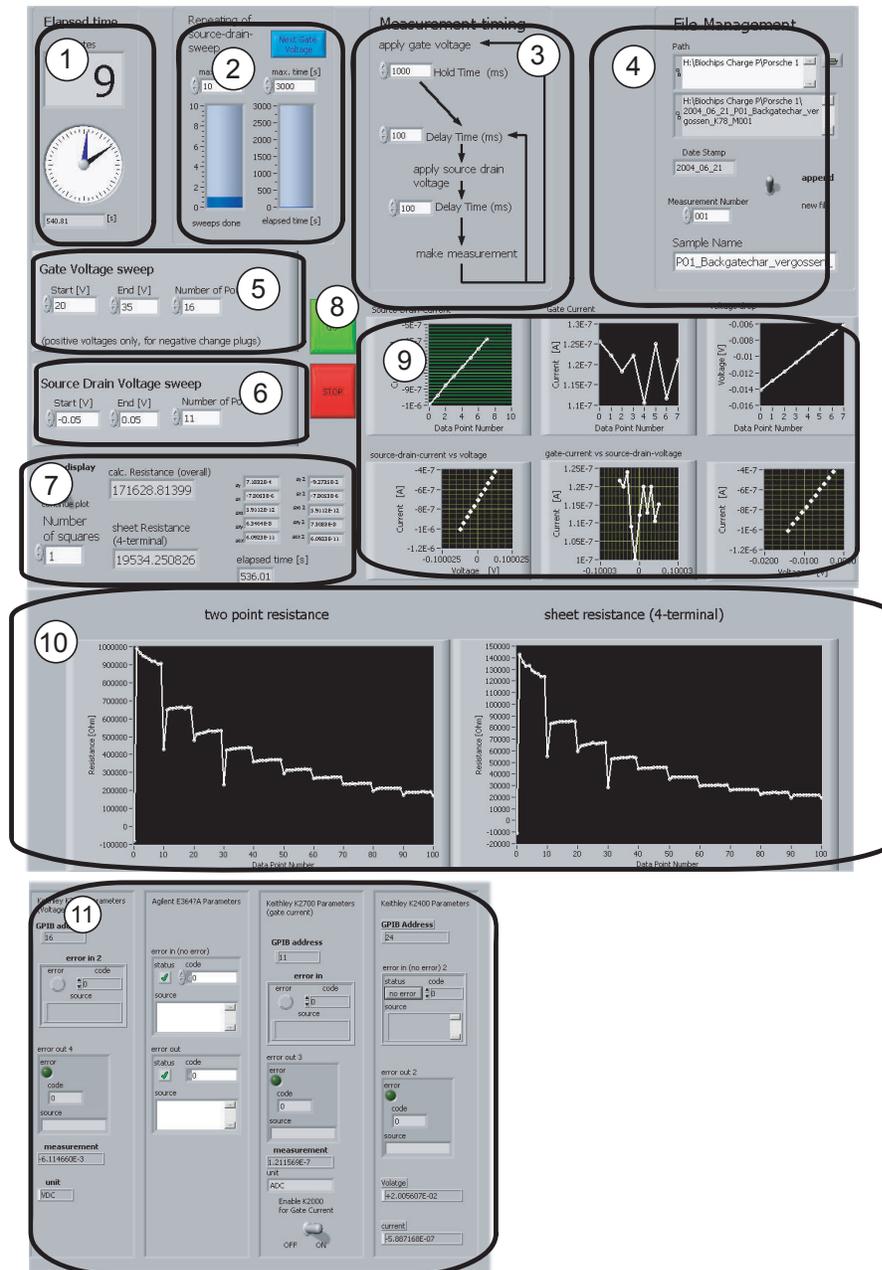
Figure 7.2: Screenshot of the front panel of the measurement software. The detailed function and meaning of the different parameters is given below.

Appendix B: Measurement Program - Details The software program written to perform the measurements is based on the software *LabView* and the program itself was intended to be self explaining. Nevertheless, a short manual of the basic

features of the program is given below.

Figure 7.2 shows the front panel of the program. All relevant parameters can be set here.

1 *The measurement time of the running measurement is shown in minutes as a digitized indicator and as an old fashioned clock.*

2 *The maximum duration for one gate voltage is set here. Both, the number of characteristics or the maximum time can be set. The program switches to the next gate voltage, when the one of the numbers is reached.*

3 *The measurements are carried out as shown here. First, the inner loop (one single current-voltage characteristic) is fulfilled, then the outer loop (different gate voltages). The time between the measurement points can be set here for both loops.*

4 *File management window. For each measurement, a separate folder is created with actual date and number of measurement.*

5 *The parameters for the gate voltage sweep (outer loop) are set here. The upper and lower border as well as the number of intermediate points can be chosen separately.*

6 *The parameters for the source drain voltage sweep (inner loop, current-voltage characteristic) are set here. The upper and lower border as well as the number of intermediate points can be chosen separately.*

7 *The actual measurement values are shown as digits in this window. Optionally, the display can be cleared.*

8 *Start and Stop button for the measurement. Optionally, the measuremnts can also be stopped by the general LabView Stop button.*

9 *Graphical result window. The actual four point measurement is shown in the upper right graph, the two point measurement in the upper left graph. The upper middle graph shows the leakage current. In the bootom part, the last measurement is shown.*

10 *In the left part, the two point resistance is shown versus time, in the right part the four point resistance. This window serves to monitor the measurements online during the buffer exchanges.*

11 *Parameters to control the dialogue between computer and instruments, such as GPIB number, Instrument type, etc.*

Publications

[1] Nikolaides, M.G., S. Rauschenbach and A.R. Bausch, *Characterization of a SOI Based Thin Film Resistor in Electrolyte Solutions for Sensor Applications*, Journal of Applied Physics **81** (1998), no. 22, 5015–5018.

[2] Nikolaides, M.G., S. Rauschenbach, S. Luber, K. Buchholz, M. Tornow, G. Abstreiter and A.R. Bausch, *Silicon-on-Insulator Thin Film Resistor for Chemical and Biological Sensor Applications*, ChemPhysChem **4** (2003), 1104–1106.

[3] Nikolaides, M.G., A.R. Bausch, M.F. Hsu, A.D. Dinsmore, M.P. Brenner, C. Gay and D.A. Weitz, *Electric-field-induced capillary attraction between like-charged particles at liquid interfaces*, Nature **420** (2002), 299–302.

[4] Dinsmore, A.D., M.F. Hsu, M.G. Nikolaides, Manuel Marquez, A.R. Bausch and D.A. Weitz, *Colloidosomes: Selectively Permeable Capsules Composed of Colloidal Particles*, Science **298** (2002), 1006–1009.

[5] Bausch, A.R., M.J. Bowick, A. Cacciuto, A. Dinsmore, M.F. Hsu, D.R. Nelson, M.G. Nikolaides, A. Travesset and D.A. Weitz, *Colloidosomes: Selectively Permeable Grain Boundary Scars and Spherical Crystallography*, Science **299** (2003), 1717–1719.

Vielen Dank...

... an alle, die zum Gelingen dieser Arbeit beigetragen haben. Ganz besonders möchte ich mich bedanken bei

Prof. Andreas Bausch, der mir alle Freiheiten gegeben hat meine Interessen zu verfolgen und stets für Diskussionen und Gespräche zu begeistern war. Vielen Dank auch für all die Unterstützung über die pure Wissenschaft hinaus.

Prof. Erich Sackmann, der zu jeder Zeit ein offenes Ohr für alle Probleme und Sorgen hatte. Sein Ausscheiden aus dem aktiven Teil des E22 wird sicherlich nur sehr schwer kompensiert werden können.

Prof. Gerhard Abstreiter, der immer Zeit für meine Fragen und Probleme hatte, und für mich eine Art Mentor war, schon seit den Anfängen meines Studiums. Natürlich auch für die Erlaubnis alle Labors an seinem Lehrstuhl zu benutzen. Ohne diese Bewegungsfreiheit hätte die Arbeit so sicherlich nicht durchgeführt werden können.

Motomu Tanaka, der mich mit den NTA Lipiden vertraut gemacht hat und immer Zeit für meine Fragen hatte, sowie für wertvolle wissenschaftliche Tips und Tricks.

Markus Fischer, für die Preparation der Peptide und der Proteine.

Hubert Riedl und **Karl Brunner**, für das Überwachsen der Sensoren.

Florian Rehfeldt und **Oliver Purrucker**, mit denen ich seit dem Grundstudium gemeinsam durch alle Prüfungen und Unwägbarkeiten des Studiums gegangen bin. Dank natürlich für wissenschaftliche Hilfe, aber ganz besonders dafür, dass wir während der ganzen Zeit Spass hatten und Freunde geblieben sind. Vielen Dank auch für die tolle Lerngruppe während der Diplomvorbereitung und fürs Korrekturlesen der Arbeit.

Stephan Rauschenbach, der als Diplomand unersetzliche Beiträge in der Sensorentwicklung geleistet hat und mir ein guter Freund und Ratgeber geworden ist. Ihm